Three-dimensional Aligned Fibrillar Scaffolds—

Fabrication and Characterization

Shaoyang Anthony Yeh

Wolfson College

University of Oxford

A thesis submitted for the degree of

Doctor of Philosophy in Engineering Science

Trinity 2015

Abstract

Aligned fibrillar scaffolds (AFSs) have been widely studied for their application in regenerative medicine, providing possible transplantable tissue replacements for nerve, spinal cord, tendon, ligament, muscle, etc. However, researches in AFSs are technically challenging mainly due to the complex fabrication and characterization processes, especially when the AFSs are made to be fully three-dimensional (3D). As the structure is linked to the quality and function of the engineered tissue product, there is an urgent need for novel techniques to characterize AFSs non-invasively and non-destructively and to link their characteristics to their functions and outcome.

In this thesis AFS fabrication and characterization were explored. By combining second harmonic generation (SHG) imaging, multiphoton microscopy (MPM), and various image processing tools, the whole process of 3D tissue characterization could be achieved in a non-invasive, precise, and quantitative way. A proof-of-concept AFS with blended fibers made of polycaprolactone and porcine gelatin was used to demonstrate the feasibility of implementing such a strategy. The data indicated that, in terms of scaffold characterization, the proposed MPM method was capable of measuring the porosity of homogenous scaffolds precisely from deconvolved 3D images. Furthermore, the method could also be used to illustrate the orientation of the aligned nanofibers. Next, when SH-SY5Y neurons were cultured on the AFS, the MPM imaging was capable of evaluating the cell viability ratio, cell-localization in AFS, and neurite outgrowth. This provided guidance for selecting the alignment method for AFS functional recovery. Lastly, when employing this non-invasive imaging-based

characterization method, it was possible to illustrate the relationship between the alignment of collagen arrays in decellularized corneal stroma and the transparency. In summary, the proposed strategy can provide some essential scaffold/tissue properties (such as alignment of fiber, porosity of scaffold, and cell viability ratio) quantitatively and non-invasively, which will help both scaffold processing design and characterization.

Acknowledgments

First of all, I would like to thank my dearest supervisors, for I would not have had the opportunity to become part of this Oxford family if it were not for them. Professor Zhanfeng Cui has taught me how to think daringly yet practically, whereas Dr Hua Ye has taught me how to be mindful in experiments and discussions. I also have to show appreciation to the teachers who have guided me down this route. Professor Shu Chien of the University of California, San Diego, has taught me to focus on the fundamentals all the time. Professor Cynthia Reinhart-King of Cornell University introduced me to the goodness of multiphoton microscopy, thus shaping my thesis even before I came here. Professor Ian Lian, Dr David Lipson, Dr Bryan Moyer, and Dr Peter Hevezi were my heroes when things got rocky along the way.

Then, I want to give my appreciation to my lab friends. Dr Julian George has been a wise companion both in friendship and in technical assistance. Dr Pierre-Alexis Mouthuy has been my role model, who first taught me electrospinning and provided me with countless inspirations. Though there are too many people to thank, amongst my lab mates I especially want to tip my hat to Mr Andy Xue, Mr Cheng Ge, Ms Pirada Trongwongsa, and Dr Xiao Wan for they gave me cheers from the beginning to the end of my doctorate years. I would also like to thank Dr Jinnan Zhang and Dr Shi Chen, who were essentially my closest companions during late evening hours.

Next, I want to thank the people who assisted me in my experiments, especially Dr Mark Thompson, Dr Nasim Zargar Baboldashti, Dr Steven Mo, Dr Susan Graham, Dr Krishna Gupta, and Dr Kalin Dragnevski. My appreciation also goes to Ms Jie Ma,

Ms Emily-Jane Randall, and Ms Lin-Huey Supisara Chen for their generous contributions to the sample preparation works. And certainly, I would also like to thank the Biotechnology and Biological Sciences Research Council (BBSRC) and China Bio-Med Regeneration Technology Limited (CBMRT™) for providing various resources for my research.

Lastly, I would like to thank my family. My father and mother have always been supportive for whatever I want to do; and as in a Chinese proverb, it is virtually impossible to return their kindness. My brother Mr Shaoliang Yeh has always provided genuine opinions about how to move my life forward. Finally, I would like to show my appreciation to my fiancée Ms Wenlin He, who shows great patience and confidence in my endeavour. Meeting Ms He in such a romantic wonderland after travelling three continents must have been a miracle by God.

As it was well written:

"In that book which is my memory,

On the first page of the chapter that is the day when I first met you,

Appear the words, 'Here begins a new life'."

— Dante Alighieri, Vita Nuova *(1293)*

List of publications

Publications

1. Comparison between Two Types of Aligned Nanofibers for Guided Neurite Outgrowth (manuscript in preparation)
2. Non-invasive and quantitative analysis of corneal microstructure and transparency (manuscript in preparation)

Conferences

1. 9th European Solid Mechanics Conference (ESMC)

   Madrid, Spain; 6-10 July 2015

   - Oral presentation on *Comparison between Two Types of Aligned Nanofibers for Guided Neurite Outgrowth*

2. 19th Chinese Life Scientists Society in UK (CLSS-UK) Annual Meeting

   Oxford, U.K.; 21 September 2013

   - Awarded for The Best Poster

3. IChemE Biochemical Engineering Young Researchers Meeting 2013

   Birmingham, U.K.; 17-18 September 2013

   - Oral presentation on *Alignment of SH-SY5Y Neurons on PCL/Gelatin Electrospun Fibers*

4. Taiwanese Technology Symposium 2013

   Oxford, U.K.; 15 June 2013

   - Main organizer, coordinator, and event host

Abbreviations

2D	two-dimensional
3D	three-dimensional
ACL	anterior cruciate ligament
AFM	atomic force microscope
AFS	aligned fibrillar scaffolds
Ag	silver
ANOVA	analysis of variance
ATR	attenuated total reflectance
BDNF	brain-derived neurotrophic factor
BSA	bovine serum albumin
BSA-FITC	bovine-serum albumin-fluorescein isothiocyanate conjugate
CBMRT	China Bio-Med Regeneration Technology Limited
CFP	capillary flow porometry
CLSM	confocal laser scanning microscope
CNS	central nervous system
CT	computed tomographical

DAergic	dopaminergic
DI H2O	deionized water
DOF	depth of field
E	Young's modulus
EB	embryoid body
ECM	extracellular matrix
ELISA	enzyme linked immune sorbent assay
ESEM	environmental scanning electronic microscope
FDA	Food and Drug Administration
FPA	focal plane array
FTIR	Fourier transform infrared spectroscopy
FWHM	full width at half-maximum
Ge	germanium
GFP	green fluorescent protein
HFIP	1,1,1,3,3,3-Hexafluoropropan-2-ol
HTS	high throughput screening
IHC	immunohistochemistry
iPSC	induced pluripotent stem cell

LARS	ligament advanced reinforcement system
LEP	liquid extrusion porosimetry
lps	lines-per-second
micro-CT	micro optical tomography
MPM	multiphoton microscopy
MSC	mesenchymal stem cell
NA	numerical aperture
NADH	nicotinamide adenine dinucleotide phosphate
NGC	nerve guidance conduit
NGF	nerve growth factor
NIR	near infrared
NLO	nonlinear optical
NPC	neural stem/progenitor cell
OVA	ovalbumin
PCL	polycaprolactone
PDMS	polydimethylsiloxane
PEG	polyethylene glycol
PEO	poly(ethylene oxide)

PGA	poly(glycolic acid)
PLA	poly(lactic acid)
PLGA	poly(D,L-lactic-co-glycolide)
PLLA	poly-L-lactic acid
PS	parallel metal strips
PSF	point spread function
RA	retinoic acid
RD	rotating drum
REST	RE-1 silencing transcription factor
RGD	arginylglycylaspartic acid
RM	random collection
rms	root mean squared
ROI	region of interest
ROS	reactive oxygen species
SD	standard deviation
SE	standard error of the mean
SEM	scanning electron microscope
SHG	second harmonic generation

SIMS	secondary ion mass spectrometry
SNR	signal-to-noise ratio
STORM	stochastic optical reconstruction microscopy
TEM	transmission electron microscope
TPEF	two-photon excited fluorescence
Tuj1	neuron-specific class III beta-tubulin

Contents

List of figures

List of tables

Chapter 1 **Introduction**

1.1 Background

The regeneration of lost human body parts is an extremely challenging task, requiring the use of the most advanced materials, methods, and assessing technologies. A huge number of tissues or organs, such as tendons, ligaments, muscles, nerves, or corneas, possess the needed physiological functions for a normal daily life. A common feature that is present in all of them is the highly aligned cell population along with oriented polypeptide fibers, which directly contribute to the organ's strength, signalling, directionality, and physiological functions. It is therefore a common approach for tissue engineers to design according to these aligned patterns, as in the development of the aligned fibrillar scaffolds (AFSs). The biggest challenge becomes how to achieve the most control over fiber alignment in an AFS in order to facilitate its maturation into targeted tissues.

A successful tissue engineered product requires controls at several steps in the making. The ultimate goal is to create a functional artificial human tissue, in which the scaffold biomaterial gradually degrades away and becomes populated by cells showing similar viability, population density, and differentiation to those of the targeted tissue. The product should be sterile prior to transplantation and biocompatible enough not to induce immune responses that cause post-transplantation ailments. The process to create a mature tissue typically involves the following stages: (1) scaffold design, (2) scaffold characterization, (3) cell-seeding, (4) tissue characterization, and (5) tissue transplantation. Each of these stages is technically challenging and requires a significant

amount of time and funding to complete in a satisfactory manner. Typically, a research project in AFS would require the involvement of several groups of expertise. This further introduces complexity and reduces the successful rate for completing a product. In order to solve these issues, whether they are technical or managerial, it is necessary to simplify the whole process for creating such a tissue engineered product while maintaining the high confidence for its transplantation readiness. Amongst these steps, scaffold fabrication, scaffold characterization, and tissue characterization are the three that are more diversified in technical requirements. Highly controlled processes in these three stages are essential for delivering a transplantable tissue product that promises functional recovery.

AFS operates on the hypothesis that properly aligned micro or nanofibers would provide the physical and mechanical cues for properly aligned cells, leading toward the recovery of targeted physiological function. Properties of these aligned fibers, including degradation of the material, degree of alignment, diameter and density of fibers, and hydrophobicity, would provide necessities for functional recovery. If the fibers are not properly aligned, the AFS would not present proper mechanical strength not only for proper cell induction, but also for the tissue as a whole to withstand necessary stresses or to exercise functions. These issues would easily cause the tissue product to be unreliable for transplantation.

While there are other methods that may create fibrillar scaffolds (e.g. freeze-drying), electrospinning has dominated this field due to its economical, robust, and adaptive nature. More importantly, electrospinning provides a moderate control over the fiber alignment for the creation of AFSs. It is capable of creating micro-to-nano scale fibers and is also adaptive to various materials of choice and morphological adjustments.

In the last decade it has already been used widely in tissue engineering, as implied in the annual increment of related reports. For the creation of certain complicated AFSs for tendons and ligaments, which are dense regular connective tissue that consist of collagen types I and III primarily (Vunjak-Novakovic *et al.*, 2004, Fan *et al.*, 2008, Teh *et al.*, 2013), some fiber-alignment methods have been proven useful in the creation of these fibrillar scaffolds. The resultant scaffold is relatively rigid for surgical handling, and can be folded or rolled to match the need of the larger organ. Some of the AFSs have already been involved in transplantation to provide a treatment, such as the replacement with artificial bladder.

Fabrication of an AFS, however, would require more than electrospinning alone. First of all, it is necessary to identify a robust and reproducible method that will yield highly aligned nanofibers. Due to the simplicity of the electrospinning apparatus, variations exist when comparing the results from one machine to another. For this reason, the collection method has to be as simple as possible, yet highly effective in creating parallel fibers. This topic remains a highly challenging issue in the electrospinning field. Secondly, the fiber diameter has to be controlled in a certain range, usually smaller than a cell body in order to promote 3D cell growth along the fibers. If the fiber diameter is too large, it may be interpreted by the cells to be a flat 2D surface; the AFS then loses its purpose to serve as a 3D culture environment. For the cultured cells to grow and mature uniformly, it is also expected that the scaffold surface in contact would also be uniform. This means that the fibers diameter should present a distribution that shows a small variance. Thirdly, cell growth on the scaffold remains a challenging issue. Although there are many materials that can be used in electrospinning, some of the materials would not only be bio-incompatible, but would also be toxic for

the cells. Some, on the other hand, do not facilitate cell adhesion and may degrade rapidly in the incubated environment, apparently not stable enough for cell growth. Additionally, it is difficult for some materials (e.g. collagen) to form a homogenous polymer solution, which is required for high-quality fibers. These factors narrow down the material of choice to a certain group of biomaterials, which would be further limited if agent delivery is considered as a potential scaffold function to be included. As a result of this, for a systematic review of the design of AFS that leads to tissue maturation and functional recovery, the material of choice would be the first crucial question to be investigated.

While the fabrication of AFS already requires lots of planning, what would actually constrain the completion of the project would be the limitations from the characterization process. The main reason is that for the AFS to be a good product for functional recovery, it has to be evaluated for factors related to the clinical workflow yet remain completely sterile. At present several machines (and thus experts of different fields) are required for a complete characterization of a fully mature tissue because each machine may only give a piece of puzzle for the big picture. This makes the characterization of 3D-, nano-scale AFSs a necessary yet extremely difficult process. Firstly, visualization of the details of nanofibers would require a very specialized microscope, such as the scanning electron microscope (SEM), but such an imaging method would be considered 2D, and cannot explore the volumetric information of the scaffold. Furthermore, the resolution of the fiber texture at nano-scale is usually not ideal. Although coating treatment (with certain metals such as gold) can increase the contrast, it alters the surface and loses some texture information about beads or cracking on the fiber. Then, there is the question of how to characterize the porosity of the

scaffold. At present there is no standard method for the testing of porosity. It is related to many factors, but in general it is due to the fact that slight variations in the formation and the fiber size of the scaffold can render a previously successful method useless. There is also the issue of how to define porosity—whether from a void-space or mass-transport point of view. With respect to different definitions, the tested results can be dramatically different and hard to compare. Next, even if the above two issues are resolved and complete scaffold characterization can be obtained, there is also the issue of the tissue characterization after cell seeding. In recent years, stem cells have played an essential role in novel tissue engineering designs because they are pluripotent and may eliminate lots of unnecessary immune responses beforehand. However, Stem cell culture is challenging in that the cells can be fragile (especially upon removal from the culture plate) and may require several chemical or physical treatments to induce enough proliferation and complete differentiation. Typical characterization of cell growth requires the multi-channel fluorescent microscope that can display various information (e.g. cell morphology, cell number, and immunohistochemistry marking for cell identity or intracellular features), but a normal fluorescent microscope would have difficulties in obtaining 3D scaffold information. Therefore, for researchers it is necessary to prepare different batches of scaffolds for different characterization methods, which may lead to unwanted variation aside from the extra expenditure. Lastly, the most existing characterization methods would eventually contaminate or destroy the samples in the process. For this reason, albeit they might help the researcher obtain needed information, the whole process from fabrication to characterization would require different scaffold/tissue samples at different stages, which continuously introduce variances and errors in the analyzed results. This is highly inconvenient for both quality control and

the research cycle that are needed for pushing a tissue engineered product to the market, and certainly contradicts what is necessary for a sterile transplantation process. In an ideal scenario, a non-destructive and sterile characterization method would be useful by providing *in situ* analysis of exactly the same samples that would undergo tissue culture and transplantation. With such a method, it is possible to accelerate the whole research/development/quality processes by months or even by years.

If the properly aligned nanofibers in AFS can lead to properly aligned cells and the resultant tissue function, it is then essential to investigate into what design constitutes a good AFS product and how to make it readily sterile for direct transplantation. This thesis was therefore designed to investigate some available materials, fabrication methods, alignment methods, and characterization methods in an attempt to identify key design criteria involved in facilitating the use of AFS functional recovery.

1.2 Aims and objectives

The specific objectives that lead toward recovery of tissue functions using AFS designs are:

1. *Investigation into a chemical-eluting electrospun AFS for its controlled release profile and related characterization methods for nanofibers*
2. *Construction and optimization of a proof-of-concept AFS that is designed to encourage aligned cell growth and to simultaneously facilitate non-destructive tissue characterization*

3. *Tissue culture analysis of the designed AFS using a characterization strategy that is based on second harmonic generation (SHG), two-photon excited fluorescence(TPEF), and image analysis*
4. *Non-invasive structural characterization for an end-point, fully 3D AFS product for the analysis of functional recovery*

1.2.1 Investigation into a chemical-eluting electrospun AFS

Because many of the electrospun AFSs would be empowered with agent-release capability for easier tissue culture, it is desirable to select a material that may be useful for both cell adhesion and agent release. Polycaprolactone (PCL), backed with a long history of FDA approval for the medical devices that were made from it, seemed to be a reasonable candidate for agent-release designs (Woodruff & Hutmacher, 2010). Another commonly used polymer call polyethylene oxide (PEO), which is frequently used in agent formulation, may provide some insight into the fine-tuning of agent release profile (Song *et al.*, 2011). Agent release investigation should not be limited to the material of choice, but also extend to prominent fabrication methods. Aside from the simple blending method, it would also be interesting to look into another prominent fabrication technique called co-axial electrospinning, which compartmentalizes the agent-loading in the nanofiber.

Another focus in this early work is to explore the drawbacks of existing AFS characterization methods. While scanning and transmission electron microscopies still play a crucial role in nano-fibrillar scaffold characterization, their processes may destroy the samples during characterization, which forbids continuation toward cell

seeding and thus increases the chance of batch variation. There might be other technical challenges involved which would limit the accuracy of the obtained data for analysis.

1.2.2 Construction of a proof-of-concept AFS

A proof-of-concept AFS is designed for the investigation of how fiber alignment may lead to desirable guided cell growth and functional recovery. Such an AFS would not only produce reliable non-destructive SHG signals for scaffold/tissue characterization, but also consist of well-aligned fibers that may possibly provide guided cell growth to many cell types. Gelatin and collagen are two SHG-capable materials that are commonly used in scaffold fabrication. Porcine gelatin can be blended into electrospun fiber for tissue engineering (Ghasemi-Mobarakeh *et al.*, 2008), so it seems to be a reasonable testing material for the proof-of-concept AFS. It is essential to understand the reliability of the SHG signals for quantification of scaffold properties, and one way to investigate this issue is through the quantification of void space/porosity of a 3D scaffold. MPM estimate of the void volume from SHG signals from the two materials will be tested against the result from liquid extrusion porosimeter (LEP) to see if it is possible to achieve a high data agreement.

The proof-of-concept AFS should also display highly aligned nanofibers. However, at present there are too many alignment methods to choose from. In order to identify the most effective method for creating highly aligned fibers, two fundamental methods—parallel metal strips (PS) and rotating drum (RD)—will be selected as representatives for the investigation. AFS created from these two methods will be characterized for their fiber diameter, alignment angle and stiffness in order to provide a

later reference. Such analysis may serve as an indicator for future selection of alignment methods for specific tissues.

1.2.3 Tissue culture application of the designed characterization strategy

After the aligned fibers are created and characterized, they will be tested for their capability to induce cell growth. SH-SY5Y neurons will be used to provide a model for the engineering of the nerve guidance conduit (NGC). Neurite outgrowth on the PS and RD fibers will be compared with that on the randomly collected fibers (RM). Earlier characterization of the properties of these fibers should provide insights into the interpretation of the neurite outgrowth results.

Simultaneously, experiments in this chapter will also be used to see how MPM imaging may be able to contribute to cell/tissue characterization. The characterization will take advantages of the SHG signals from the fibers and the stained TPEF signals. Cell viability and location information will be collected using 3D MPM imaging and analysed with spot objects. The result will be coupled with alamarBlue test for confirmation of successful cell culture. Neurons will be stained for their neuron-specific class III beta-tubulin (Tuj1) in the later immunohistochemistry for easier measure of 3D neurite length and observation of the cell-substrate interactions. It is expected that the proposed characterization strategy would be able to statistically distinguish slight differences in neurite outgrowth.

1.2.4 Non-invasive characterization for an end-point, fully 3D AFS

The void space analytic method will be applied once again for the analysis of the relationship between scaffold structure and function. A group of 80 vacuum-sealed

porcine corneal scaffolds will be first tested for their level of transparency (in terms of Total Transmittance and Haze). The tested results will be normalized for the selection of samples showing extreme values. These samples will then be visualized non-invasively using MPM for the success of cell removal. The collected SHG images will also be transformed into quantitative data and analysed using several image analysis tools. Isosurface analysis, for example, will be used to illustrate the interior fibrillary density of these samples. Another software called SurfCharJ will be used to test the texture of the exterior of the scaffold. Analyzed results from these samples will be compared with their transparency readouts in order to draw possible relationships between corneal microstructure and transparency functions. This investigation will illustrate the non-invasive nature of MPM characterization and present an innovated method for functional analysis of an AFS such as corneal scaffolds.

1.3 Scope of study

The proposed project in this thesis is broad and boundless due to the fact that there are countless ways to fabricate or characterize a 3D AFS. In order to show that properly designed 3D AFSs can guide cell growth, promote functional recovery and be ready for transplantation, it is necessary to rely on quantifiable entities to make the judgment at each point. Hence, this thesis focused on proving that proper selection of alignment method that can lead to dramatically better cell growth, which likely contributes to higher functional recovery. In that regard, the scope of AFS fabrication was intentionally set around key issues such as agent delivery stability, fiber diameter, alignment angle variability, scaffold porosity, mechanical strength, induced

morphological change of the cells, and non-invasive functional analysis. Though there are more parameters for a matured tissue scaffold design, they are omitted so that this thesis may focus on characterizing the success in cell growth and functional recovery. For the same reason, the characterization effort was intentionally set around certain aspects that meet the minimum requirements of scaffold/tissue characterization, while maximizing the quantitative precision and potential in research applications. In order to achieve this, the study first focused on common features that are needed for a 3D AFS. It is assumed that the characterized AFS would be 3D, properly aligned, biocompatible, cell-adhesive, and agent-eluting. The report would then explore individual properties and their corresponding characterization methods, attempting to find a way to simplify or replace current methods without sacrificing precision or introducing artefacts. The proof-of-concept AFS would be created to demonstrate how the two principle alignment methods may create two significantly different scaffolds and second harmonic generation (SHG) imaging may contribute to the overall characterization strategy. Considering the lack of point spread function (PSF) assessment method and the eventual goal of this report, the study only focused on the quantification of blindly deconvolved backward SHG signals rather than the original signals. For image processing and analysis, no new algorithm was created during the investigation; rather, this thesis focused on utilizing existing software to provide an evaluation of the precise control in image acquisition and quantification that can lead to functional analysis of the resultant tissue.

This thesis is organized into seven chapters. Following this chapter, Chapter 2 dealt with literature review, specifically on the fundamentals of electrospinning and the concept of SHG imaging using multiphoton microscopy (MPM). This lays out the

current challenges in the fabrication and characterization of an AFS and suggests an approach that can realize the eventual functional transplantation. Chapter 3 explores the most applicable material of choice on the assumption that such an AFS would employ a controlled-release mechanism in the future. On the basis of that, Chapter 4 explores the possible way to introduce SHG signals to the AFS, which likely can enrich the information generated by the characterized AFS. It then compares two promising porosity-characterization tools and two fundamental alignment methods in order to present a proof-of-concept AFS design. Chapter 5 was built on the understanding from previous chapters and presents a tissue-culture result, comparing the guided neurite outgrowth on the scaffolds made from the two alignment methods. . At this point all the key factors that lead to satisfactory characterization of the representative AFS should have been identified and assessed. Chapter 6 then switches direction to the characterization of a completely packed, fully 3D decellularized corneal AFS. Works in this chapter explore and show that highly-aligned scaffold microstructure can lead to the recovery of transparency in cornea. They also explore the possibility of conducting a highly precise, quantitative, and non-invasive characterization process so that the scaffold can be readily transplantable. In Chapter 7 the project is summarized and discussed for its practicability, scientific contributions, applications, and future improvements.

Chapter 2 **Literature review**

The goal of this thesis is to enhance understanding of current fabrication and characterization methods of AFSs for tissue replacement. Such an investigation is not only essential for selecting the best approach for functional recovery of the targeted tissue or organ, but also for making the tissue product readily available for surgical intervention. *It is hypothesized in this thesis that the aligned fibers in AFSs can guide and result in aligned cells during tissue culture, which enhances the eventual function of the targeted tissue.* It is worthwhile to start the investigation by considering how the field of tissue engineering emerged and became distinguishable from other disciplines in medicine. Afterwards, it is necessary to identify key measurements in the clinical workflow/transplantation and the ones that are necessary for the laboratory development of a novel AFS. Following such discussion should be a survey of available methods that may be used to create such a clinically applicable AFS product that may promise functional recovery.

2.1 The road to create engineered tissues

There are limited ways to replace a missing body part for a patient. Traditionally, a prosthetic device that is made from wood, metal, or plastics is used to substitute the lost tissue or organ. Such an approach cannot be fully integrated into the body; more importantly, it does not regenerate many necessary physiological functions of the tissue. In some cases, embedded prosthetic devices such as the artificial knee joint might also

require a second surgery years later to prolong its use. Another novel approach that has been made available is to rely on cloning technology to provide the needed body part. Cloning utilizes the genomic sequence of the patient to create an embryo that, as it develops, should be a replica of the patient. Although such a method is the most direct way to provide functional tissue, it has serious ethical concerns such as the sacrifice of one life for another, and is therefore usually avoided. A more applicable and acceptable approach that has gradually matured in recent years is *tissue engineering*, which relies on the use of biodegradable materials, scaffold design, and stem cells to artificially create functional body parts.

The origin of "tissue engineering" as it is recognized at present can be traced back to Professor Y.C. Fung's proposal to NSF (United States) for an engineering research center to be entitled "Center for the Engineering of Living Tissues" in 1985 (Fung, 2001). The term was drawn upon the traditional definition that "tissue" would be presented as a fundamental level of analysis of living organisms between cells and organs. Gradually, this new field emerged to embody cell biology, biochemistry, material science, fabrication techniques, and characterization methods. Tissue engineering, therefore, could clearly be seen as a combination effort from many other existing fields to suggest a possible solution to unsolved medical issues. But it was only later, when other fields such human genomics, stem-cell biology, and nanotechnology became more mature and systematic, that tissue engineering no longer stayed in concept, but became quite hopeful as a treatment. Newer design concepts also appeared, such as the idea of cell therapy and the use of extracellular matrix (ECM) materials as the supporting scaffold for tissue maturation. This was also the point where designs for an integrable body part for functional recovery became the eventual goal, which is

dramatically different from conventional prosthesis approaches. Some tissue-engineered products, such as artificial bladder, corneal epithelium, and engineered skin, have entered the clinics (Gelain, 2008). However, tissues/organs that are complex in microstructure, materials, and identities of cultured cells require more advanced scaffold fabrication methods.

2.2 Impacts of research in aligned fibrillar scaffolds (AFS)

The use of three-dimensional (3D) aligned fibrillar scaffold (AFS) is one of the approaches that have driven tissue engineering forward. Many human tissues, including muscles, tendons, ligaments, nerves, and corneas, show an ECM environment that consists of aligned nano- or micro-protein fibers. Alignment of these fibers plays an important role in guided or polarized cell growth, providing needed mechanical strength and maintaining the physiological function of the tissue. For example, Meyle *et al.* (1993) used transmission electron microscopy (TEM) to show that seeding dermal fibroblasts on silicone wafer that possessed 1~2 μm microgrooves for 48 hours would induce alignment of cell body and actin filaments during initial cell adhesion. Since AFS would possess fibers of similar size, it can be expected that such cell-substrate interaction would be dynamic. Tissue regeneration of these elongated tissues typically requires artificial creation of such an aligned fibrillar environment for cells to be cultured. Ligament regeneration, for example, can help solve some of the most common injuries to sportsmanship, such as anterior cruciate ligament (ACL) injury. Gianotti *et al.* (2009) did a national survey for New Zealand, which revealed that the incidence rate per 100,000 person-years was 36.9 for ACL surgeries, and the mean treatment cost for

these surgeries is $11,157 (New Zealand Dollars). Ratcliffe *et al.* (2015) also reported that there are as many as 100,000 ACL repairs performed annually in the United States. There lacks enough donors for healthy ligaments. The ailments at the donor sites followed by the autograft treatment have further restricted doctors to provide treatments. Xenograft from animal sources could cause immune reactions and has therefore been avoided if alternative treatment exists. Considering the fact that ligaments are composed of closely packed collagen fiber bundles that are parallel to provide stability of joints in the musculoskeletal system (Woo *et al.*, 2006), regeneration of these tissues can benefit from well-designed 3D AFSs. However, at present the popular ligament advanced reinforcement system (LARS) suffers from synovial hyperplasia in the knee joint, which contains a large amount of hemosiderin deposition (Li *et al.*, 2012b). Presence of thick fibrous scar tissue around the graft may also cause early failure of the scaffold. As a result, complete development of a prototypic AFS requires inclusive analyses of

1. Control of fibrillar alignment
2. Material toxicity
3. Material degradation
4. Mass transport
5. Mechanical loading
6. Thermo response
7. Acidity response
8. Inflammatory/immune response
9. Functional assessment of the cultured tissue

Amongst all these assessments, points 2, 3, 5, 6, 7, and 8 are directly related to the material of choice. 1 and 4 are related to the fabrication method, and 9 is directly

related to the cultured cells upon differentiation. This also places the emphasis in the sequence: biomaterial of choice, fabrication technique, and non-destructive functional assessment. Using a material that has an established record in scaffold design could help speedup the development process. Proper fabrication technique and non-destructive functional assessment, however, need to be investigated further. How much fiber alignment can scientists obtain and whether an AFS made from such a method is truly useful for induced morphological change in cells remains to be investigated. And since contamination of the AFS during characterization can directly prevent successful transplantation, it is crucial to find a proper characterization method that can lead to functional assessment of the cultured AFS tissue. This is the key to make the AFS readily available for clinical measurements before surgery, and important parameters should be identified and readily tested.

2.3 Characterizations and regulations

Along the way of tissue engineering emerging, one thing that stands out as the core pillar for this field is the method for characterization. ECM-based tissue engineering involves various important steps (Morgan *et al.*, 2013b). These include:

1. Selection of the most appropriate cell type
2. Design of scaffold
3. Seeding the cells onto the scaffold for a sustainable cell culture
4. Incubation with bioreactor to encourage physiologically relevant responses
5. Implantation to promote maturation of the tissue, targeting functional recovery of the organ

For the product to be successfully developed for the market, each of the steps has to be characterized for milestone accomplishments. Selection of the cell type depends on the tissue type the researcher would like to regenerate, so is not part of the fabrication or characterization process to be discussed here (although the cell culture protocol directly affects the tissue characterization process later). Scaffolds that are designed for cell culture conventionally rely on scanning electron microscopy (SEM) and transmission electron microscopy (TEM) to provide high resolution images of the nano- or micro-patterns (Meyle *et al.*, 1993, Nanci *et al.*, 1996). It is common to use SEM to analyse negative copies of the original nano- or micro-pattern surface that may be used to induce cell-substrate interactions. TEM has been involved in the analysis of the structure of nanoparticles. Although SEM and TEM seem to provide necessary characterization of certain properties, their samples are subject to radiation damage (Egerton *et al.*, 2004). SEM samples experience electrostatic charging on the visualized region of the specimen. The region in view later becomes so charged that it repels the incident beam, leading to unstable or distorted images. A direct consequence from this is that the window for viewing the targeted region is generally very short. TEM, on the other hand, can easily elevate the local temperature during imaging, therefore causing burning of the fibrillar scaffold. Charging of a TEM specimen can also produce a mechanical force that may tear the thin polymer. Furthermore, TEM most likely requires ultrathin sections of samples in order to achieve full penetration. Considering the diameter range of typical fibers for tissue engineering, the success rate for a characterization that is done by TEM may vary case by case. Therefore, it would be highly desirable to have a characterization method that does not induce similar damages to the nanofibers, yet is able to illustrate important fiber properties such as diameter and

orientation. Reliable scaffold characterization methods are necessary for the laboratory development of the AFS products. On the other hand, tissue characterization, which provides the measurements for the clinical workflow, would mostly require optical or fluorescent microscopy in order to non-invasively assess cellular properties such as the viability ratio, the stage of cell differentiation and the degree of functional recovery. These measurements determine whether an AFS product can successfully integrate into the system of the patient and provide the wanted physiological functions. Clinical measurements, however, are not totally excluded from the developmental phase. *In vitro* tests of the cellular responses to the designed AFS should be conducted using related cell lines to provide an estimate of the degree of tissue maturation before such a product enters the market. Both developmental and clinical characterization methods should be considered as a package for the regulation of such a novel AFS product.

For characterization that may meet regulatory needs, two essential questions arise: (1) what is the most appropriate and standardized machine or technique that can assess the success of each step, and (2) what grading/quantitative criteria do researchers use to define success in each step. The answers to these questions are essential for a tissue engineered product to pass governmental regulations. In the United States, a tissue product would be regulated by the Food and Drug Administration (FDA) under the category "combination products" (O'Shea & Daniels, 2012). A combination product has multiple characteristics. It can be a drug/device, a biologic/device, a drug/biologic, or a drug/device/biologic product. By definition, a product that combines two products of the same type (e.g. a device contains two or more drug ingredients in a single dosage unit) is not a combination product. A cell-culture scaffold for tissue engineering, however, would likely fall into the category of biologic/device or drug/device/biologic,

depending on whether a drug- or peptide-eluting design is involved. For this kind of product, the Safe Medical Devices Act of 1990 directed the FDA to assign the review process to an agency center based on the product's primary mode of action. Similarly in Europe, legal instruments such as European Regulations and Directives, and national laws of the Member States, establish a framework that manages all aspects of any medical products business (Wilson, 2011). These bodies would determine the single mode of action and would therefore provide the most important therapeutic effect of the combination product and serve as the key to whether or not such a product can be put on the market. Disregarding the drug release issues, from a biologic/device point of view, the cellular activities and potential recovery of physiological functions would hence be the most important criteria that define a successful tissue scaffold. A complete characterization process for the AFS scaffold, therefore, would need to include cell imaging or functional assessment of the eventual tissue.

2.4 Electrospinning as the primary mean for AFS design

Fabrication of an AFS is heavily dominated by one technology called electrospinning. Various techniques such as electrospinning, meltblowing, flash-spinning, forcespinning, drawing, template synthesis, and phase separation have been developed for the creation of polymeric nanofibers (Vasita & Katti, 2006, Nayak *et al.*, 2011). Meltblowing, though being simple to use, requires a specially designed small orifice in the die and high viscosity of the polymeric melt. Flash-spinning can only produce short fibers from 3 to 10 μm in length. Forcespinning requires good control over high temperature at specific times. Drawing lacks a consistent control over the

fiber diameter. Template synthesis and phase separation cannot be scaled up to match the size of human tissues. Amongst these methods, electrospinning stands out as an AFS fabrication method because it utilizes a simple process and creates long and continuous fibers from an enriched list of available materials. These advantages enable prototypic designs of fibrillar scaffolds, which make electrospinning a reliable approach toward the complicated tissue engineering process. The diameter of the fibers usually ranges from a few micrometers to tens of nanometers, which is similar to the peptide fibers typically found in ECM. One drawback on its use in tissue engineering, however, is that the presence of harmful organic chemical solvents prevents possible addition of cells during scaffold formation (Gelain, 2008). This would later prevent a uniform distribution of the cells throughout the scaffold, and would require complicated fabrication methods and precise control over pore diameters. Nevertheless, electrospinning still presents more opportunities for successful AFS designs.

The original idea of applying electric potential to alter liquid droplet formation can be traced back to more than a century ago (Bose, 1745, Rayleigh, 1882, Cooley, 1902, Morton, 1902). The first patent appeared in 1934, when an apparatus for producing polymer filaments using electrostatic repulsion against surface charges was formally disclosed (Formhals, 1934). However, due to a lack of supporting technologies, this method remained underdeveloped for a very long period. In the early 1990s, several research groups revisited this technique by demonstrating that this electrostatic method is highly versatile in fabrication—it can be used with a broad range of organic polymers to form nanofibers (Doshi & Reneker, 1995, Reneker & Chun, 1996). Other material combinations such as natural, blended, or woven polymers can also be made. It is also possible to impregnate nanoparticles or drugs amongst these polymers to create

functional fibers. Technically, almost any soluble polymer that presents a high molecular weight can be electrospun (Wang *et al.*, 2006). The term "electrospinning" was finally coined and widely accepted in the field of polymer technology. During the last decade, researchers have found a new use for this technology—to create nano-fibrillar scaffolds for tissue engineering and agent release. Thereafter, research groups world-wide have investigated modification of the electrospinning process, creating finer fibers, oriented fibers, more porous scaffolds, and agent-releasing conduits. The nanofibers can be so thin that it forces cells to adhere to the scaffold in a three-dimensional manner. More importantly, as stem cell biology progresses and more chemical agents (e.g. growth factors) are identified as inducers for cell differentiation, agent-release has become a core research focus in tissue engineering. It is essential to ensure that the patient's own stem cells can be cultured into the targeted cell type after differentiation *in situ*, so proper design of the controlled release mechanism and the guarantee that the agent can remain effective after the release are necessary. Electrospinning, due to the physical simplicity of the fiber formation process, has a high potential for successful agent loading, control, protection, and release. With respect to AFS design, several papers have been published on easy and reliable methods that created moderately aligned nanofibers. This makes electrospinning a highly potent method for tissue engineering. Since 2000, the number of tissue engineering papers related to electrospinning has increased dramatically (as shown in Figure 2.1). The worldwide research community is active and enlarging. Electrospinning, therefore, is the most useful method in realizing products of AFSs.

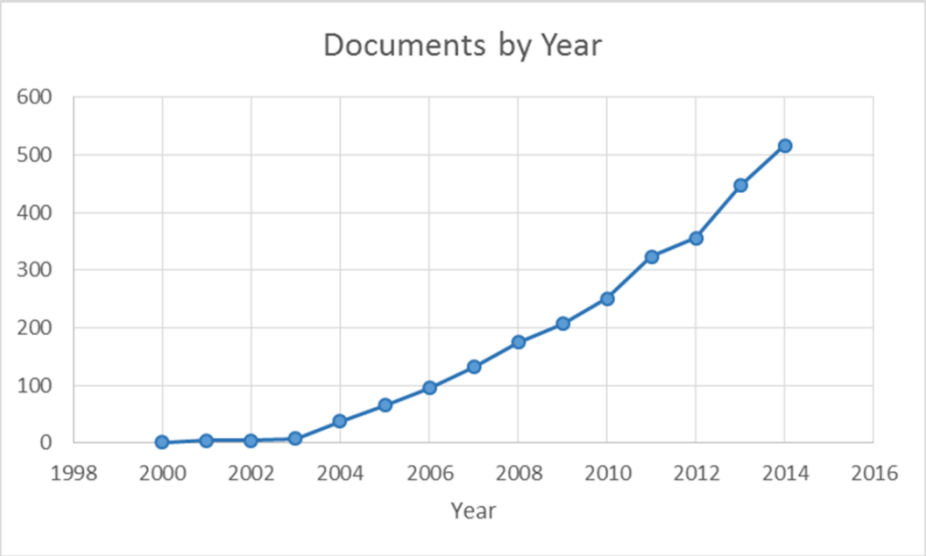

Figure 2.1: Annual number of tissue engineering reports that are related to electrospinning. Database: Scopus.com. Keywords: "tissue engineering"* AND electrospinning*. Data range from 2000 to 2014, accessed on 10th September 2015.

2.5 Fundamental theory of electrospinning

The schematics of a typical electrospinning apparatus is shown in Figure 2.2 (Bhardwaj & Kundu, 2010). In general, a high voltage system is used to create an electrically charged jet of polymer solution made with a highly volatile solvent. When the jet is dried, the charged extrusion is collected on the grounded collector and left as a polymer fiber (Doshi & Reneker, 1995). There are four major components that are needed to complete this process: a high voltage power supply, a syringe that delivers the polymer solution through a capillary spinneret, a collector that is normally earthed, and a syringe pump that continuously injects more polymer solution to the spinneret (Huang *et al.*, 2003). As the voltage increases and enters a certain range, the pendant polymer drop at the nozzle becomes so statistically charged that the induced charges are evenly

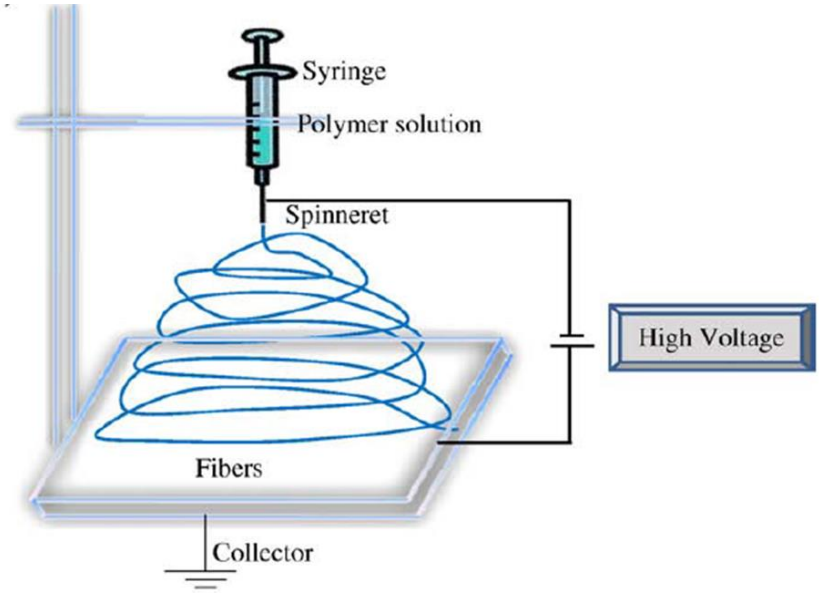

Figure 2.2: A typical setup for vertical electrospinning of random fibers. The nanofiber is ejected in a whipping motion as it travels to the grounded collector. *Source: (Bhardwaj & Kundu, 2010).*

distributed over the surface (Li & Xia, 2004). The droplet, originally found in a spherical shape at equilibrium, becomes distorted as the charges within the droplet migrate toward the surface above the grounded collector. Eventually, a protrusion starts to appear on the end of the droplet, turning the droplet into a conical shape known as the Taylor cone (Taylor, 1969, Reznik *et al.*, 2004). At a certain voltage, the repulsive electrostatic force overcomes the surface tension, and a charged jet is ejected from the tip of the Taylor cone toward the collector. This ejected jet would undergo a stretching and whipping motion, forming a series of continuous loops due to residual charges (Reneker *et al.*, 2000, Shin *et al.*, 2001). As the solvent along this elongated jet evaporates, solid polymer fibers are left over and lay themselves on the grounded collector. There have been lots of theoretical discussions and direct observations over the years that can explain this process in more details (Huang *et al.*, 2003, Greiner & Wendorff, 2007, Reneker *et al.*, 2007, Agarwal *et al.*, 2009). Fundamentally speaking, electrospinning is based on physics. When a low-viscosity polymeric fluid is heavily

charged, the forces generated by surface tension in a solvent overcome those needed for viscous flow (Wang & Ryan, 2011). The Taylor cone then ejects the jet into a regular stream of droplets through Rayleigh instability. When the viscosity of the fluid increases (due to evaporation of the solvent), the balance between surface tension and viscous flow favours the formation of a cylindrical jet. A stretched polymer solution will strain harden due to entanglements from the individual unit under the influence of the van der Waals forces, and solvent evaporation will also increase viscosity, eventually vitrified or crystallize the structure (of the fiber).

2.6 Processing parameters for electrospun scaffolds

During AFS development, there are several parameters that need to be controlled in order to stabilize the jet and create fibers of repeatable properties (Doshi & Reneker, 1995, Robb & Lennox, 2011). The parameters can be put into three categories: material, spinning, and ambient. Material parameters include the solute and solvent of choice, molecular weight of each polymer, concentration and viscosity of the polymer solution. Selected solvent is usually highly volatile, and would likely be miscible if the peptide-base content was mixed with the polymer solution. Spinning parameters include the critical voltage range (in kilovolts), flow rate of the polymer solution, the distance between the spinneret and the surface of the collector, and the duration of collection. Ambient parameters include the air control, humidity, and environmental temperature. These parameters have allowed electrospinning to become a versatile technique in tissue engineering. For example, the diameter of the fiber may be controlled with fine-tuning of the concentration of the polymer solution for the desired range. The duration of

collection can affect the thickness and local distribution of the fibers. If the spinning distance between the spinneret and the collector is large, it delays the time for solvent evaporation and encourages thinning of the fiber. These parameters are hardly independent of each other. As a result, it is quite challenging to create repeatable samples. Usually, it is necessary to undergo an optimization step to ensure that all the parameters can be controlled in order to create high quality fibers.

As a nanofabrication technique for AFSs, in the case wherethe scaffold does not involve drug release or associated bioreactor design, certain developmental characteristics require a higher control and a more elaborated characterization process:

Fiber diameter (2D vs 3D)

Fiber alignment

Fiber hydrophobicity (for successful cell adhesion)

Fiber texture (for successful cell adhesion and migration)

Fiber morphology (for guided cell growth)

Fiber mechanical properties (for guided cell growth)

Scaffold thickness (for transplantation considerations)

Proper selection of **fiber diameter** is important for successful tissue mimicking. It has been accepted amongst the scientific community that flat glasses or plastic substrate for *in vitro* experiments cannot represent the real tissue microenvironments (Gelain, 2008). Cells possess the ability to recognize topographical differences as presented in grooves and ridges, which tend to guide development of certain cellular

features such as the cytoskeleton. It was found that protrusions of cells were unable to bend over a surface inclination that is greater than 4°. Such contact would force the cells to orient in a direction parallel to the microgrooves. Hence, a fine control over fiber diameter, for example, is also essential for 3D culture. As Doshi and Reneker (1995) reported, electrospun fiber may have a diameter range between 0.05 and 5 μm. If a fiber diameter is too large (e.g. 3~4 μm), it might be seen by the free-floating cells as a 2D surface. Cells would then be more likely to adhere to single fibers only rather than interacting with multiple fibers, and incline toward 2D culture rather than 3D culture. This clearly would not comply with the grand assumption of the ECM-based design, which believes that by providing an environment similar to the natural ECM of the targeted cell type, the cells would interact in similar ways to cells in natural tissue. Typically, during cell seeding, it is acceptable to assume a cell would be spherical and have a diameter of 10 μm (Dwane *et al.*, 2013). Submicron fiber diameter can be assessed using a scanning electron microscope (SEM), transmission electron microscope (TEM), or atomic force microscope (AFM).

Fiber alignment is the most important and distinguishable feature of an AFS. Since the hypothesis requires aligned fibers to guide cell alignment for the later functional recovery, the degree of fiber alignment should be the most important feature for AFS development. However, due to the nature of the electrospinning process, it is not likely to create perfectly parallel fibers. Furthermore, different collector designs might lead to different AFSs that can be useful for creating different tissues/organs. It is, therefore, essential to investigate into the induced differences and select the most appropriate collection method. The degree of fiber alignment can be easily assessed

using a brightfield microscope, as long as the mounting stage can provide reliable axes for precise measurements.

Fiber hydrophobicity is another issue that requires particular attention because it may affect cell adhesion/viability/migration/proliferation (Walboomers & Jansen, 2001). Different cell types have different preferences over the surface they attach to. If the scaffold hydrophobicity changes due to other reasons (e.g. hydrolysis), the cell might no longer prefer the material, resulting in less cell-binding and a reduced cell viability. This would lead to a direct failure of the tissue scaffold. Hydrophobicity of the fiber is usually tested with a contact angle method, but its effect is also exemplified in a agent-releasing profile.

Surface texture and fiber morphology can be discussed together. Surface texture refers to the microstructure of single fibers that the cells would have direct contact with. A well-controlled electrospun membrane would typically have repeatable features; and in general, it is essential to encourage cell migration on smooth fibers. For example, a study showed that surface roughness of around 90.162 ± 38.848 nm may present significantly more human gingival fibroblast attachment on modified high-purity aluminium oxide substrate compared to a polished one with an average surface roughness of 2.736 ± 0.471 (Leong *et al.*, 2008). Different fibers can be produced to meet specific requirements, however, such as beaded, porous, and core-shell fibers. Surface texture can be illustrated using SEM. The choice of surface texture depends on the ultimate goal of the tissue culture. Fiber morphology, on the other hand, is a global assessment of the membrane feature, which has direct effects on cell polarity, migration, and penetration. It is an important factor for consideration that may vary significantly from one tissue to another. For example, pores of a diameter of 20 μm would be

desirable for hepatocytes, but 90-360 μm pores would be preferred for fibroblast culture (Leong *et al.*, 2008). The effect of fiber morphology can be evaluated from void space or porosity analysis. If cells form a cluster upon the first contact with the scaffold, it is likely that they would not migrate into the interior of the scaffold, and thus would compete for nutrients with each other. As time goes on, the local medium would become more acidic, and events for contact inhibition would increase as the cell cluster proliferates. These would eventually lead to a decline in cell viability. Fiber morphology also sets the limit for general diffusion for nutrients, wastes, or other molecules, particularly when the scaffold is not porous enough. Limited supply for oxygen, for example, would directly decrease the viability of the cells, and toxic substances can build up over time. Morphology, however, is not totally independent from texture of the fiber. Beaded fiber, for example, could use up lots of the interfibrillar space, therefore reducing the overall porosity. Orientation or alignment of the fiber can also affect the formation of cell clusters and cell morphology. Quantitative assessment for fiber morphology is difficult, however, due to the fact that it is the feature that shows the highest variance from one electrospun sample to another. Micro optical tomography (micro-CT) might help analyze fiber morphology, but AFS are in general submicron in fiber diameter and interfiber spacing, pushing the limit for its resolution. It would also be desirable if there was a method that can help predict the overall scaffold porosity from the analysis of fiber morphology. Such a method could significantly save time and cost on scaffold manufacturing and speed up the cell-culture process. This could be an important feature in AFS to be characterized for cell types that might carry functional recovery, such as the formation of neural networks.

Fiber mechanical properties are important parameters because they are directly related to the material in use and the order of the fibers. Similar to the hydrophobicity issue, cells would prefer a certain range of substrate stiffness, which may be predicted from the original material properties, constitution of the fiber, and the orientation of the fibers. There is, however, a serious challenge to overcome before such information can prove to be most useful in tissue engineering. Although a more traditional (and practical) approach would be to use a uniaxial tensile stress testing machine for such information, it is important to keep in mind whether it is the microscopic/single-fiber property or the macroscopic/bundled-fiber property that is tested. Recent development of a nanoindent method could be useful in illuminating the difference between the two, allowing a more accurate predication.

Lastly, the **thickness** of the electrospun membrane directly influences the way the mature tissue can be implemented into patients. Any design of a scaffold has to take into consideration how the surgeons will operate on it. If the scaffold itself is too fragile, it would not be transferable. Cell-culture on this type of membrane might also be seen as 2D instead of 3D culture. On the other hand, if the scaffold is too thick, it would introduce many issues into tissue culture. One major drawback could be the reduced diffusion of substances. This would be critical in the case where natural or induced vascularisation is unlikely. For electrospinning, another existing issue related to sample thickness is the uneven distribution of the fibers. If the fibers are collected in a normal, random manner after a long period (e.g. 30 minutes), it becomes apparent that the central portion of the scaffold becomes much thicker than the outer fibers. This is because the fibers, once they leave the Taylor cone, start to deposit in a Guassian-like manner. For a short period of time, the fiber density might be evenly distributed. But as

time goes on, the differences in local fiber density become more and more obvious. A commonly acceptable solution to this problem is to stack up several membranes that are each manufactured in a short period of time. However, the gap between the membranes becomes a difficult issue to control or assess, and this is clearly not the best solution to create equally distributed fibrillar membranes. This is also one of the reasons for looking into other designs of the grounded collectors. Lastly, the thicker the sample is, the more difficult the characterization process becomes. A full 3D sample (meaning the sample is far thicker than the size of a single layer of cells) would make it hard for the incidental beam to penetrate. Scattered signals are also absorbed and lost into the samples. The reduction of the signal-to-noise ratio (SNR) makes it unlikely to have highly precise and quantifiable data to be characterized for almost any method that is available. This is one of the ultimate challenges for AFS characterization.

In summary, several technical challenges are involved in the complete characterization of AFS engineered product:

1. Properties of the nanofiber
2. Fiber alignment
3. Resolution of recorded data
4. Penetration for thick samples
5. Tissue-culture-related properties

These challenging issues directly limit the characterization powers of current methods, so multiple methods are required for a complete analysis that may pass the final regulation. They significantly prolong the whole tissue engineering process and increases the time and cost. Most importantly, the sample can be easily contaminated or

destroyed during the characterization process, making it difficult to deliver a reliable AFS product at the transplantation stage of tissue engineering. If there is one method that could tackle all of them simultaneously, it could simplify the necessary works, accelerate the production cycle, and create new standards for quality control.

2.7 Fluorescent microscopy as a scaffold characterization method

As mentioned earlier, clinical measurements are necessary for successful functional recovery and are not totally excluded from the developmental phase of an AFS product. One approach that may simultaneously satisfy these conditions would be using quantitative fluorescent imaging. There are usually two outcomes when light meets a medium/tissue; it either gets absorbed or scattered, as depicted in Figure 2.3 (Morgan *et al.*, 2013a, p.5). This forms the principles of various optical techniques including fluorescent imaging. Fluorescent microscopy has a long established use in biology, versatility in sample preparation, and multi-channel recording. It relies on the phenomenon that when certain molecules are exposed to light of a specific wavelength, they will emit light of a lower energy but increased wavelength (a detailed discussion of this principle is below). These interactions are highly related to the molecular composition and the microstructure of the tissue involved (Georgakoudi *et al.*, 2008). The most common type is the widefield epifluorescence microscope (see Figure 2.4 for a schematic diagram) (Morgan *et al.*, 2013a, p.33), which uses the same objective lens to both produce the focal plane and collect the emitted light. A proper selection of optical filters can separate this emitted light into different channels. When the channelled photos are matched with selected lookup table, the photos can be merged to

form coloured images. This multi-colour nature is the core strength of using fluorescent microscopes in biology, and it becomes particularly powerful when the colours themselves contain particular information. If the signal from the AFS is displayed in one channel whereas the signal from the cultured cells (whether they are stained or not), it is possible to acquire some of the most important information regarding

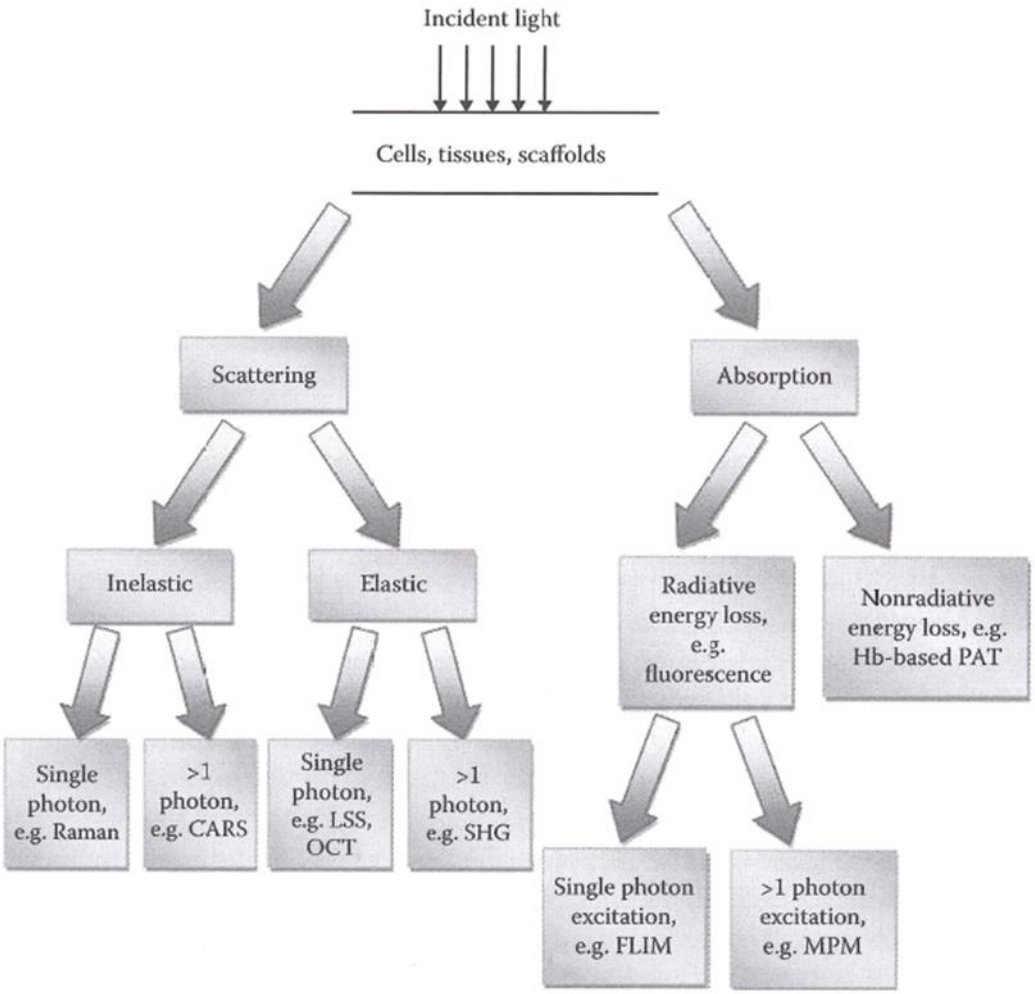

Figure 2.3: Interactions of light with tissue. CARS—coherent anti-Stoke Raman spectroscopy; LSS—light scattering spectroscopy; OCT—optical coherence tomography; SHG—second harmonic generation; FILM—fluorescence lifetime imaging; MPM—multiphoton microscopy; PAT—photoacoustic tomography. *Source: (Morgan et al., 2013a, p.5).*

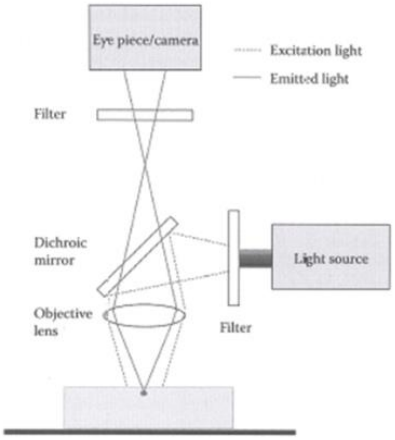

Figure 2.4: Schematic diagram of a widefield epifluorescent microscope.
Source: (Morgan et al., 2013a, p.33).

cell-substrate interactions, which helps to determine the success of tissue culture.

2.8 Signals from autofluorescent biological molecules

For the observation of cell-substrate interaction, endogenous fluorescence from existing biological molecules inside the scaffold/tissue is an important feature. The excitation and emission maxima of a number of common biological molecules is summarized in Table 2.1 (Morgan *et al.*, 2013a, p.46). Fluorescent microscopy by its own single-photon excitation is already capable of detecting the presence of some molecules in the extracellular matrix. Collagen, for example, more likely gives autofluorescence in the blue channel (with maximum emission wavelength between 305-450 nm). Although this autofluorescence seems to be promising to be incorporated into scaffold characterization, one major drawback is that several biological molecules

share similar ranges of emission wavelength, making them difficult to be separated from one another in linear optical imaging (thus without enough specification for identity).

Molecule	Maximum Excitation Wavelength (λ = nm)	Maximum Emission Wavelength (λ = nm)
Collagen	270-370	305-450
Elastin	300-340	420-460
Flavins	375-450	520-550
Lipofuscin	340-390	430-490
NADH	350	450
NADPH	336	464
Phenylalanine	257	282
Retinol	325	400
Tyrosine	283	305
Tryptophan	280	350

Table 2.1: Excitation/emission wavelengths of some common biological molecules. *Source: (Morgan et al., 2013a, p.46).*

2.9 Staining methods that may be employed for tissue characterization

There are lots of chemical stains that have been developed to enrich the works with fluorescent microscopes for cell/tissue characterization. Nile Red, for example, can label intracellular lipids (Greenspan *et al.*, 1985). The emergence of immunohistochemistry, or specific detection of molecules using antibodies conjugated with fluorophores, significantly advanced the field of biology by allowing direct labelling of marker proteins of particular cell types. This helps the researcher to keep on track of cell populations or to monitor cells in different cell cycles. More recently, there were a number of specific fluorescent probes that can be used to monitor dynamic processes in living cells, and direct visualization over their responses to changing

environments became possible (Tsien, 1989). In recent years, the discovery of green fluorescent protein (GFP) from jelly fish (Shimomura *et al.*, 1962) and the cloning of the GFP gene (Prasher *et al.*, 1992) meant that scientists can now modify cells for the expression of proteins that include a fluorescent tag. This has made it convenient for researchers to study intermolecular interactions and subcellular localization using live cells (Shaner *et al.*, 2005). Lastly, the development of quantum dot with various colours creates the bridge between fluorescent microscopy and nanotechnology. Considering that in recent years the scaffold manufacturing methods have become finer, targeting to create nano-scale substrates to promote more natural cell-ECM interaction, the use of quantum dot can be seen as a powerful tool for the observation of substrate (Bagherzadeh *et al.*, 2013) and agent release. The availability of these many tools makes fluorescent microscopy the most prominent choice for the examination of whether a cultured tissue is matured in terms of its cellular activities.

2.10 Drawbacks with the epifluorescence microscope

Although a conventional fluorescent microscope can offer much information about the cultured tissue, its usage in tissue engineering is more often limited by the way the sample imaging should be conducted. If the ultimate goal for tissue characterization is to observe the cultured tissue and its interaction with the patient's physiological system, there will be a significant limitation on the use of staining with fluorescent probes because they are likely to influence physiological responses. More importantly, the image section has to be three-dimensional because most tissue scaffolds are made for transplantation so will be 3D scaffolds readily cultured with live

cells. Commercial epifluorescence microscopes, however, would generate a 3D image that is too blurry to give useful information because the information that is in the light path but out of the focal plane is also collected. Upon excitation, the entire specimen that is laid in the optical path is illuminated simultaneously, and the signal from every excited fluorophore is recorded, including the ones outside the focal plane. This generates a very strong background to overload the depth of the field that is allowed by the objective, reducing the axial resolution and making the image lose contrast. This limitation is further enhanced by the fact that the incoming light from the mercury lamp cannot penetrate deeper, either for the development of the *in vitro* samples or for the clinical assessment of the transplanted tissue. These drawbacks lead to the creation of the more advanced fluorescent microscopes— confocal laser scanning microscope (CLSM) and multiphoton microscope (MPM).

2.11 Confocal laser scanning microscope (CLSM)

CLSM is a modified fluorescent microscope that is targeted to solve the above cons of the conventional epifluorescent microscope. It involves two significant modifications—the use of a monochromatic laser as the excitation light source and pinholes that allow the light progresses in certain paths to go through. The monochromatic laser (contrary to the mercury lamp) allows the user to choose very specific excitation wavelengths, which leads to a more versatile combination of fluorophores to be used simultaneously. The pinhole in front of the laser source ensures that only one point within a specimen is lit at any time point, thus eliminating stray lateral light that will interfere and reduce resultant image contrast. Another pinhole in a

plane is conjugated to the focal plane in front of the detector to limit the majority of the reflected light that comes from regions above or below the focal plane inside the sample. The size of the detector pinhole determines the thickness of the optical section viewed (thus in CLSM the volumetric information in not limited by the depth of the field given by the objective, but by the detector pinhole). The smaller the pinhole is, the thinner the axial thickness of the image at the cost of a reduced signal-to-noise ratio.

At the core of whether a particular design of microscope is more useful than others is the resolution it can offer. Resolution can be defined as the minimum distance between two separate points in the field of view that can be distinguished as two distinct entities. If two objects are separated by a distance smaller than this, they would appear blurred and become impossible to differentiate. In digital imaging, they are likely to be merged into the same pixel, resulting in loss of information. Resolution is mainly determined by the numerical aperture (NA) of the objective, and a greater NA tends to yield better resolution (less loss of information). However, resolution is also influenced by many other factors, such as the wavelength of the light (both excitation and emission, the size of the pinhole, and the pixel/voxel setting used in recording. In general, CLSM can reach 200 nm for lateral resolution and 900 nm for axial resolution, which would be ideal for cell imaging but insufficient for scaffold visualization.

Also, sample thickness is a significant limitation for CLSM to go 3D. If the sample depths are greater than 5 µm, the lateral contrast starts to be sacrificed and further reduced to that of the epifluorescent microscope (Morgan *et al.*, 2013a, p.36). Aside from that, 3D images from CLSM are constructed by stacking many 2D slices on top of each other. This is called “optical sectioning”, which allows the viewer to observe the interior of the sample without the need to physically disrupt it. Such a technique,

however, is limited by many other factors. The working distance of the objective imposes an upper limit because if the objective touches the sample physically, it directly disrupts the imaging process. Also, the depth of penetration is restricted by the sample's natural absorption capability of the excitation energy and its scattering of both excitation and emission lights. This challenge is naturally elevated as the imaging depth increases. The mismatch of refractive indices between the sample medium and the objective immersion medium would also cause the detected signal to be reduced. As a result, a proper selection of the objective and immersion media is the key to extend the imaging depth. Lastly, if the excitation wavelength is shorter (e.g. ultraviolet range), the excitation beam would more likely become scattered away rather than penetrate into the sample. Many papers have reported that the sample prepared for CLSM cannot be larger than 100 μm in thickness because that is how much depth the ultraviolet laser can penetrate. The excitation wavelength, therefore, would set the lower limit for the depth to be visualized. With a properly created sample and optimized optical environment, the imaging depth for CLSM should be between 50 to 100 μm, mainly determined by the nature of the sample. As a result, CLSM would find limited use in 3D imaging despite its apparent improvements.

Photobleaching, which is the irreversible destruction of a fluorophore from its exposure to light, occurs when electrons are, while in their excited state, modified by interactions with other molecules within the environment. This prevents the electrons from returning to the ground state, such that they are not able to emit light. The excitation/emission life cycle of a fluorophore can be variable, depending on both the nature of the fluorophore and the local environment. Phototoxicity is another issue that arises when the excited electron reacts with molecular oxygen that is found in the local

environment. A number of reactive oxygen species (ROS) are produced, which may cause significant damage to the cellular structures, resulting in a loss of cell viability or introducing particular difficulties for visualizing live samples (Knight *et al.*, 2003). Even if CLSM is in use, all fluorophores within the laser light path would be excited, causing significant photobleaching and phototoxicity. This is an important consideration when there may be fluorescent sources that are not from the specifically engineered fluorophores. Signals from these fluorophores can diminish fast, causing possible type II error (i.e. false-negative) recording.

2.12 Multiphoton microscopy (MPM)

Fortunately, the newly-emerged multiphoton microscopy (or two-photon excitation microscopy, the title based on its design principle), is able to bypass or improve upon many of the issues mentioned above for 3D tissue imaging, thus having the potential to serve as a clinical assessment for transplanted tissue and its physiological function. The two-photon excitation theory first appeared in Maria Göppert-Mayer's paper (1931), which proposed that photons of lesser energy together can cause an excitation "normally" produced by the absorption of a single photon of higher energy. Later, as commercial "turnkey" laser become available, and mode-locking became controlled at ease, the theory was finally able to be realized, creating an imaging tool closest to the fluorescent microscope to give full 3D imaging.

The mechanism behind two-photon excitation is based on the assumption that simultaneous (within 10^{-18} s) absorption of energy from two photons, each providing half of the total energy required to induce fluorescence, can generate the same amount

of energy needed for fluorescent emission to occur. This generated emission is called two-photon excited fluorescence (TPEF) and can be explained using the Jablonski diagram in Figure 2.5 (Morgan *et al.*, 2013a, p.36). The excitation wavelength can be longer than the emission wavelength, providing an anti-Stokes shift. Mode-locking makes sure that the density of photon is high at the focal point but falls off sharply above and below this 2D plane. Therefore, only fluorophores in the focal plane are excited, providing a similar or even better control than that of the CLSM. Due to the setting, the excitation can only occur upon the simultaneous absorption of two photos, so the probability that a fluorophore will be excited is highest in the focal plane. For regions 1 µm above or below this plane, excitation events drop to near zero. With this mechanism, photobleaching and phototoxicity issues are limited only to the region inside the focal plane (or more specifically, the depth of field). Therefore, samples can be visualized for a longer period, and type II error is significantly reduced.

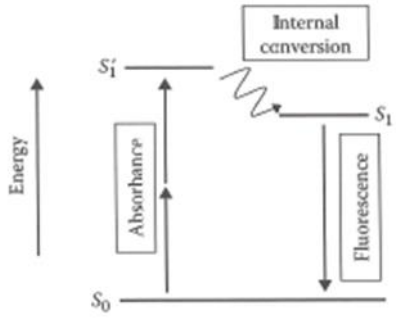

Figure 2.5: Jablonski diagram of two-photon excitation. *Source: (Morgan et al., 2013a, p.36).*

Compared to other microscopes, MPM by its design is more capable of creating high resolution 3D images even for thicker samples. The longer excitation wavelengths can reduce absorption and scattering coefficients in biological tissues. This means that two-photon excitation can go deeper into the sample (Centonze & White, 1998).

Because there is no need for the pinhole anymore, the external (nondescanned) detectors can be placed as close to the collection lens as possible. This greatly extends the penetration depth, one of the most challenging issues in 3D imaging. The use of infrared laser and the extended penetration depth are the keys that make non-invasive 3D AFS characterization possible. More importantly, the high resolution of MPM imaging has made the voxel control subject to what is needed for quantitative characterization. Existing image processing tools may help further enhance SNR, analyse the quantifiable data, and distinguish scaffold/tissue features that are not observed previously. As a result, advances in resolution and penetration make MPM a highly promising tool in 3D AFS tissue engineering, whether it is *in vitro* or *in vivo*.

2.13 Second harmonic generation (SHG) imaging

Although the specs of MPM are specialized in 3D deep tissue imaging, its potential in non-invasive imaging is dependent on a material-specific fluorescent signal called second harmonic generation (SHG). SHG microscopy emerged as a high-resolution optical imaging technique in the late 1990s, roughly 10 years after the pioneered work on two-photon excited fluorescence (TPEF) by Professor Watt Webb of Cornell University (Denk *et al.*, 1990, Zipfel *et al.*, 2003). SHG is a nonlinear optical (NLO) effect that was discovered by Franken, *et al.* (1961). Soon in 1971 it was found that biological molecules such as collagen can also produce SHG (Fine & Hansen, 1971, Xiyi & Campagnola, 2013). The initial suggestion for SHG as an imaging tool was made by Colin Sheppard. Isaac Freund and his colleagues then published a study on the collagen fiber structure in rat-tail tendon using SHG polarization analysis. SHG has also

been use on sensing membrane potential. Over the years the resolution of SHG imaging has been improved dramatically due to the use of mode-locked lasers. Thereafter, SHG imaging has been mainly developed in two directions: (1) exogenous staining with fluorescent dyes for potential sensing in cell membranes, and (2) endogenous imaging of tissues. It can be expected that if an AFS is fabricated with SHG-capable materials, it can take this advantage further to provide scaffold imaging during development and functional assessment during a clinical trial.

The material response to an applied electric field *F* (such as light) is often described by polarization P:

$$P = \chi^{(1)}F^1 + \chi^{(2)}F^2 + \chi^{(3)}F^3 + \cdots \quad (2.1)$$

where $\chi^{(n)}$ is the nth-order nonlinear susceptibility. Each term in Equation 2.1 represents a particular optical signal that might be used for the characterization of the scaffold material. The nonlinear effects are contributed from the terms where n > 1. The tensor $\chi^{(n)}$ decreases dramatically with increasing n, meaning that the higher-order nonlinear processes are relatively weak (and probably negligible) responses to the driving optical waves. $\chi^{(1)}$ can be seen as the linear response of the material to the optical field, often used to explain linear (or one-photon) absorption and the index of refraction. SHG is governed by the $\chi^{(2)}$ term. Aside from SHG, there are also THG signals governed by the term $\chi^{(3)}$, which can be incorporated into the system to provide even more information regarding the innate property of some scaffolds. The

incorporation of higher-order susceptibilities would be a good addition to further empower the MPM characterization method.

In SHG imaging, photon emission at the harmonic frequency 2ω is generated from the second-order nonlinear interaction between the fundamental optical wave of frequency ω and the nonlinear material. Molecules exposed to the incoming electric field need to possess a dipole moment that ensures the production of a harmonic optical wave component from the nonsymmetrical oscillation of the electrons in response to the symmetrically oscillating driving wave. Therefore, effective SHG requires that the molecules of the medium have a permanent dipole moment and nonzero hyperpolarizability, and the dipole moments should be aligned at the bulk level (e.g. the focal volume).

One major difference between SHG and the other prominent, incoherent process TPEF is the emission directionality. SHG has a phase relationship with the laser and a well-defined emission directionality, which is not found in either single or multiphoton excitation. Traditional phase matching conditions used to characterize strictly coherent processes would be $\Delta k = k_{2\omega} - 2k_{\omega} = 0$, where $k_{2\omega}$ is the wave vector for SHG photon and k_{ω} is the wave vector for the incidental photon (LaComb *et al.*, 2008). Due to the polycrystalline nature of collagenous issues, axial momentum is created altering the phase matching condition. The resultant SHG follows the forward direction of the fundamental wave in the limit of perfect phase matching, as achieved in certain uniaxial birefringent crystals. For biological tissues, perfect phase matching can never be achieved because no type I phase-matching conditions exist (hence no matching of the refractive index of the ordinary wave of the SHG with the extraordinary wave of the fundamental). The minimum phase mismatch is the dispersion in refractive index

between the fundamental wavelength and that of the SHG. It is also worth noting that the molecules that are being imaged (e.g. collagen or elastin) are not perfectly aligned in tissue. Such a SHG signal varies according to Equation 2.2:

$$I_{\mathrm{SHG}} \propto \sin\left(\frac{m\Delta kL}{2}\right) \tag{2.2}$$

where m is an integer and L is the coherence length (Mertz & Moreaux, 2001, LaComb *et al.*, 2008). As a result of a decrease in SHG conversion efficiency, some backward SHG signal is also produced due to the need to conserve momentum. The value of Δk would be primarily responsible for driving the SHG signal forward or backward. The smaller Δk is, the more likely the resultant SHG will be in the forward direction. This means that while using SHG for image acquisition of biological molecules, it is important to consider the proportions of how much signal would be driven forward into the photo sensor. For the upright MPM used in this report, the weaker backward signals are collected for analysis; hence, there is a specific need to enhance the signal against the background.

Also, a laser beam focused by an objective should no longer be seen as a plane wave because it experiences a swift phase anomaly at the focus (Gouy, 1890, Boyd, 1980). This reduces the effective optical momentum along the incidental direction and complicates the phase-matching condition (Feng & Winful, 2001). The eventual SHG beam profile does not match the cone-shaped fundamental beam that propagates from the focal point, so the emission becomes a two-lobe profile for the momentum conservation to be satisfied with its intensity on the propagation axis being minimum (Moreaux *et al.*, 2001). The higher the numerical aperture of the objective, the larger the angle between the lobes. Therefore, the choice of a microscopic objective with a proper

NA becomes an important consideration when collecting SHG image signals. The choice of the NA is dependent on the desired precision of quantification needs. Smaller NA should be used in imaging to reduce errors in later deconvolution processes, which would be reflected in quantification.

In short, SHG signals present a great opportunity for researchers to visualize the AFS microstructure without the need for further staining (therefore being non-invasive). However, it is difficult to control SHG precisely; as such signals are weak and show directionality. One of the challenges for this thesis, therefore, is to prove the idea that such signal can be controlled and further quantified for AFS tissue analysis.

2.14 Summary

In this chapter, an overview of the AFS importance, fabrication and characterization is presented. Electrospinning is the dominant method for creating high quality AFS, whereas MPM seems to be able to provide quantifiable data for the characterization process. These two methods present a straight logic from the manufacture of a multi-purpose AFS to its characterization in a 3D, quantitative, and non-invasive manner fulfilling the needs in both laboratory development and clinical trials. Although other technical issues remain, the incorporation of SHG-capable materials and existing image processing tools may be able to fill in the needed roles for the eventual realization of the strategy. The following chapters, hence, are dedicated to investigating how practical the proposed strategy is, starting from the choice of a highly-applicable biomaterial for electrospinning.

Chapter 3 **Electrospinning of an aligned fibrillar scaffold with controlled release**

3.1 Introduction

In Chapter 2, electrospinning was discussed as a reliable method to create nanofibers. In this chapter, some materials of choice for the proof-of-concept fiber are investigated, assuming that the fiber might participate in agent release and cell culture in the future. Another focus in this chapter is investigation of the limitations of some common scaffold characterization methods that may be used in the scaffold fabrication process.

3.1.1 Electrospinning for nano-fibrillar scaffolds

Nano-fibrillar tissue scaffolds have been made available during the last decade owing to advances in electrospinning and related nano-technologies (Burger *et al.*, 2006). Electrospinning is an old technique that was first observed by Rayleigh in 1897, then studied by Zeleny (1914), and patented by Formhals (1934). Taylor (1969) then laid the theoretical foundation of the electrically driven jet, the most essential part that holds the secrets to the optimization of fibrillar quality. There are various applications using electrospun nanofibers, such as wound-healing dress (Khil *et al.*, 2003, Har-el *et al.*, 2014), agent-release vesicle (Leung *et al.*, 2011), and tissue engineering scaffold (Li *et al.*, 2002) etc. In recent years its usage in medical device invention has received the most attention. One of the driving forces that lead this trend is the development of fiber-alignment methods (Theron *et al.*, 2001, Katta *et al.*, 2004, Li & Xia, 2004, Xu *et al.*, 2004, Yang *et al.*, 2005, Zhong *et al.*, 2006, Corey *et al.*, 2007). For example, Duan *et*

al. (2006) have shown that aligned PLGA-chitosan/PVA fibers collected on a rotating drum can used to culture fibroblasts, which hold a strong potential in skin reconstruction. Bashur *et al.* (2006) studied how fiber diameter and orientation may affect the growth of fibroblasts, which provides some guidance for ligament repair. These studies demonstrate how matured alignment methods can be extremely useful in creating complex tissue from the physical cell-substrate interaction perspective. And considering the complex challenges of tissues such as the blood vessel, spinal cord, and tendon, etc., more functional designs of such aligned tissue scaffold would certainly be desirable in future tissue engineering.

3.1.2 The need for agent-elution in tissue engineering

Controlled agent release has in recent years becomes an important chemical function to be included in scaffold fabrications. Macromolecular drugs such as proteins, peptides, genes, vaccines, nanoparticles, antigens, and growth factors have been encapsulated to induce cellular or physiological effects on many occasions (Johansen *et al.*, 1998, Kumar *et al.*, 2004). Many applications, such as drug formulation, tissue culture and wound healing have benefited from this development in recent years. For instance, the growing knowledge about stem-cell biology leads unveiled the needed growth factors for the stem cells to adhere, proliferate, develop pseudopods, and differentiate. In order to make induced pluripotent cells (iPSCs) differentiate into mature functional Purkinje neurons (Muguruma *et al.*, 2010, Wang *et al.*, 2015), it was necessary to add Fgf2 and insulin to the embryoid bodies (EBs) in a time-sensitive manner in order to activate the endogenous production of Wnt1 and Fgf8 from EBs. In this case, 7 μg/mL insulin was added from Day 0 whereas the 20 ng/mL Fgf2 was added

from Day 1 onward to bias the differentiation towards midbrain-hindbrain regionality. An additional 10 µg/mL cyclopamine was later added to the culture from Day 7 to Day 10 to facilitate dorsalization. The whole cell culture was monitored over 20 days until the Purkinje progenitors were created. From the tissue culture point of view, this protocol would require a certain amount of human labour, and post-differentiation cell transportation and surgical transplantation remain unsolved. It is therefore necessary to deliver the correct dose at the proper timing, preferably on the culturing scaffold *in situ*. Considering the duration of this protocol, such research can benefit from a specifically-designed agent releasing electrospun membrane.

3.1.3 Aliphatic materials in controlled release

Material-controlled agent release is mainly a diffusion event that is highly dynamic with respect to changing degradation (e.g. bulk or surface erosion) of the encapsulating fibrillar scaffold typically made from aliphatic materials. When a fibrillar scaffold is designed as a controlled-release vessel for a peptide-based agent, it is necessary to evaluate the type of degradation/erosion it possesses and match the timing with the cell culture protocol. This kind of biomaterial properties of polymeric materials were discussed in detail by Vert *et al.* (1992). A classic example is the analysis of agent release from poly(D,L-lactic-co-glycolide) (PLGA) fibers (Gaspar *et al.*, 1998, Govender *et al.*, 1999, Hutmacher, 2000, Jain, 2000, Bilati *et al.*, 2005, Kim & Martin, 2006, Mundargi *et al.*, 2008). This material is basically a co-polymer of Poly(lactic acid) (PLA) and poly(glycolic acid) (PGA) at a designated ratio. They are synthetic and bioerodible polymers (Ratner *et al.*, 2004, pp.120-121). PLA is relatively more hydrophobic and was intensively investigated by various groups (Gilding & Reed, 1979,

Reed & Gilding, 1981, Kim *et al.*, 2003). Chen *et al.* (2000) utilized secondary ion mass spectrometry (SIMS) to study the degradation of PGA. It is worth noting that no linear relationship exists between the ratios of lactic acid to glycolic acid. PGA is highly crystalline, yet rapidly lose its crystallinity in copolymers with lactic acid. It was found that 50:50 copolymers degrade more rapidly than either PGA or PLA alone. In other words, by adjusting the ratio of the two polymers, it is possible to lock on certain release durations, as discussed by Makadia and Siegel (2011). This illustrates the usefulness of release control simply from the choice of material. PLGA also has the potential for successful cell adhesion. Li *et al.*(2002) presented an electrospun PLGA scaffold that supported adhesion and proliferation of human mesenchymal stem cells. They discovered that the cells could maintain a normal phenotypic shape and proliferate in the nano-fibrillar network after 7 days of culture. PLGA therefore is also an excellent choice for initial testing of cell viability.

Although PLGA has proven to be useful for many applications, the material suffers from certain drawbacks in tissue culture. One significant drawback is that its degradation products are relatively strong acids that even though they would eventually be reabsorbed in a natural way, they could cause changes in local pH, which may delay more cell proliferation (Li *et al.*, 2002). This local drop in pH could also cause damage to the medical device or surrounding cells and may delay the inflammatory response (Bergsma *et al.*, 1995, Athanasiou *et al.*, 1998). Furthermore, the local pH drop could also cause protein instability. It was shown that the pH in buffered release medium could drop to pH3 if the medium was not changed, which may result in severe hydrolysis of the loaded proteins (Lu & Park, 1995, Park *et al.*, 1995). Aside from the pH issue, the next drawback is the apparent initial burst release of agent. This

uncontrolled release limits the use of PLGA in the formulation of certain agents (e.g. cancer-related drugs) (Zeng *et al.*, 2003, Kim *et al.*, 2010). Lastly, PLGA as an agent-releasing material may experience incomplete release. The free carboxyl end groups of PLGA chains could cause electrostatic interactions with the protein initially, whereas the non-covalent aggregation and hydrophobic PLGA-protein contact would limit the release in the later stage (Crotts & Park, 1997, Park *et al.*, 1998, Kim & Park, 1999). This shows that the control over the free-end functional groups and the fine-tuning for proper hydrophobicity could possibly lead to a more complete protein release. These drawbacks from PLGA illustrate some of the most critical concerns for using polymeric agent delivery systems. The material of choice is the core element that leads to the realization of this functional design of the scaffold; it should be the first point of interest for the characterization works. Therefore, it is desirable to find some suitable biomaterials that can overcome these shortages while allowing good controls over agent-release.

Polycaprolactone (PCL) is one of the well-accepted biomaterials of choice. A number of agent-delivery devices that are fabricated with PCL have received FDA approval and CE Mark registration, indicating that the material has a faster venue toward markets (Woodruff & Hutmacher, 2010). PCL degrades at a slower pace than PLA, thus has been used in drug eluting devices that need to remain active for over one year (Ratner *et al.*, 2004, pp.118-119). In long-term degradation in water, PCL seems to create a highly stable environment in terms of pH control (Dziadek *et al.*, 2015). The degradation mechanism of PCL, therefore, has been well established (Pitt *et al.*, 1979, eds. Langer & Chasin, 1990, p.71). It was also found that with an initial crystallinity of 59 %, it displayed a steady drug release rate and it is possible to release over 200 days.

Based on a study of the Capronor system, a commercial implantable contraceptive device made of PCL, the material is generally regarded as nontoxic and tissue compatible. ε-Hydroxycaproic acid (or 6-hydroxyhexanoic acid) is derived from complete hydrolysis of the polymer and enters the caprolactam degradation pathway, it then becomes adipate semialdehyde and is later degraded into acetoacetate in the liver (Li *et al.*, 2012a). The biocompatibility of PCL was confirmed by Orchel *et al.* (2010) when they observed a normal fibroblast culture under the influence of 6-hydroxyhexanoid acid. Furthermore, the highly adaptive PCL can be blended with other polymers to improve stress performance, dyeability and adhesion. Copolymers of PCL can be formed using many monomers, such as ethylene oxide, polyvinylchloride, chloroprene, and polystyrene (Sinha *et al.*, 2004). Cao and Choichet (1999) found that PCL by itself was capable of encapsulating more ovalbumin (OVAs) [which served as a model of nerve growth factor (NGF) in their study] than PLGA 50/50 due to its faster precipitating nature. Later, Valmikinathan *et al.* (2009) created a PCL electrospun fiber that was blended with bovine serum albumin (BSA) for the release of NGF. The sustained release of NGF lasted for at least 28 days, and enzyme linked immune sorbent assays (ELISA) and PC12 cell based bioassays confirmed that the NGF remained active enough to induce neurite outgrowth. This shows that PCL as an agent-eluting material of choice can be used to delivery peptide-based agents successfully. In summary, PCL should be a promising candidate to improve upon the drawbacks of the PLGA system.

Poly(ethylene oxide) (PEO) is one of the most well-documented materials for adjusting the overall hydrophobicity and agent-release properties of the scaffold. PEO is water-soluble (Hammouda, 2006), so would not only alter the hydrophobicity of the scaffold but also serve as a proper reservoir for peptide agents. It can be expected that

by blending a certain amount of PEO with PCL in electrospinning, cell adhesion on the resultant scaffold may be dramatically improved. PEO has a well-contained molecular weight and has been used in the modification of other polymer materials in agent release (Li *et al.*, 2006, Heunis *et al.*, 2011, Song *et al.*, 2011). PEO can also be added to aid the electrospinning of collagen fibers (Huang *et al.*, 2001). The molecule is known as polyethylene glycol (PEG) when it is presented in the form of smaller molecular weight. PEG is involved in an important process called PEGylation, which may mask the released agent from the host's immune system and increase the hydrodynamic size to prolong its circulatory time *in vivo* (Harris & Chess, 2003). Thus, PEO is generally deemed an inactive ingredient for medical use; but in clinical use, PEO is also known for suppressing protein adhesion and is used as an anti-inflammatory polymeric coating (Wörz *et al.*, 2012). With a wide-range of available choices in molecular weight, PEO is a good testing material for fine-tuning other materials involved in the fabrication of electrospun membranes (Andersson *et al.*, 2014). Fabrication with PEO would present an opportunity to enrich the scaffold function and preserve the activity of the agent.

3.1.4 Compartmentalization in agent-eluting fibers

Aside from degradation of materials, another determining factor for agent release rate is the possible compartmentalization of the agent inside the fiber. One prominent electrospinning method to intentionally create compartmentalization is called co-axial spinning. The agent is either released from the core compartment of one material or from the shell compartment of another material. Several goals are achieved through this design: (1) better protection of the agent during formulation/fabrication, (2) provision of an extra control over the release rate, and (3) release of multiple agents

simultaneously. This method was first published by Loscertales, *et al.* (2002) and was investigated further by several groups (Huang & Yang, 2006, Jiang *et al.*, 2006, Zhang *et al.*, 2006, Yarin *et al.*, 2007, Yang *et al.*, 2008, Su *et al.*, 2012, Qu *et al.*, 2013, Rubert *et al.*, 2014). During electrospinning, the shell acts as a barrier to retard the evaporation of the core solution, so the jet can be kept in the liquid phrase for longer in order to complete a proper elongation process (Zhang *et al.*, 2004, Jiang *et al.*, 2005, Yu *et al.*, 2012). It is also possible to encapsulate some non-spinnable core materials (Sun *et al.*, 2003), allowing flexible agent release designs. As a demonstration of the practical use of co-axial fiber in agent delivery, Rubert *et al.* (2014) presented PCL-PEO co-axial fibers that were employed for basic fibroblast growth factor delivery. They proved that PCL-PEO co-axial fibers could support NIH3T3 fibroblast adhesion, preserve the functionality of growth factors released from the core PEO compartment, and release the agent for 9 days. Although it has been reported extensively and shows high promise, one of the issues that has remained obscure is the mechanism behind agent release from each compartment, and whether it can provide a reliable simultaneous release of multiple agents. Hence, it is interesting to study how peptides were actually released from the core or shell compartment and whether such a release profile is a highly controllable one.

Therefore, three goals are investigated in this chapter: (1) exploring the limitations of some current characterization methods for aligned fibrillar scaffolds, (2) modifying PCL with PEO and see how the change in hydrophobicity would affect agent release, and (3) comparing the controlled release profiles of both co-axial and blended fibers to see which one would give a steady release of the agent content. The results

from this chapter help to illustrate how the material and fabrication method of choice can lead to challenges in selecting the most appropriate characterization methods.

3.2 Materials and methods

3.2.1 Polymers and agents acquisition

Poly(ethylene oxide) (Mv: 900,000 Da), poly-Ɛ-caprolactone (Mw: 70,000-90,000 Da) and bovine-serum albumin-fluorescein isothiocyanate conjugate (BSA-FITC) were acquired from Sigma-Aldrich. 1,1,1,3,3,3-Hexafluoropropan-2-ol (HFIP, 99 %) was purchased from Apollo Scientific. 10 nm silver nanoparticles were obtained from Sigma-Aldrich.

3.2.2 Electrospin apparatus

The electrospinning machine is shown in Figure 3.1. The metallic nozzle in frame A delivered the polymer solution(s) and applied a stable voltage using a high voltage supply system (model 73030DC, Genvolt, U.K.). The flow rates of the polymer solutions were controlled by syringe pumps (Harvard Apparatus Ltd., U.K.). A nitrogen tank was used to supply a homogeneous, horizontal nitrogen flow for atmospheric control. In frame B is a rotating drum (RD) (made by the IBME workshop, University of Oxford), which was used for the collection of aligned electrospun fibers with equivalent diameter distributions. This RD collector was made of stainless steel, with a voltage supply (GW Instek GPS-1850D). The diameter of the rotating drum is 5 cm and the length is 15 cm.

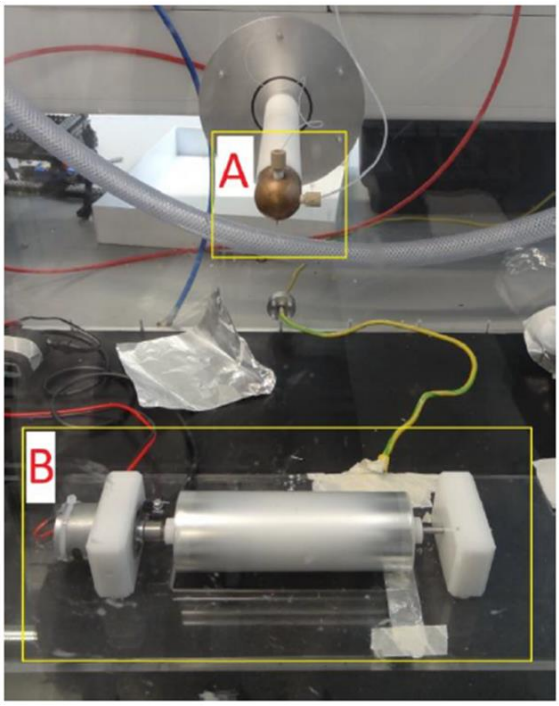

Figure 3.1: The electrospinning machine. Frame A presented the co-axial spinneret. Frame B presented the rotating drum collector.

Two types of nozzles were employed in this machine, as shown in Figure 3.2. One is a single-channel nozzle (A, C), which has an opening of 0.8 mm (internal diameter). This was used for the blended fiber and the pure PCL control. The other is a three-way co-axial nozzle (B, D), which has an opening with an eccentric design. The outer tubing (for the shell solution) has an inner diameter of 0.686 mm and the inner tubing (for the core solution) has an inner diameter of 0.260 mm. This was used for the two co-axial fibers in the experimental group. Panels C & D present the schematics of where the agent will be located inside the co-axial fiber. For the blended or pure PCL control, the agent should be distributed throughout the fiber body. For the co-axial fiber, however, the fiber body would be compartmentalized and the agents would be loaded only in the core compartment.

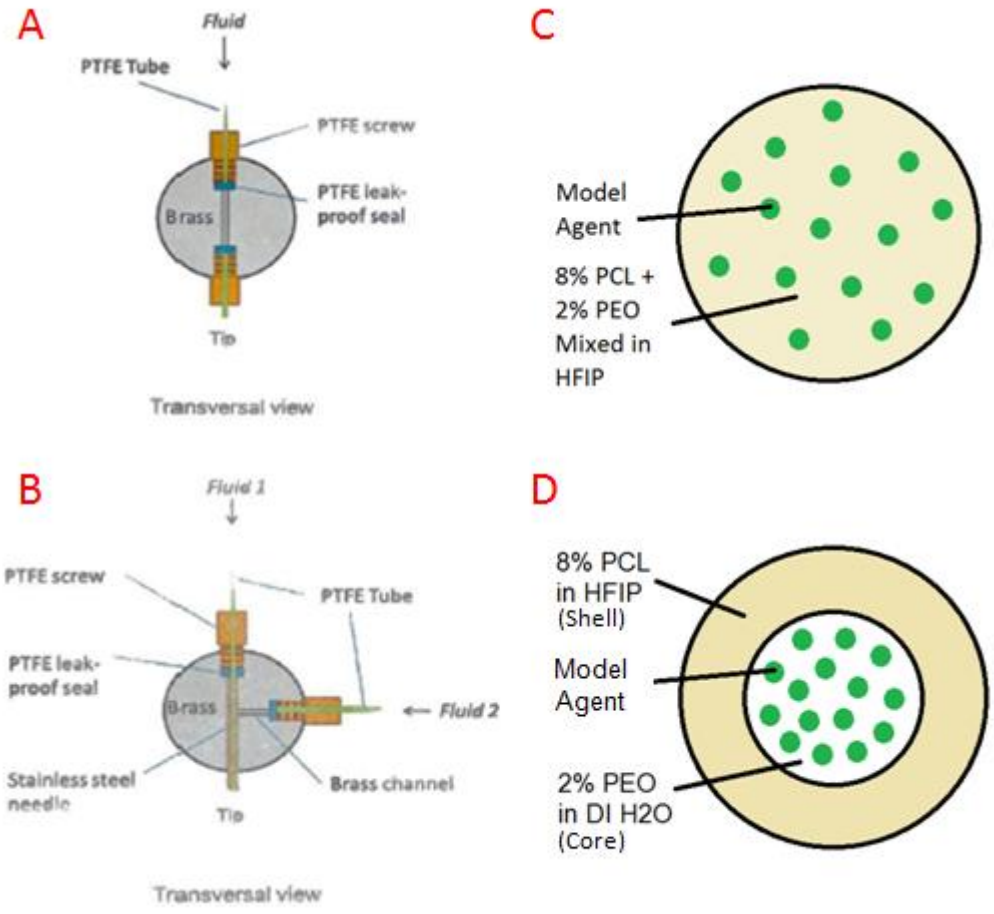

Figure 3.2: The two nozzles used to create the blended and the co-axial fibers. (A) The single-channel nozzle used to create the blended fiber. (B) A three-way nozzle used to create the co-axial fiber. Courtesy of Dr Pierre-Alexis Mouthuy, University of Oxford [figure edited]. **(**C) & (D) represent how the model agents (i.g. silver nanoparticles and BSA-FITC) were loaded in these two fibers.

3.2.3 Electrospinning process

All concentration measurements in this chapter were done in weight by volume (w/v). **For the surface and structural characterization**, two types of electrospun fibers were created as depicted Table 3.1. Silver (Ag) nanoparticles would serve as the loaded agent for the enhancement of visual contrast. The PEO solution consisted of 2 % w/v PEO and 0.1 μmol/mL Silver (Ag) nanoparticles, both dissolved in deionized water (DI H2O). The PCL solution consisted of 8 % w/v PCL dissolved in HFIP. The distance between

the ejecting point and the collecting drum was 17 cm. The pressure of the nitrogen was kept at 1 bar (14 psi). The collecting drum rotated at 2000 rpm in order to create aligned fibers, as used in a published report (Sundaray *et al.*, 2004), and the fibers were collected over a period of one hour individually. Samples from these two Ag-loaded fibers were sent for analyses by scanning and transmission electron microscopies (SEM & TEM). The flow rates of the co-axial fiber were adjusted according to the assumption that the ratio of flow rates would be the same as the ratio of volumes set for the blended fiber.

	Core	Shell	Ag	Voltage (kV)	Flow Rate (mL/hr)
Co-axial	PEO	PCL	Core	10.5	Core = 0.1 Shell = 0.9
Blended	Mixed	Mixed	Mixed	5.0	1.0

Table 3.1: Fabrication conditions for co-axial and blended fibers.

In order to establish the agent delivery profile, four types of electrospun fibers were created as depicted in Table 3.2. The PCL-PEO blended fiber and the pure PCL control fiber were created according to Figure 3.2C, and the two co-axial fibers were designed according to Figure 3.2D. A total of 0.1 % w/v BSA-FITC was loaded in the corresponding compartments. The distance between the ejecting point and the collecting drum was 17 cm. The pressure of the nitrogen was kept at 1 bar (14 psi). The collecting drum rotated at 2000 rpm to cause fiber alignment, and the fibers were collected over a period of one hour.

	Core	Shell	BSA-FITC	Voltage (kV)	Flow Rate (mL/hr)
Co-Ax1	PEO	PCL	Core	18.0	Core = 0.1 Shell = 0.9
Co-Ax2	PEO	PCL	Shell	13.5	Core = 0.1 Shell = 0.9
Blended	Mixed	Mixed	Mixed	5.5	1.0
8% PCL-only	PCL	PCL	Mixed	11.5	1.0

Table 3.2: Experimental conditions for the agent-release study.

3.2.4 Electron microscopy

Scanning electron microscopy (SEM) was used to characterize the surface texture and the diameter distribution of the Ag-loaded fibers. Sample pieces (13 mm in diameter) were cut and mounted onto an aluminium stub via a carbon adhesive sticker. They were then coated with a 2.5 nm layer of platinum introduced by a Cressington 208 HR sputter coater (Vortex Control Systems, Inc., US). A JSM 840F scanning electron microscope (JOEL, Japan) was used to visualize the fibers. Three different areas were observed randomly at magnifications of 2000x, 5000x or 10000x. The diameters, in terms of mean ± population standard deviation from 100 random points on the scaffold, were measured on 5000x images using Nikon NIS-Elements for statistical analysis. A transmission electron microscope (TEM) (JEOL2000FX with an accelerating voltage of 200kV) was also used to discover the locations of the silver nanoparticles and to assess the integrity of the co-axial structure. Both imaging sessions were assisted by research scientists in the Begbroke Science Park (Oxford, United Kingdom).

3.2.5 BSA release study using fluorescent spectrophotometer

Scaffolds were punched into small disks of 13 mm diameter, and their initial weights (data not shown) were measured in order to provide an estimate of how much BSA-FITC actually went into each disc. Afterwards, they were inserted into 2 mL Eppendorf tubes containing 1 mL of PBS solution. Four scaffolds (n = 4) will be tested per sample in order to establish an average dose of release and its sample standard deviation. The tubes were placed on a rotating platform (20 rpm, VWR, Dublin, Ireland) which was relocated to an incubator maintained at 37˚C. The PBS solution was collected for measurement by a fluorescent spectrophotometer and was replaced by fresh PBS solution each time. Twelve time points (by hour) were taken over a duration of 4 days: 0.5, 1, 1.5, 2, 3, 4, 6, 12, 24, 48, 72, 96. At the end of the experiment, the incubated scaffolds were dissolved in 500 μL HFIP individually for a minimum of 48 hours on the rotating platform and the resulting solutions were diluted 1:1 with deionized water before taking measurements. The sum of measurements served as an indicator for the initial C_0 concentrations.

The amount of BSA for each sample was assessed by an excitation wavelength of 495 nm and was measured at the emission wavelength at 535 nm in room temperature. The procedure was performed using a microplate reader (The Wallac 1420 VICTOR2 TM, Perkin Elmer, United States).

3.2.6 Statistics

Fiber diameter that was measured from the SEM images was reported in mean ± population standard deviation (n = 100) in order to further increase the precision. The

diameters of the blended and the co-axial groups were compared using the two-tailed Student's *t*-test with a confidence level of $p < 0.05$. For the agent release study, the concentration of the released agent at each check point was reported in mean ± sample standard deviation (n = 4) to provide an estimate from each formula.

3.3 Results

3.3.1 Characterization of the fiber diameter

The first half of this chapter focuses on validation of the fabricated co-axial fiber with respect to the fiber diameter, morphology, and the intra-fiber locations of silver nanoparticles using SEM and TEM. Figure 3.3 shows the SEM images of the silver-loaded electrospun fibers. On the one hand, the blended fibers had an average diameter of 1.18 ± 0.28 μm. On the other hand, the co-axial fibers had an average diameter of 0.37 ± 0.31 μm. The two-tailed Student's *t* test gave a *t* value of 45, indicating that $p < 0.05$. This thus rejected the null hypothesis that the two groups of fibers came from the

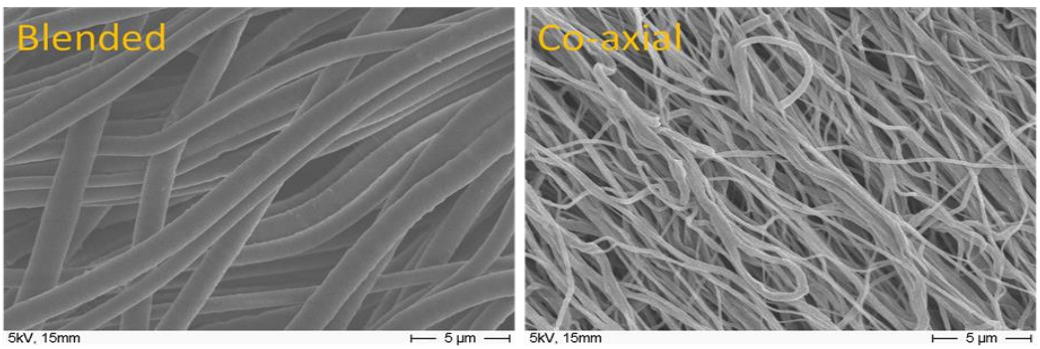

Figure 3.3: Silver-loaded electrospun fibers. LEFT: blended fiber consists of 8% PCL and 2% PEO (volume ratio = 9:1). RIGHT: co-axial fiber consists of an 8% PCL shell and 2% PEO core (flow rates = 9:1). 100 points were selected randomly for statistical analysis.

same population based on comparison of the two diameter distributions. Fibers showed clear orientation in both groups, suggesting that 2000 rpm was fast enough for the RD collector to create a certain degree of alignment for the two fibers.

3.3.2 Characterization of the fiber compartmentalization

The presence of the core compartment was later investigated using silver nanoparticles. Figure 3.4 presents the TEM images of the two types of fibers. Panels A and B represent the blended fiber and panels C and D represent the co-axial fiber.

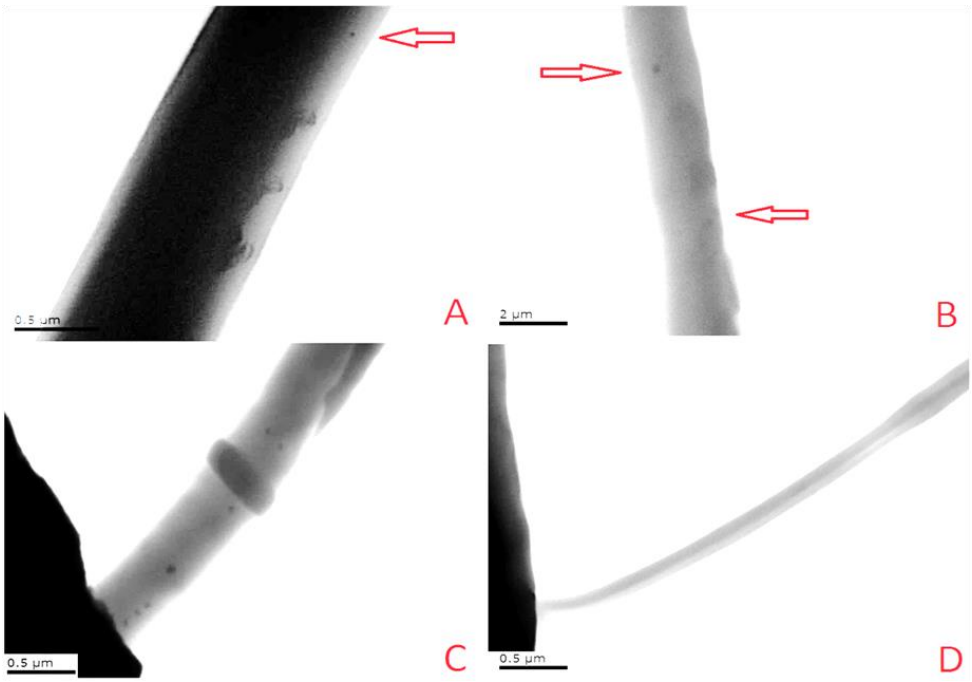

Figure 3.4: TEM images of the fiber structure. Red arrows indicate the locations of silver nanoparticles. A) A blended fiber showing a silver nanoparticle toward the outside of the fiber. B) A blended fiber presenting two nanoparticles, one at the center whereas the other on the peripheral. C) A co-axial fiber displaying several nanoparticles in the central core compartment. D) A co-axial fiber presenting the core and the shell compartments.

Panel A shows a thick blended fiber (~1 μm). The silver nanoparticle was found close to the peripheral of the fiber. This panel also provided some information on how the two polymers were mixed during spinning. The image is obscure because the transmission electron beam had difficulty passing through a fiber of this thickness. To serve as additional proof, in panel B another blended fiber showed nanoparticles located on both the central and the peripheral regions, suggesting that the particles could be found throughout the whole fiber. In panel C, however, the silver nanoparticles were only found in the central region of the fiber. This observation was echoed by panel D, which presents a clear distinction between the core and the shell compartments. Together, panels C and D demonstrated that there existed two different regions in the fiber structure. As a result, the co-axial nozzle was able to properly create the two compartments of the co-axial fiber.

3.3.3 Controlled release profiles

After the qualities of the two fibers were assessed, the agent release profiles of the two fibers were constructed. Figure 3.5 shows the agent delivery profiles constructed on the accumulative release. The four lines were fitted with power curves to establish trendlines, as shown on the figure. The agent release profiles revealed that for the first 24 hours, the BSA release from the core showed a distinguished release rate that was much faster than the other three fibers. This is interesting because it was hypothesized that the PCL shell would provide some shielding effect for the PEO core, therefore delaying the release of BSA-FITC from the core; but the observation showed the opposite. In the previous study, Jiang *et al.* (2005) presented a similar study with a PEG-core/PCL-shell fiber releasing BSA and lysozymes. Their study showed that

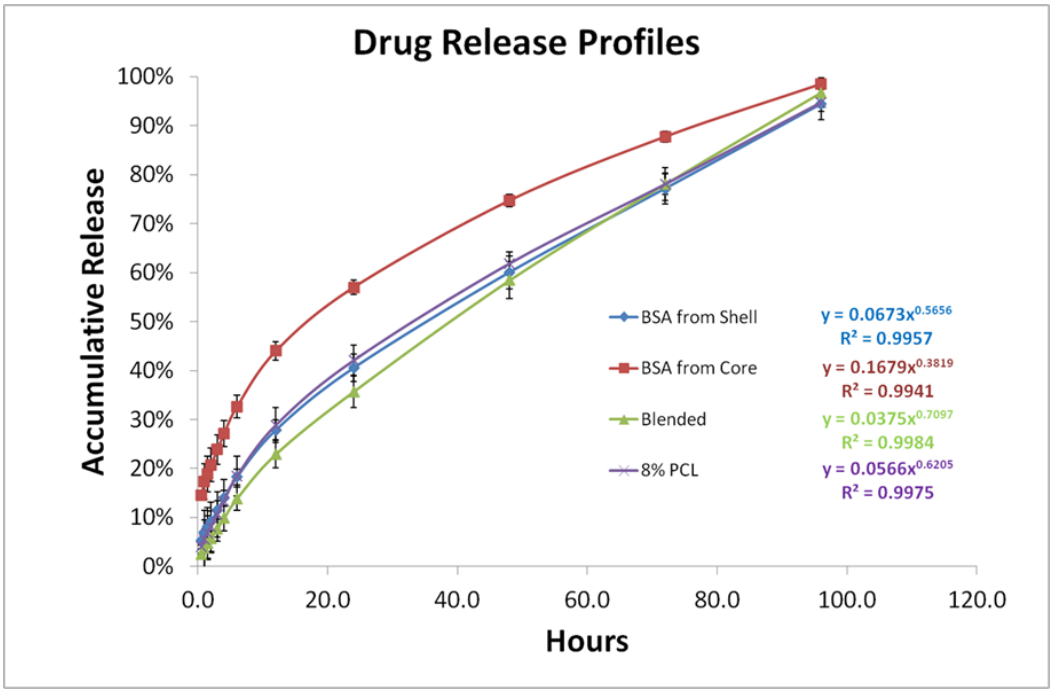

Figure 3.5: Drug release profiles. Protein release from the core (red) showed an apparent burst release during the first 12 hours compared to the other groups. The blended fiber (green) showed a more steady, zero-order-like release.

a larger PEG-core allowed faster agent release. It is difficult, however, to assess their result because several parameters were changed simultaneously in their study (e.g. flow rate, total agent loading, etc.). The study presented in this thesis, on the other hand, was designed to include the same amount of the PEO, PCL and BSA-FITC in the co-axial and blended fibers, therefore simplifying the observation of the quick PEO release. An assumption here is that the PCL shell might experience initial swelling to allow more water access, dissolving PEO and forcing the BSA-FITC to enter a mobile phase. Because the PEO core started to dissolve whereas the PCL shell remained intact, the free-floating BSA-FITCs that were released from the PEO core became faster than the entrapped ones from the PCL shell. This is echoed by the results of Jiang *et al.* (2005), which presented an SEM image of a hollow co-axial fiber that clearly lacked the core PEG material after 24 days. One way to test this assumption is to load the core

compartment with a material that does not dissolve faster than the shell PCL (for example, loading the core region with PCL of the same diameter). This prevents the dissolution of the core material and allows a direct examination of the diffusion from the core region only. If the release rate drops dramatically, it can be shown that dissolving PEO does contribute to the fast release from the core.

3.4 Discussion

3.4.1 Characterization with SEM and TEM

SEM imaging can provide a reliable measurement of the fiber diameters and display the fiber texture and orientation, which are some of the essential information required in scaffold characterization. In Figure 3.3, it was found by SEM analysis that the blended fiber had a more uniformed diameter distribution. This suggests that the Taylor cone generated from the blended solution was stable enough to control the size of the fiber. On average, the blended fiber had a diameter around one micrometer, which is closer to the ideal diameter for promoting cell-fiber adhesion, spreading, and interaction in general (Li *et al.*, 2002, Badami *et al.*, 2006, Bashur *et al.*, 2006, Moroni *et al.*, 2006, Pham *et al.*, 2006, Christopherson *et al.*, 2009). Such a fiber also had more interfibrillar space compared to the co-axial fiber. This larger interfibrillar space would make the blended scaffold more assessable for cell migration. In comparison, the co-axial fiber had a very wide diameter distribution. This indicated that the Taylor cone that created this fiber was unstable. This also limited the size of the interfibrillar space, making this fiber less applicable as a tissue engineering scaffold. The wide variance of fiber size could also lead to an inhomogeneous agent release rate. It is possible that this

phenomenon might create unequal local concentration of the released agent, which is undesirable for whole-tissue maturation. Furthermore, SEM images clearly show that the fibers were oriented toward a certain direction. This proves that SEM is an indispensable tool for the analysis of fiber alignment for future optimization of the fibrillar scaffolds. As a result, considering its usefulness in statistical analysis of the fiber diameter and alignment angle, and the possibility of predications regarding cell culture and controlled release, SEM remains an essential tool for the characterization of fibrillar scaffolds.

The thickness of the fiber has a tremendous effect on the penetration of the TEM beam, which limits TEM's use as a characterization method for electrospun fibers. Several papers have relied on the use of TEM to provide the locations of the loaded nanoparticles for fibers (Li *et al.*, 2003a, Hou & Reneker, 2004, Jiang *et al.*, 2005, An *et al.*, 2009). However, in this report it was found that such a characterization method actually has lots of limitations of its own and may require multiple fields of views for data interpretation. TEM in general requires the sample to be as thin as possible and high quality images can only be generated with sample thickness in the order of tens of nanometers. For example, it requires a sample thickness of 70 nm when conducting a TEM imaging of animal tissue (Cheville & Stasko, 2014), and 1 μm samples are considered too thick to generate enough resolution. As a result, when such a localization of nanoparticle method is in use, it is necessary to draw the conclusion from smaller fibers while ignoring the larger ones. This means that this method, though commonly used, is premised on the speculation that the smaller fibers are representative of the majority of the fibers. This presents a good example to show how difficult it is to characterize an AFS that consists of nano-scale fibers. In order to increase the overall

confidence of co-axial spinning, other characterization methods are needed to provide extra confirmation.

Nevertheless, it is possible to observe the locations of the nanoparticles from TEM images. When the findings from TEM were coupled with SEM, it is convincing that the co-axial fiber was created properly. Figure 3.4 presented some nanoparticles that have been located both at the edge and in the central portion of the blended fiber, indicating that there is no apparent separation of the two materials (thus two chambers). In contrast, the appearances of multiple nanoparticles in the co-axial fiber were found at the central region of the fiber. More importantly, in panel D it is shown that there existed a sharp boundary, which strongly suggested the presences of two compartments. Coupling the findings from SEM, which statistically rejects the idea that the two fibers are from the same population, it should be clear that the co-axial spinning was successful in separating the compartments. Hence, the co-axial nozzle used in this experiment is reliable in creating the fiber that possesses two compartments.

3.4.2 Control of burst release

The burst release exhibited by the core PEO is another important feature in this profile. Burst release in general is an unwanted feature in controlled release because it implies that there is no control at the initial release, easily causing a temporary overdose and toxic effect (Allison, 2008). It is also an indicator that the release duration would be shortened. As a result, many papers have been dedicated to eliminate the initial burst release. Because burst release is a common observation from hydrophobic materials, it is possible that the observed burst release from the PEO core is limited by the hydrophobic PCL shell. One way to examine this model is to switch the shell material

to a hydrophilic substance such as polyvinyl alcohol. This will remove the hydrophobic component (and the burst release effect). If the burst release is eliminated and the PEO core shares a similar delivery rate as others, the delaying effect of the PCL shell will be clear and further analysis can be performed to characterize the degree of delay by factors controlling the PCL shell, including PCL concentration and molecular weight.

An interesting observation is that the blended fiber shows a zero-order-like agent release profile. This observation was supported by the fact that when fitted with a linear trendline, the equation $y = 0.0099x + 0.0589$ yielded a R^2 value of 98.71 %. Such a releasing curve indicates that the formulas used for the blended fiber might be used in another application that requires highly-controlled agent release. The similarity between the BSA from Shell line (blue) and the 8 % PCL line (purple) indicates that the agent release profile from the shell compartment in this formula was comparable to that from a simple 8 % PCL fiber. It is intriguing to compare these two fibers with the blended fiber, which consisted of only 0.2 % of PEO. In a related report by Park *et al.* (2005), modified PCL-PEG micelles were designed for the release of paclitaxel. It was found that such formula created sustained release rate and significantly limited the initial burst release. In another report, Jiang *et al.* (2006) presented a co-axial fiber that consisted of BSA-containing dextran in the core and PCL-PEG mixed at various ratios in the shell. Their report showed that the release rate of BSA increased with the PEG percent in the shell section. This illustrated how the introduction of the relatively hydrophilic PEG-PEO could help to design the agent release profile of the PCL fiber. Considering the need to engineer the PCL fiber to become more hydrophilic for better cell adhesion in tissue culture, it seems possible to mix PCL with other relatively hydrophilic molecules not only to improve on the cell adhesion performance, but also to create a agent-eluting

fiber that may possess a zero-order release profile. If such a blended agent-eluting fiber were aligned to form a fibrillar scaffold, it could become particularly useful for the engineering designs of some highly complex tissues, such as oriented neural networks (Schmidt & Leach, 2003) and tendon bundles (Kannus, 2000).

The formula for the fiber provided a useful agent releasing duration as well. In one of the earlier experiments, Huang and Yang (2006) created a co-axial fiber that enclosed an aqueous solution that contains low-molecular-weight agents in a PCL shell. The lack of a core material meant that the agent delivery was all dependent on free diffusion, making it difficult to control the release rates of the agents. Jiang *et al.* (2005) released BSA in a PEG-PCL co-axial fiber, but it is difficult to conclude the duration of their release profiles since they changed several parameters simultaneously. They also finished the study when one of the fibers (i.e. 0.6 mL/hr) completed only 50 % of the accumulative release, which was not enough to establish a reliable profile since 60 % is the minimum amount to properly apply a power curve to the burst release scenario (Ritger & Peppas, 1987a, Ritger & Peppas, 1987b). In this study, however, both the co-axial and blended fibers almost released the full amount of the BSA-FITC at the end of the fourth day. This indicated that the experiment yielded highly controlled agent release profiles. Such a four-day period is ideal for many applications, including the design of a wound healing mesh or the seeding of the stem cells. Also, all four power curves showed an R^2 value greater than 99 %, indicating that the established predications for the agent releasing rates were representative of the real cases.

3.5 Summary

In this chapter a PCL-based aligned fibrillar scaffold was characterized for its fiber morphology, fabrication validity, and agent-release performance. SEM and TEM were employed for the analysis of the scaffold quality. Agent release profiles from the co-axial and blended PCL-PEO fibers were constructed over a period of 4 days. The results indicated that SEM is an essential method to explore the fiber diameter, texture, and orientation. TEM imaging, however, was quite limited by the fiber thickness to deliver a highly reliable analysis. Nonetheless, comparison of these evidences indicated that co-axial spinning was successful in creating separated compartments for agent loading. Agent release profiles indicated that when the agent was loaded in the core, it actually experienced a faster release compared to the case when the agent was loaded in the shell, possibly due to the decomposition of the core material. An interesting finding is that the blended formula showed a release profile with a much controlled initial burst release. This indicated that by making the fiber material more miscible and hydrophilic, it is possible to create a zero-order agent release. Such aligned an fibrillar scaffold would be highly useful for the engineering of tissues with higher complexity. The insights from this chapter, especially on the material properties, provided enough hints for designing the proof-of-concept fiber in the next chapter.

Chapter 4 **Generation of a prototypic AFS targeting functional recovery**

4.1 Introduction

Following the results presented in Chapter 3, several key issues for AFS design were investigated. Firstly, it was found that agent release is heavily dependent on the material of choice, and the hydrophobicity of the fiber significantly alters the release profile, possibly towards zero-order kinetics. Secondly, it was also found that PCL is an ideal material for cell culture and agent release. Thirdly, it was also found that the use of SEM and TEM contaminates or destroys the scaffold. It will be ideal for researchers if there is an alternative way to acquire information regarding fiber quality and scaffold properties. As mentioned in Chapter 2, a combined use of multiphoton microscopy (MPM) and second harmonic generation (SHG) signalling may be able to provide such a needed method. Therefore, a prototypic AFS that incorporates the above three concepts was designed in this chapter in order to take a step further towards creating a tissue scaffold that leads toward desirable tissue culture and functional transplantation. The chapter then characterizes this AFS for its degree of alignment using two basic collectors in order to determine whether such a fiber possesses desirable features for cell culture

4.1.1 Aspects of fiber fabrication

One of the most effective approaches for characterization is to take advantage of the fiber material itself. If the material itself is able to generate signals that can reveal the surface texture, morphology, density, or even diameter data, it can bypass the need

for electron interactions with the scaffold and potentially prevent destruction during characterization. SHG imaging, though being material specific, may be one of the best methods to realize this approach. Nevertheless, scaffold characterization with SHG might be difficult because (1) the SHG material might alter necessary scaffold properties for tissue culture and (2) the SHG signals might not possess enough quality to yield useful characterization data. Hence, it is essential to select an appropriate material that could satisfy the above two challenges.

4.1.2 Gelatin/collagen as fiber materials

As biomaterials, gelatin and collagen come from the same origin, but the most apparent difference comes from the capability of collagen to form highly aligned ultra-structures, as present in many tissue showing strength and directionality. Fibrillar collagens are made up of repetitive amino acids such as (with glycine-proline-hydroxyproline being the most abundant repeating unit). This left-handed string undergoes extensive post-translational modification in order to form a right-handed coil/triple helix. Collagen is also one of the most abundant biomaterials. Approximately 30 % or more of total protein in the human body consists of collagen (Di Lullo *et al.*, 2002), making it one of the most important materials of choice in regenerative medicine. Xenogeneic collagen also shows low immunogenicity when transplanted into humans (Patino *et al.*, 2003, Bayrak *et al.*, 2013). Therefore, collagen can be seen as a natural, highly ordered, degradable, cell-adhesive biomaterial. It can be expected that if a tissue scaffold is designed with collagen, it can show ample cell-adhesion sites for most cell types, similar mechanical properties as the targeted tissue, low immune responses, and less time for the full integration into human body. But in terms of AFS fabrication,

collagen is a difficult material to be coupled with electrospinning. There are only a limited number of available solvents such as HFIP, glacial acetic acid, or ethanol mixture that might be used for spinning (Matthews *et al.*, 2002, Dong *et al.*, 2009, Chakrapani *et al.*, 2012) But two key issues present. One is that such pure collagen fiber usually does not show uniformity. Beads development and a wider variance in fiber diameter are commonly observed. The other is that, depending on the constitution of the solvent system, it is possible that the collagen can be denatured in the process and lose its promising features in tissue engineering. Although freeze-drying might replace electrospinning for the creation of collagen scaffolds, there is no fiber orientation and the fiber diameter is typically in the micro scale rather than the nano scale, thus with limited applications. For these reasons, alternative methods of using collagen are being explored continuously.

Gelatin, on the other hand, was derived from collagen in a controlled degradation process, which creates fragments that preserve the α-helical structure and the surface peptide sequences. Mammalian gelatin has found wide use as an excipient in pharmaceutical processing (Djagny *et al.*, 2001) or a stabilizer in vaccines (Sakaguchi & Inouye, 2000). Most commonly used forms of gelatin in tissue engineering are derived from porcine (Natu *et al.*, 2007, Lai & Hsieh, 2012) and bovine (Hsu *et al.*, 2013) sources. Clinical reactivity to these gelatin sources have been relatively uncommon (Sakaguchi *et al.*, 1999, Pool *et al.*, 2002, Mullins, 2003), and immune reactivity typically vary with the molecular weight of gelatin in use (Sakai *et al.*, 1998, Kelso, 1999). Molecular weight ranging from 2000 to 10,000 Da would show considerably reduced reactivity with anti-gelatin IgE while maintaining its adsorption blocking activity. Gelatin has also been reported to reduce the potential of an antigenic response

in vivo because it is deficient in both tyrosine and tryptophan, and contains only a small amount of phenylalanine (Gorgieva & Kokol, 2011). As a result from its amino combination, gelatin has a lower potential for forming aromatic radicals that can lead to antigenic responses (Kokare, 2008). Therefore, gelatin can resolve many potential issues with respect to availability and immunity in an early stage of tissue engineering.

When it comes to scaffold fabrication, gelatin is sometimes seen as a reasonable material replacement for collagen. It is naturally derived, commonly used, and economical in manufacturing. Collagen differs from gelatin in that it contains more tertiary structures, leading to a lower aqueous solubility at acidic pH < 5 (Pahuja *et al.*, 2012). This limits the use of collagen in the preparation of polymer solution in electrospinning. On the other hand, the fragmental gelatin molecules are much easier dissolved compared to pure collagen, and therefore easier to form fibers with better controls. In terms of potential interaction with cells, gelatin may help lower the hydrophobicity of some synthetic polymers such as polycaprotactone (PCL) and poly-L-lactic acid (PLLA) (Van Vlierberghe *et al.*, 2011). Depending on the cultured cell type, scaffold materials modified by gelatin may create proper surface hydrophobicity that encourages the developments of focal adhesion and fibrillar adhesion for the cells (Horbett *et al.*, 1988, Dubruel *et al.*, 2007, Van Vlierberghe *et al.*, 2007, Van Vlierberghe *et al.*, 2008b, Campillo-Fernández *et al.*, 2009). Furthermore, mammalian gelatin is rich in domains that can bind to cell-surface receptors (e.g. integrin) and to other extracellular matrix (ECM) proteins, such as fibronectin; it can be seen as a versatile substrate for attachment of adherent cells (Katagiri *et al.*, 2003). With respect to cell adhesion, gelatin has both relevant hydrophilicity and enriched RGD sequences that are essential for successful focal adhesion for most integrins (Klotz & Smith, 1995,

Humphries *et al.*, 2006, Dong *et al.*, 2010). These properties can significantly contribute to cell culture, making gelatin a desirable addition to be embedded into electrospun fibers for tissue engineering. The created electrospun fiber shows a smooth and uniform surface and is therefore useful in generating consistent cell cultures. Nevertheless, mixing gelatin into an AFS design would show little effect on the mechanical strength of the designed tissue (Ghasemi-Mobarakeh *et al.*, 2008). A higher gelatin content can lead to weakened ultimate strength of the tissue. As a result, it is necessary to combine gelatin with other biomaterials in order to generate the needed tissue strength. The amount of gelatin will determine the mechanical properties of the tissue.

4.1.3 Second harmonic generation (SHG) of gelatine/collagen

Another especially valuable advantage of incorporating collagen or gelatin in scaffold design is the fact that they can initiate SHG in MPM imaging. SHG is a coherent light-scattering process that would occur when the incident molecule has a noncentrosymmetric structure (Simpson, 2004, Pena *et al.*, 2005, Haupert & Simpson, 2009). Photon emission at the harmonic frequency 2ω is collected after second-order nonlinear interaction of the fundamental optical wave (ω) and the nonlinear material. SHG can be seen as a coherent second-order light scattering process generating a new wavelength that has twice the frequency of the fundamental wave. More specifically, molecules exposed to the electric field need to possess a dipole moment, which produces a harmonic optical wave component when the non-symmetrical oscillation of the electrons was induced by the symmetrically oscillating driving wave. Effective SHG requires that the molecules of the scaffold have a permanent dipole moment and nonzero hyperpolarizability; at the bulk level (e.g. in the focal volume), the dipole

moments should be aligned in an organized array. Hence, whether there would be SHG signal or not solely depends on the molecular structure presented in the scaffold, and there would be no need for staining to create the fluorescent signal. Theoretically, SHG signal is energy conserving, and hence should not suffer from the effects of phototoxicity or photobleaching (Xi *et al.*, 2008). SHG signals coming from collagen/gelatin have been utilized in experimental designs in several studies (Kim *et al.*, 2000, Bueno *et al.*, 2011, Manickavasagam *et al.*, 2014). For example, Yasui *et al.* (2009) have shown that SHG from collagen can be used to analyze skin microstructure. By using a Cr:forsterite instead of a Ti:sapphire laser for mode-locking, they showed that the SHG signals were promising for even deeper tissue imaging than the conventional range. Considering the number of scaffold designs that have employed gelatin in recent years (Figure 4.1), it is certainly desirable to develop a scaffold

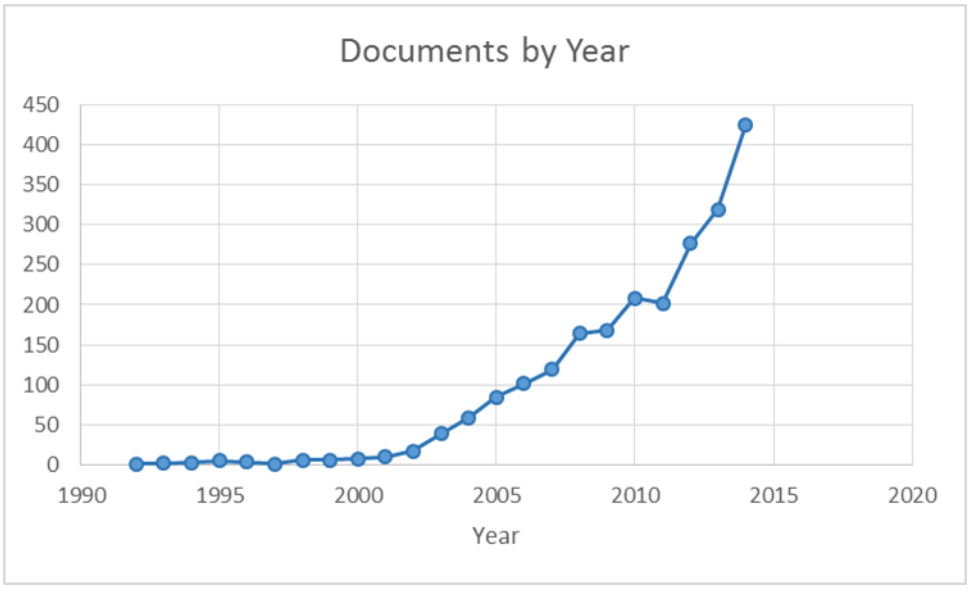

Figure 4.1: Annual number of articles that involve gelatin in scaffold design. Database: Scopus.com. Keywords: scaffold* AND gelatin*. Data range from years 1990 to 2014, accessed on 16th August 2015.

characterization that can take advantage these SHG signals. Therefore, scaffolds designed with gelatin/collagen may enable visualization of the scaffold structure without extra invasive staining works. The best way to illustrate this strategy is through the characterization of scaffold porosity.

4.1.4 Porosity of a scaffold

Porosity of the scaffold is one of the most important features that should be considered early in tissue engineering designs (Zein *et al.*, 2002, Meinel *et al.*, 2004). Porosity is an estimate of the void spaces in a material. It is a fraction of the void volume over the total volume, typically reported in percentage. Because porosity is widely applicable in various fields, its definition can vary and thus requires different methods for assessment, leading to a lack of a universal method for its characterization in materials or scaffolds. Typically, two theoretical approaches are applied while measuring porosity—unit cube analysis and mass technique (Ho & Hutmacher, 2006). The unit cube approach evaluates porosity using volume fraction. It takes linear measurements of the scaffold cube and assumes that the scaffold struts are uniform without fusion of the layers (Zein *et al.*, 2002, Woodfield *et al.*, 2004). The drawback of this method, however, is that it does not take into account experimental issues such as mass transport or material swelling. Imaging techniques such as CT or MPM belong to this category. In mass technique, however, the volume of the scaffold material is derived from the division of the mass of the scaffold over its material density. This technique is applicable for scaffolds with controlled and uncontrolled geometries, but requires precise measurements of the change in total mass. Regarding these, several methods that are based on the Archimedes method and liquid displacement were

developed (Zhang & Ma, 1999, Ma & Zhang, 2001, Ramay & Zhang, 2003). When it comes to pore characterization of electrospun nano-fibrous membranes, methods such as **capillary flow porometry** (CFP) (Bagherzadeh *et al.*, 2013) has become a standard. However, **liquid extrusion porosimetry** (LEP) (Tornello *et al.*, 2014) is more relevant toward a fully 3D AFS, and has been used in literature to provide reasonable estimates of the membrane porosity. CFP and LEP are highly similar to each other, both measuring mainly the through pores. The major difference is that CFP works particularly well on thin membranes where as LEP is more precise on 3D scaffolds. They may serve as a good control for method development when the liquid in use does not cause significant absorption and swelling of the scaffold. A significant drawback, however, is that these tests are likely to contaminate the tested scaffold in the process and prevent further tests on it.

For tissue engineers, there are even more requirements for porosity characterization from the tissue culture side. Fibrillar scaffolds should be biocompatible, with reliable thermal and mechanical properties similar to extracellular matrices (Yang *et al.*, 2001a). It is also necessary to have free diffusion of nutrients and wastes in and out of the scaffold for cells to proliferate normally. Local dead zones could also affect the osmotic pressure or agent diffusion, causing damage to the cells. Furthermore, the scaffold has to be porous enough to allow free cell migration. As the cells proliferate, they would start expanding from the colony and move into free zones. Otherwise, contact inhibition could occur, leading toward pre-maturation of the tissue (Bandtlow *et al.*, 1990, Blakeney *et al.*, 2011). Nevertheless, the most important criteria for choosing the right method would probably be its capability to remain non-destructive and sterile throughout the characterization process. The reason for this is that the whole process of

tissue manufacturing is particularly extensive, involving many follow-up steps (e.g. cell culture, bioreactor incubation, and transplantation) after scaffold characterization until it reaches full tissue maturation. Each of these steps can introduce variances in the scaffold/tissue, therefore decreasing confidence in the final tissue product.

Another concern comes from fabrication of the scaffold, which often renders an established characterization method useless. Considering the eventual need for mass transport, tests that are performed based on mechanical/physical contacts remain the most trusted. However, variations from one fabrication method to another exist, and are usually caused by changes in fiber diameter, surface texture, material properties, and mechanical strength. These changes can put the tested results in questions easily. For electrospun membranes, the best method for porosity assessment is to use CFP. However, when a fully 3D electrospun scaffold is desired, then LEP becomes the more reliable method. The difference between the two scenarios is that in order to make a 3D electrospun scaffold, it is almost necessary to stack up the membranes to increase the volume, which easily exceeds the volume allowance of CFP. Furthermore, the pocket space between the membranes introduces new errors into the estimation. Considering the fact that in tissue engineering, the selected range of the pore size should be more relevant to the cell size, the pocket space between membranes therefore should be re-defined and excluded from the porosity estimation. Such a definition could come from the display of two peaks in the histogram distribution of the pore size. From this case, it can be shown that even if there is only a slight change in the fabrication method, it may require more than one machine to yield a satisfactory understanding of the scaffold porosity. Hence, there is an apparent need for a method that does not rely on physical contacts or cause contaminations, yet is able to draw precise, repeatable information to

predict 3D scaffold porosity. Such a method must reduce potential variance without sacrificing the precision in characterization.

4.1.5 Optical method on porosity measurement based on SHG

Although SHG imaging may seem to be a good method for porosity characterization, quantification of such signals is quite challenging. Firstly, it has a broader spectrum, so does not necessarily fall into the specifically designed optical filter for channelling. Secondly, there is usually little SHG signal from gelatin (Filová *et al.*, 2010). This means that the SHG signals are in general not specific enough for quantification works, and there is a need to distinguish it from the background noise. Thirdly, a typical galvanic scanner would create a hyperstack of 2D images when creating the 3D image. This kind of 3D image has one major obstacle called point spread function (PSF), which happens when the fluorescent signals bleed into the above or below plane that supposedly would be nothing recorded. This creates a strong noise that may obscure signals that would present in proximal regions. PSF for each pixel recorded has to be well contained in order to render the recorded data useful for quantification. Scientists have therefore developed some methods to clear the obscuring noises. One of these methods is called blind deconvolution (Lam & Goodman, 2000), in which a mathematical approximation is used to predict typical PSF profile (noise distribution) in three-dimensional spacing. In this thesis it is expected that blind deconvolution can help remove noises from the planes above and below the focal plane, rendering the SHG signal to specific spots in the 3D environment. Fourth, no matter how well the signals are generated, they are contained in the depth of field (DOF),

which is pre-determined by the objective in use. DOF is typically calculated by the following equation (Murphy, 2002, p.90):

$$d_{tot} = \frac{\lambda_0 n}{NA^2} \tag{4.1}$$

where d_{tot} represents the depth of field, λ_0 is the wavelength of the illuminating light, n is the refractive index of the medium (usually air = 1.005, immersion water = 1.336, and immersion oil = 1.515) (Zhou *et al.*, 2013) used between the coverslip and the objective lens. NA is the objective numerical aperture. It is often helpful to limit the depth of field to avoid confusion on interpretation of the micrograph (Sheppard & Wilson, 1978). Utilized Z-step has to be smaller than half of DOF in order to render the recorded axial data quantifiable. Lastly, although the infrared laser can go deep into the scaffold, it cannot go beyond the working distance of the objective. Therefore, the real depth visualized by MPM would be a combined result of the incidental wavelength and laser power, DOF and working distance of the objective, and the Z-step of choice. When using such an optical method for the assessment of porosity, it is necessary to match the DOF with representative regions inside the scaffold, and then to extend the estimate to other regions of the scaffold on the assumption that the stereology analytic results can represent the whole tissue. This idea is also utilized in the experimental design in this chapter.

4.1.6 Alignment of nanofibers

In order to complete a proof-of-concept AFS, it is also necessary to investigate the alignment quality of the PCL-Gelatin fibers. When the agent releasing samples from

Chapter 3 were created from the rotating drum (RD), it is valid to claim that the samples should release the same amount of agents. For that purpose alone the collection speed at 2000 rpm using RD would seem proper. However, when such AFS is used for culturing cells, the requirement for proper alignment becomes more stringent because there are apparent cell-substrate interactions that may affect cell health or even re-direct the differentiation process. Alignment methods would significantly expand the applications for electrospinning, but a reliable method is particularly difficult to find because the jet of the electrospinning process is a three-dimensional whipping trajectory due to bending instability (Huang *et al.*, 2003). Considering the physical nature of the fiber deposition, re-designing the collector becomes the most efficient approach for the creation of AFSs. Several groups have investigated the proper design of the collector for aligned fibers (Theron *et al.*, 2001, Li *et al.*, 2003b, Teo *et al.*, 2005, Pan *et al.*, 2006, Afifi *et al.*, 2009, Lee *et al.*, 2009, Yan *et al.*, 2009, Badrossamay *et al.*, 2010, Edwards *et al.*, 2010). Although there are many useful designs (Sahay *et al.*, 2011), they tend to fall into two fundamental categories: random deposition between two parallel plates or a forceful rotating mandrel that continuously pulls the fibers. Hereafter these two principle designs are referred to as parallel metal strips (PS) (Chaurey *et al.*, 2010, Li *et al.*, 2003b) and rotating drum (RD) (Ding *et al.*, 2002) as shown in Figure 4.2:

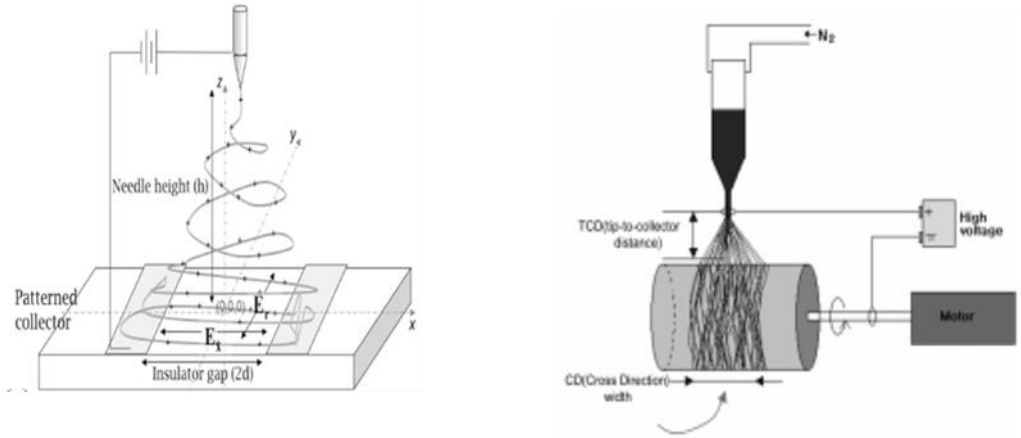

Figure 4.2: Two fundamental designs for the alignment of electrospun fibers. LEFT: Parallel metal strips (PS). *Source: (Chaurey et al., 2010).* RIGHT: Rotating drum (RD). *Source: (Ding et al., 2002).*

The PS fibers align by randomly depositing the thread on the two auxiliary metal strips at different times. As excess fibers build up on the strips, the residual charges may become dominant and repel the proximal fibers. This allows proper creation of the spacing between the fibers. This design can be further controlled with a time-varying switch between the two electrodes (Grasl *et al.*, 2013). Liu and Dzenis (2008) conducted modelling research on the effects of the residual charge and gap size on 4.5 wt% PEO fibers. Their experiments showed that the alignment increased non-linearly with increased gap size, and residual charges could substantially decrease the degree of nanofiber alignment. Later, Chaurey *et al.* (2010) presented a model that analysed the mechanism behind this collection method. In their paper, they claimed that for an insulator gap > 10 mm, the gap fraction with $E_r > E_x$ is almost 100 %, hence suggesting that alignment angle would be minimized (and become parallel). This seemed to be a good starting gap range for testing in this chapter. Nevertheless, effects from the fiber diameter, fiber material, and collecting duration were not addressed. These would need to be controlled in order to draw proper conclusion on the dominant factor in alignment.

The older RD collector receives the fiber randomly across the mandrel with an angular pulling force. This collector has therefore been characterized extensively (Pan *et al.*, 2006). It has also found impact in the growth of neurons (Wang *et al.*, 2009). Depending on the width of the rotor, a variation of this design is the disk collector (Theron *et al.*, 2001, Ghasemi-Mobarakeh *et al.*, 2008). Although faster drawing force (e.g. 6000 rpm) seems to stiffen the overall scaffold, it also tends to reduce the diameter of the PCL fiber due to the faster uptake rate (Thomas *et al.*, 2006). As a result, a moderate rotating speed should be used to avoid unnecessary stretching of the fibers. According to the literature, roughly 4000 rpm, which is 10.47 m/s in terms of the collector surface speed, would be enough to provide fibers with enough alignment (Matthews *et al.*, 2002, Gupta *et al.*, 2009, Kiselev & Rosell-Llompart, 2012). Sundaray *et al.* (2004) illustrated that controlling the interelectrode distance, concentration of the solution, and the use of a single sharp pin as counter electrode can help collect aligned fibers even at 2000 rpm. In short, 4000 rpm may be deemed a reasonable and rather robust median speed for creating aligned fibers without sacrificing the diameter.

Therefore, in this chapter a proof-of-concept AFS that encourages good cell adhesion, yields SHG signals for imaging, and is properly aligned was attempted. It was interesting to see whether the SHG signals could be reliable for quantitative analysis and which alignment method would create AFS with higher fiber quality.

4.2 Materials and methods

4.2.1 Materials

Polycaprolactone (PCL, Mv 70,000 ~ 90,000 Da) pallets and Type A Gelatin from porcine skin were obtained from Sigma. Hexafluoroisopropanol (HFIP) was obtained from Apollo Scientific Limited. Nunc™ Thermanox™ Coverslips that had tissue-culture treated polyester films surface were obtained from Thermo Scientific. Freeze-dried samples were made by isolated collagen from porcine skin acquired from M. Feller Son and Daughter Butchers in the Covered Market, Oxford.

4.2.2 The electrospinning process

For the porosity testing, the polymer solutions used for electrospinning were 10 % w/w PCL:Gelatin = 70:30 in HFIP. The applied voltage for the PCL:Gelatin polymer solution was 9.0 kV. The inner diameter of the spinneret was 0.8 mm. The distance between the Taylor cone and any of the three collecting grounds was 13.5 cm. The flow rate of the solutions was 1 mL/hr. 1 bar of nitrogen gas was also applied during the collection. Fibers were collected on foil papers for 5 minutes. The thin membrane was later washed with ample DI water, dried overnight, and punched into disks with a 15 mm wad punch. 24 disks were then stacked on top of each other, wet with DI water, compressed, and dried again to form a sample that is 1 mm in thickness. The samples were later visualized by MPM and tested by LEP for porosity (n = 3).

For the testing of the two alignment methods, the polymer solutions used for electrospinning were 6 % w/w PCL Only and PCL:Gelatin = 70:30 in HFIP. Aside from the collectors in used, all electrospun fibers were formed with the same condition. The applied voltage for PCL Only fibers was 6.5 kV to 7.0 kV, and that for the PCL-Gelatin fibers was 10 kV to 11.5 kV. The inner diameter of the spinneret was 0.8 mm. The distance between the Taylor cone and any of the three collecting grounds was 13.5 cm.

The flow rate of the solutions was 1 mL/hr. 1 bar of nitrogen gas was also applied during collection.

Three collectors—parallel metal strips (PS), rotating drums (RD) and a flat metal plate for random collection (RM)—were used for comparison (as shown in Figure 4.3):

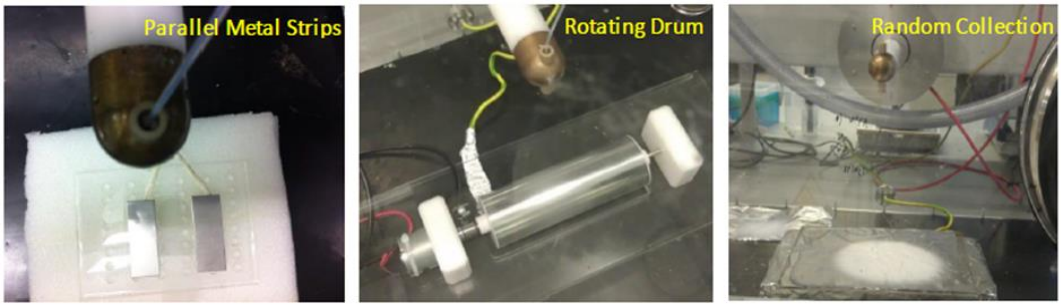

Figure 4.3: Electrospinning collectors used in this thesis.

The PS collector was made of a pair of aluminium metal pieces (2 cm x 5 cm x 0.1 cm each). A polydimethylsiloxane (PDMS) pad (8.5 cm x 12 cm x 0.5 cm) was placed under the two metal strips to provide insulation. The two strips were grounded directly so that the charged fiber could randomly deposit on either surface of the strips. The RD collector was made of stainless steel, with a voltage supply (GW Instek GPS-1850D). The diameter of the rotating drum was 5 cm and the length was 15 cm. All RD fibers were collected at 4000 rpm (approximately 10.47 m/s in terms of the collector surface speed), which was reported in the literature to have sufficient alignment. The grounded surface of the rotating drum was wrapped in aluminium foil paper for fiber deposit. For RM collection, a stainless steel plate (20 cm x 15 cm x 0.1 cm) was used for grounding and a foil sheet was used for fiber collection.

4.2.3 ESEM imaging

For porosity testing, fiber diameter and texture of the 5-minute electrospun membranes and the freeze-dried collagen scaffolds were visualized without coating with an environmental scanning electronic microscope (ESEM, Carl Zeiss Evo LS15 VP-Scanning Electron Microscope, with SE, BSE, VPSE and EPSE detectors). The accelerating voltage was 15 kV at roughly 10 mm working distance and 30 Pa pressure. Fiji (ImageJ, NIH) was used to measure the diameter over 100 electrospun fibers.

For alignment testing, fiber diameter and texture of electrospun samples were visualized with the same conditions. Coating of nanofibers was done using the glow discharge method (Quorum Technologies®); for this an Au/Pt target was used at on operating current of 20 mA and coating times of 105 seconds.

4.2.4 Fiber characterizations

In order to optimize the collection process for PS fibers, Nunc coverslips were placed right between the two metal strips for the newly formed fiber to deposit. Two parameters were measured for the assessment of alignment given by PS—the spacing between the fibers and the degree of alignment. The measurements were performed for PCL-Gelatin fibers only because viability study results prefer the use of such material on cell culture. The spacing is obtained by directly measuring the distance between the surface of two proximal fibers (n = 30). Spacing investigation was taken for different collecting durations (e.g. 10, 30, 60, 300, 600, and 1200 seconds). Later, the degree of alignment was measured by comparing the angle of the fiber versus the axis of the image (θ) with respect to various distance of separation between strips (i.e. 1.5, 2.5, 3.5, and 5.5 cm) (n = 30) for a duration of 20 minutes. Same angle measurement was applied

to the RD group. All samples were repeated 3 times. 2D images in this section were obtained using a Nikon TiE2000 inverted microscope equipped with NIS Elements.

Young's modulus of samples from the three collection methods was evaluated using a Bose-electroforce Compact Test Frame. A 20N load cell was used for measuring the force. The electrospun samples were first collected for 20 minutes, then cut into 6 cm x 3 cm sheets at dense regions. These sheets were later carefully folded in half along the long side three times, making the thickness of the central portion approximately eight times that of the original sheet thickness. The exact thickness for each sample was measured using a micrometer (Keyence LS-7601, U.K.), so the cross-sectional area could be calculated accordingly. Mounted samples had initial separation of 5 mm between the two clamps. Data for applied force and travel were collected and converted into stress and strain. Young's modulus values were derived from the trend line and at least 5 samples were tested for each scenario.

4.2.5 Porcine collagen isolation

The freeze-dried collagen scaffolds were prepared by Ms Emily-Jane Randall, University of Oxford. 100 g of porcine skin was soaked in acetone in the reactor for 24 hours in a fume hood. A solid:solvent ratio of 1:15 [(wet weight skin (g):solution volume (mL)] was used. The skin was then thoroughly washed with deionized (DI) water. Lactic acid (0.5M/2.5M) was added (1:15 solid:solvent ratio) and the tissue was left for 24 hours. Additional 6.5 liters of DI water was added before the reaction stage. This was carried out at residence times of 24h and 48h, and at pepsin levels of 2 g and 10 g. The solid:solvent ratio was 1:80 (initial tissue weight:total reactor solvent volume). Later, pH was adjusted to 2 with 10M HCL for pepsin t function. For residence time

24h the mixture was agitated for 8h, and for 48h the mixture was agitated for 16h. 4 liters of solution was tapped off and adjusted to pH 7 using 8M NaOH. The precipitant was left for about half an hour and then centrifuged in a Beckman Coulter Avanti Series centrifuge (Brea, CA, United States) at 5000 rpm for 25 minutes at 4°C using a JLA8.1 rotor. The supernatant was discarded and the pellets were scraped into a beaker for lyophilisation.

4.2.6 Preparation of the freeze-dried samples

Following the dipping sequence the sample was carefully removed from the holder using tweezers and placed into the wells of the custom mould; DI water was then added to each well until the scaffolds were immersed and the whole mould frozen at -20˚C for at least 24 hours. Once sufficient samples had been collected the moulds were taken to be freeze-dried in a VirTis Advantage Plus EL -85 Freeze Dryer (SP Scientific, SP Industries, United States), provided by the Biomedical Ultrasonics, Biotherapy, and Biopharmaceuticals Laboratory in Oxford University. The detail of the lyophilization process is summarized in

Table 4.1.

Steps	Onset (˚C)	Endset (˚C)	Hold (min)	Ramp (˚C/min)	Phase Time (min)	Total Time (min)	Vac (mtarr)
1	20	-20	-	5	8	8	-
2	-20	-20	15	-	15	23	-
3	-20	-50	-	1	30	53	-
4	-50	-50	210	-	210	263	-
5	-50	-20	-	0.5	60	323	145
6	-20	-20	2880	-	2880	3203	145
7	-20	25	-	0.25	180	3383	100
8	25	25	2100	-	2100	5483	-

Table 4.1: Lyophilization cycle.

4.2.7 ATR-FTIR for protein integrity

A Bruker Tensor 37 Fourier transform infrared spectroscopy (FTIR) Instrument coupled with Hyperion 3000 FPA (focal plane array) system was used to study the integrity of gelatin and collagen before and after fabrication. The MIRacle ATR (Attenuated Total Reflectance) with germanium (Ge) crystal was used to acquire the ATR spectrums, which show peaks that were inverted in absorbance mode with acorrected intensity. Resolution was set as 8 cm^{-1}, and the aperture in use was 6 mm. KBr was used as the beamsplitter material. The scan rate was 20 kHz, and 64 scans were conducted. Three samples were examined: porcine gelatin powder, freeze-dried porcine skin collagen, and embedded gelatin inside the PCL electrospun fibers.

4.2.8 Multiphoton microscopy (MPM)

Three-dimensional fluorescent images were obtained from a modified BioRad Radiance 2100 MP Multiphoton Microscope (Zeiss; Jena, Germany). Near infrared (NIR) laser beams (wavelength = 800 nm) were obtained from a tunable 76 MHz femtosecond pulsed Ti:sapphire laser (Mira 900-F, Coherent, Ely, U.K.) pumped by a 10 W multiline argon ion laser (Verdi; Coherent). For better matching of the two-lobe profile as mentioned in Section 2.13, a Nikon S Fluor 10X water-immersion objective with a considerably small NA of 0.30 and working distance of 2 mm was used for all images. The emission filters selected were: 495 nm for blue, 525 nm for green, and 595 nm for red. For each scaffold, 9 fields of view (785 µm x 785 µm each, in commonly used 512 x 512 pixels (Ralston *et al.*, 2008, Labouta *et al.*, 2011, Bakalar *et al.*, 2012,

Ferro *et al.*, 2012) were scanned at 500 lines-per-second (lps) for the investigation of porosity using this optical method. The recorded Z-step was 2.65 μm.

4.2.9 Image Processing

A specially designed working station was used for all of the image processing works. This hot desk computer utilized an Intel® Xeon® CPU E3-1270 V2 @ 3.50 GHz CPU. The operating system was 64-bit Windows 7 Enterprise. The installed memory was 16.0 GB, and the graphic card in use was NVIDIA Quadro 2000.

Image files first underwent 3D blind deconvolution treatment using AutoQuant X3. They were later reopened and constructed by Imaris 7.6.1. Regions of Interest (ROIs) were set for 3D volumes that were fully occupied by the signals from scaffolds. Regions that may be affected by laser damage were intentionally avoided to increase precision of volumetric calculations. The isosurface objects were thus constructed to quantify the volume and to illustrate the morphology both on the outer surface and the interior of the scaffold. The porosity that is measured by the microscopic method (P_{MPM}) was calculated by the equation:

$$P_{MPM} = \frac{V_{ROI} - \sum V_{ISO}}{V_{ROI}} \tag{4.2}$$

where V_{ROI} is the total volume occupied by the ROI of choice, and $\sum V_{ISO}$ represents the sum of the volumes of all the isosurfaces constructed.

For the electrospun scaffolds, all the isosurfaces were created at the manual threshold of 0 (between 0 and 255 in terms of the grey scale). The surface area detail level was set at 1 μm. Background subtraction of diameter of the largest sphere (set at

11.1 μm) which would fit into the surface objects was also performed. For freeze-dried samples, all isosurfaces had a manual threshold of 19, surface area detail level of 2.96 μm. The objects were constructed on absolute intensity only (no background subtraction). Thresholds were selected and hold constant at the moment when developed isosurfaces fully occupied the SHG signals in blue channel.

For each electrospun and freeze-dried sample, nine images were taken and processed with the isosurface protocol using the same threshold. Estimated optical porosity values from the nine spots were then averaged to provide one single value for the whole sample. For all three samples from the same group, the three averaged values were then used to calculate the final P_{MPM} of either the electrospun or the freeze-dried group.

4.2.10 Liquid extrusion porosimetry (LEP)

The same samples that were visualized by MPM were sent to Porous Materials, Inc. (Ithaca, New York, United States) for liquid extrusion porosimetry analysis (LEP, service T901), which yielded standard information regarding pore throat diameter distribution and porosity of the scaffolds. These values would serve as the control for the testing of the MPM estimates of porosity. The Galwick solution was used as the testing liquid which has a surface tension of 15.9 dynes/cm and is able to detect a pore diameter of 0.07 mm at 100 psi. The total percentage porosity (P_{LEP}) was calculated by Equation 4.3:

$$P_{LEP} = \frac{M_{abs} - M_{ext}}{M_{abs}} \tag{4.3}$$

where M_{abs} is the mass when the sample fully absorbed Galwick and M_{ext} is the total mass of the Galwick solution that was expelled from the sample by the LEP machine. Solution volumes contained by larger pores were first expelled as the pressure increased, followed by the ones in smaller pores until no more solution was collected.

4.2.11 Statistics

Spacing between fibers was reported in mean ± sample standard deviation (SD) (n = 30). Fiber diameters were reported in mean ± population standard deviation (n = 100). Porosity (n = 3) and Young's Moduli (n ≥ 5) measurements were reported in mean ± standard error of the mean (SE). Statistical analysis was carried out with either Student's *t* test or one-way Analysis of Variance (ANOVA) with multiple comparisons against the control group in GraphPad Prism 6 (version 6.03). $p < 0.05$ was considered to be statistically significant.

4.3 Results

4.3.1 Surface characterization of the scaffolds

In order to evaluate the precision of the optical estimate of porosity using SHG signals from collagen/gelatin, two types of scaffolds were created. ESEM images of the two scaffolds are shown in Figure 4.4. Although the spinning process was quite steady, the 10 % PCL-Gelatin fibers seemed to show a high variance over fiber diameters. There was no bead-formation, and the fibers seem to be flattened, showing smooth surfaces. The fibers were measured to be 18.069 ± 9.077 μm. This type of fiber would present a challenge for the optical assessment of the porosity, as it is likely that signals from the

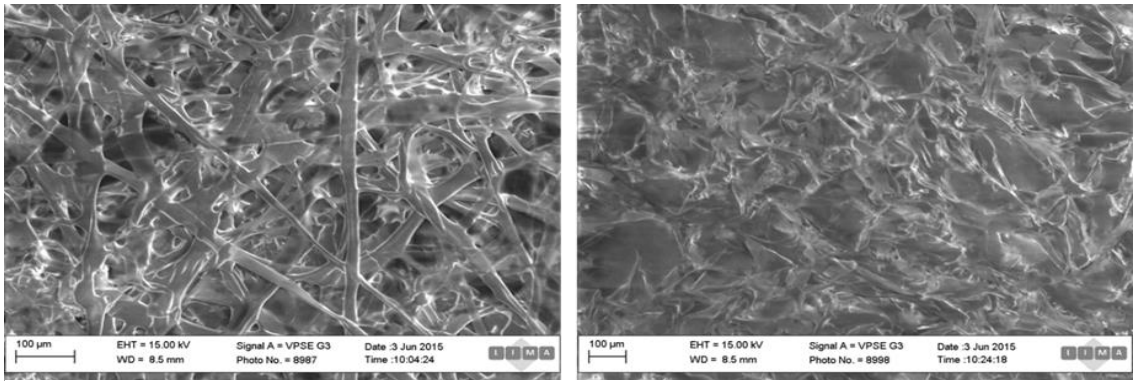

Figure 4.4: Electrospun and freeze-dried scaffolds as visualized by ESEM. LEFT: The electrospun samples show a high variance in fiber diameter. RIGHT: freeze-dried scaffolds show difficulty in depth-interpretation. Scale bar = 100 µm.

smaller fibers might not be picked up in the MPM session. The freeze-dried scaffold showed lots of folding and wrapping globally. Graphical assessment of the pore diameter/volume using ESEM images seemed unlikely to provide a good evaluation, since ESEM is still a surface-scanning method for creating reliable 2D nano-scale images. Overall, both of these scaffolds would pose tremendous challenges in porosity assessment.

4.3.2 Protein structure assessment

Zeugolis *et al.* (2008) reported that HFIP might degrade and destroy the α-helical structure of gelatin. Other experimental or ambient factors might also alter the conformation of gelatin (Kim *et al.*, 2000). Therefore, it is essential to evaluate the chemical bonding from FTIR spectra to see if the gelatin remains genuine after fabrication. The ATR-IR spectrum of gelatin is mainly characterized by the presence of two important characteristic regions—the amide I and the amide II bands (Van Vlierberghe *et al.*, 2008a, Van Vlierberghe *et al.*, 2011). The amide I band at 1664 cm^{-1} contains primarily C=O stretching of the peptide group and is extremely sensitive to changes in the gelatin chain conformation (Prystupa & Donald, 1996). The amide II

band at 1556 cm^{-1} is rich with N-H bend coupled with C-N stretch (Jackson *et al.*, 1995). These two signature peaks can help us characterize the condition of the embedded gelatin.

Figure 4.5 shows that for the three groups to be compared, the signature peaks for collagen did not shift away for the commercial gelatin powder and the embedded gelatin inside the electrospun fibers. Compared to the freeze-dried collagen scaffold, both gelatin powder and the gelatin embedded in the electrospun fibers still showed the α-helical specific peaks at 1650 cm^{-1} for the amide I region and 1563 cm^{-1} for the amide II region (Dong *et al.*, 2009). These slight differences are probably negligible. In terms of the area under the two peaks, gelatin fiber is apparently smaller than the freeze-dried collagen samples. This has two meanings: firstly, it showed that gelatin, while dissolved in HFIP and fabricated using electrospinning, can maintain its function inherited from the collagenous-state. This is particularly important if the PCL-Gelatin fiber is to be considered as a material for cell culture in the future. Secondly, it was to be expected that the SHG signals from the nano-fibrillar samples would be weak and blurry. The area under the absorption spectra represents that amount of such chemical structure that can be found using the ATR stage. Since electrospun fibers are already quite small to be detected by MPM (at best 100 nm only), it is essential to keep the SHG signal above a certain degree to be detected reliably. Therefore, for the scheme of using the SHG from gelatin to study porosity of the scaffold, this would pose an extra challenge in controlling the signal-to-noise ratio.

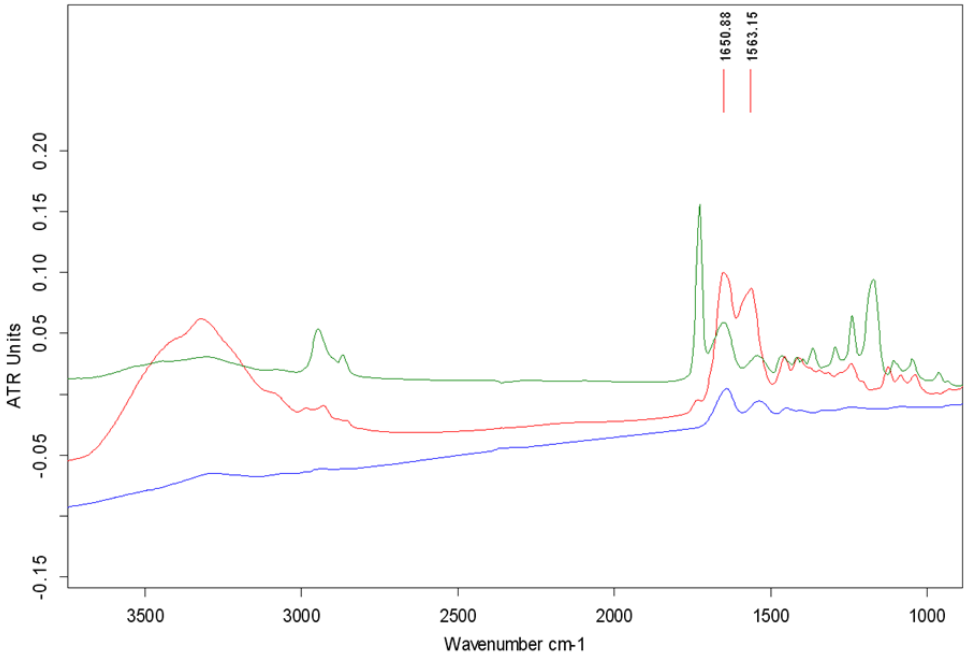

Figure 4.5: ATR-FTIR Absorbance spectra. Red: freeze-dried collagen; Blue: gelatin powder as acquired from the vendor; Green: embedded gelatin in the electrospun fibers. The signature peaks that represent collagen were picked for comparisons.

4.3.3 Improvement of signal-to-noise ratio from deconvolution

Figure 4.6 shows the 3D MPM section of the electrospun fibers. Due to the reduced SHG signals from the embedded gelatin, the recording had to be done with a high gain on all three channels in order to capture the fiber morphology. This caused difficulty in distinguishing between the SHG signals and the background noise. Also, signals by the PSF can cause blurriness in the Z-axis, which obscured wanted signals from the fiber. If two voxels are closer than the full width at half-maximum (FWHM) of the PSF, they are obscured by the blurriness (Huang *et al.*, 2009). This also contributed directly to the loss of resolution and the sequential capability toward volume rendering of the isosurface processing. For this reason, it is desirable to rely on theoretical and automated methods to enhance the contrast for the fiber. Stronger SHG signals from

gelatin were mostly recorded in the blue channel, whereas they also appeared weakly in the green channel due to photobleeding and likely died out in the red channel. For this reason, it is reasonable to consider the red colour to be mostly signals from the noise. If the red signal occurs in a particular voxel, it should be removed. The green strips in the XZ-frame in the Before Deconvolution panel (i.e. red arrows in Figure 4.6) indicated signal saturation by the green signals at these voxels. These are artefacts from high gain during recording and should be removed as well. The left (before deconvolution) picture show a tremendous amount of noise (as presented by the cloudy green and red dots). Even the blue gelatin signals from the XZ- or YZ-sides are blurry smears. Such images would be difficult to be analyzed by isosurfaces. In order to enhance the SNR, a blind deconvolution software was tested to remove these noise sources. On the right is the

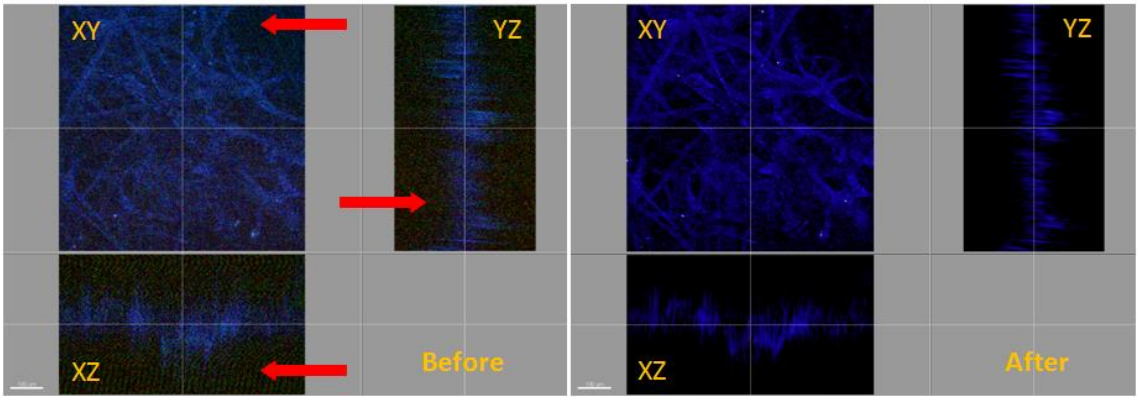

Figure 4.6: MPM imaging of electrospun fibers. LEFT: original image. RIGHT: same image after blind deconvolution. The image recorded SHG signals from the embedded gelatin, which can be observed from three angles (XY, XZ, and YZ sides). The two images were presented in the same way, meaning, look-up table setting, contrast, brightness, and gamma gain are the exactly same for better comparison. Red arrows indicate the present of cloudy green and red signals, which mostly came from the background noise. They were removed after blind deconvolution in an automated process. This led to a better estimate of the void space (i.e. black areas in the after deconvolution panel). Scale bar = 100 µm.

same image file after being blindly deconvolved. Most of the cloudy noises were removed, and even the blue signals start to separate from each other, making the signal from single fibers stand out. This indicates that when visualizing fibrillar scaffolds, deconvolution is necessary in order to reduce the blurriness in the Z-axis caused by the point spread function of the SHG sources on the fibers. This treatment enables the construction of the fibrillary network.

Figure 4.7 shows a similar comparison for the freeze-dried collagen scaffolds. These scaffolds had better SHG signals from the collagen fibers than expected, since the FTIR result in Figure 4.5 showed a larger total area under the signature peaks. Although the SNR seemed to be well controlled for the original image (almost no signal from the green and the red channels), the PSF that was presented gave excess signals that may still cause an overestimate of the scaffold volume (thus an underestimate of the porosity of the scaffold). Deconvolution still caused the signal to be much reduced to the plane only, and the fibrillar structure of the collagen became easier to estimate. Deconvolution

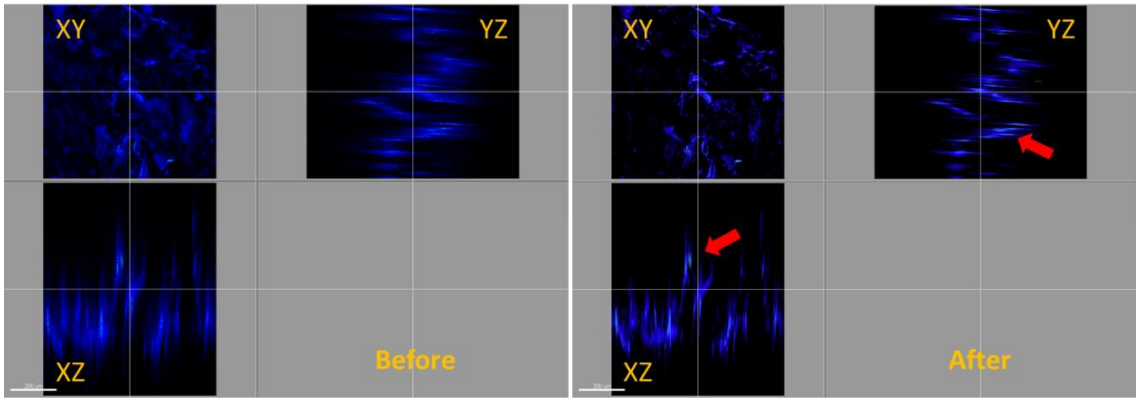

Figure 4.7: MPM imaging of freeze-dried samples. LEFT: original image. RIGHT: same image after blind deconvolution. The two images were presented in the same conditions. Stronger contrast on these green spots (indicated by red arrows) were revealed in the deconvolved picture, indicating the spots where local collagen could be denser. The smear from the blue collagen signal has also been improved to provide better signal for later isosurface reconstruction. Scale bar = 200 μm.

here also revealed regions that had denser collagen fibers, as shown by the green spots (in the After Deconvolution panel in Figure 4.7). These spot were previously obscured by the PSF from other portions of the scaffold, and could be a limiting parameter for the analysis of mass transport. This indicates that deconvolution is not only important for the enhancement of the SNR, but also for revealing structural information that was previously obscured from the original MPM images.

4.3.4 Estimate of the porosity of the scaffolds

Representative histograms of the pore diameter distribution of the two groups are displayed in Figure 4.8. Average pore diameter was calculated to be 57.4521 μm for the electrospun samples and 78.3687 μm for the freeze-dried samples. From the figure, it was observed that there were a small number of extremely large pores presented in the electrospun membranes. These might come from the passage of the liquid stored between two electrospun membranes, since LEP mainly measures the throat pore diameter of the sample as it reacts to the increasing pressure. Such large pores were not found in the freeze-dried samples, suggesting that the freeze-dried samples and are more coherent and homogeneous, more likely to follow a normal distribution.

Porosity values calculated by the optical method (P_{MPM}) and the mechanical method (P_{LEP}) were summarized in Table 4.2. Isosurface processes of both groups from the tilted XZ-side were displayed in Figure 4.9. The blue SHG signals from the scaffolds were adequately enclosed by the green, 80 % transparent isosurface. This approximation using isosurface is most difficult when signal boundaries were determined from the XZ-side because the voxels were not isotropic and are in general longer in the Z-axis. Such a complete coverage would be able to turn the 3D MPM

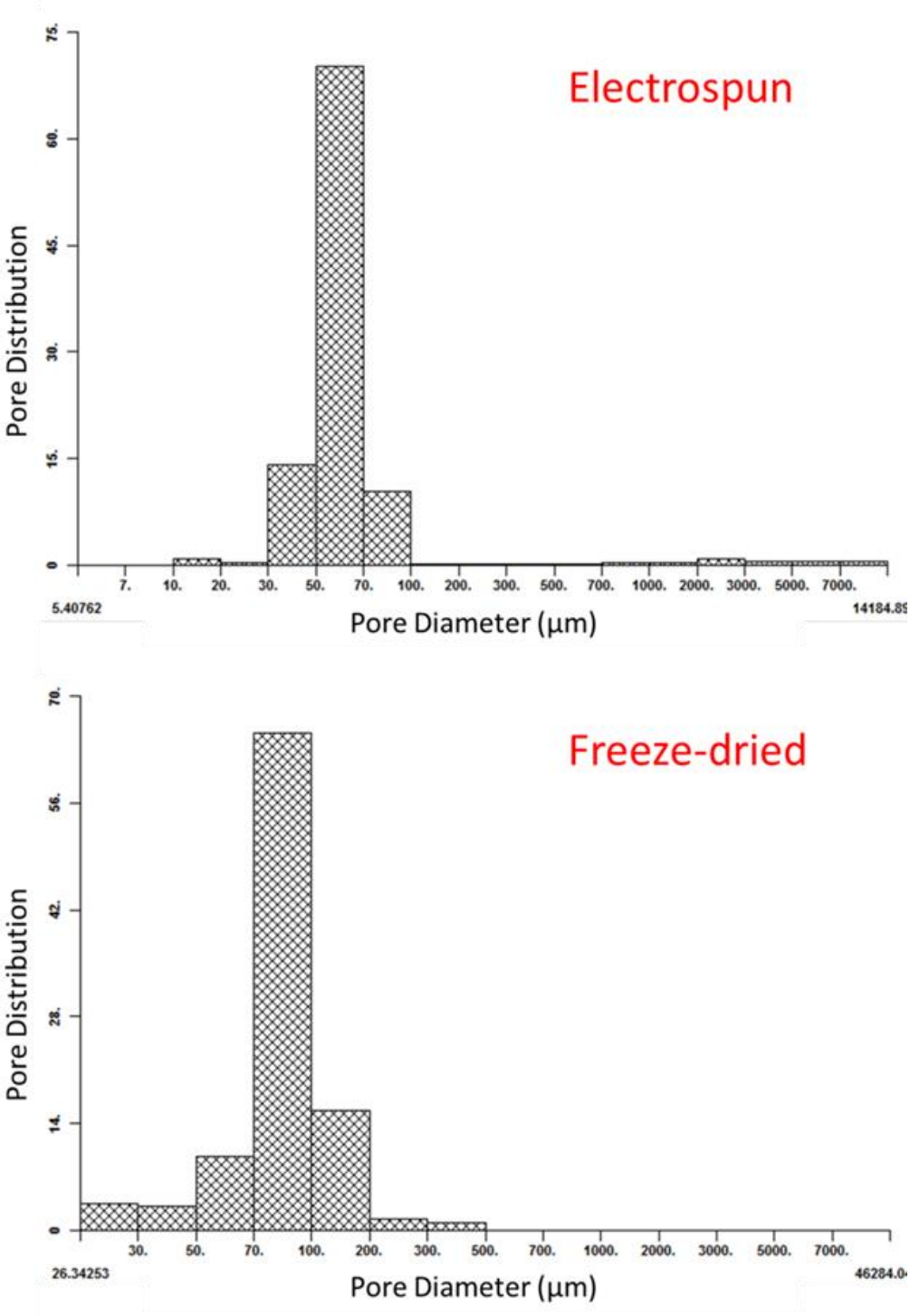

Figure 4.8: Pore diameter distribution of the electrospun and freeze-dried samples. Data were acquired from the liquid extrusion porosimetry (LEP) (3 samples in total) to serve as a control for the multiphoton void space analysis. Presence of extremely large pores was found peaked between 2000 to 3000 µm for the electrospun group but not for the freeze-dried group, which shows a uniformed pore distribution. This indicated that the LEP method is capable of providing a distinction between the two types of pores in 3D electrospun scaffolds.

Porosity (%)	Average ± SE
Electrospun Membrane	
P_{MPM}	47.64 ± 0.44
P_{LEP}	20.84 ± 0.74
Freeze-dried Scaffold	
P_{MPM}	66.45 ± 1.14
P_{LEP}	66.95 ± 0.28

Table 4.2: Estimated percentages of porosity. For the freeze-dried scaffold, the P_{MPM} value has a high agreement with the control P_{LEP} value. However, for the electrospun membrane, P_{LEP} shows a much lower through pore estimate than the P_{MPM} due to the exclusion of the pocket space between membranes.

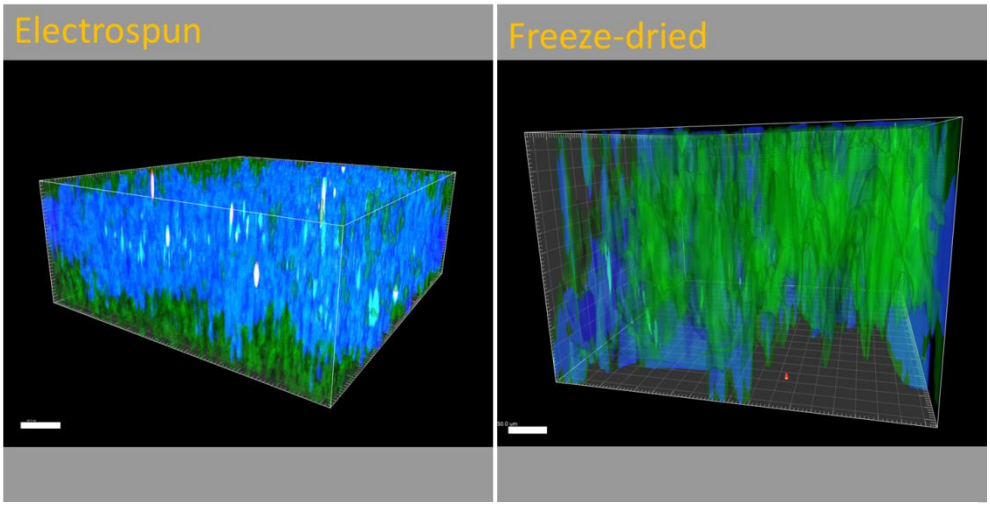

Figure 4.9: Isosurface processing observed from the XZ-side. Blue—SHG signals from the scaffold. Green—isosurface approximation of the volume occupied by the SHG signals. Signals from the scaffolds were completely enclosed by the isosurface in order to present a better estimate of the void space. Scale bar = 50µm.

images into quantifiable data. For the electrospun group, P_{MPM} showed a significant ~27 % difference from P_{LEP} ($p < 0.0001$ in unpaired *t* test). On the other hand, the *t* test showed no significant difference between P_{MPM} and P_{LEP} for the freeze-dried group. Largest error occurred in LEP measurement of the electrospun group (3.6 %), but was within the expected 5 % error as designed for the machine. Overall, the estimated

porosity values from the two methods seemed to agree on the freeze-dried samples but not on the electrospun samples. Nevertheless, both the optical and liquid extrusion methods showed repeatable measurements, since the errors were all below 5 % of the mean values.

4.3.5 Fiber characterizations

Fiber characterization focused on the 6 % w/w PCL-Gelatin fiber. Figure 4.10 presents the observation on interfibrillar gaps by PS, and the numerical data is summarized in Table 4.3. As the collection period increased, the spacing between two

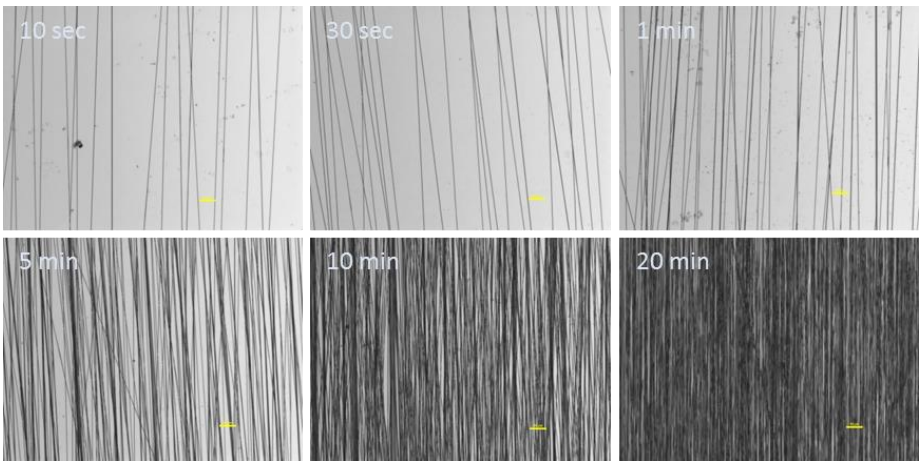

Figure 4.10: Bright field microscopy of PCL/Gelatin PS fibers. Samples were collected in different durations: 10 s, 30 s, 1 min, 5 min, 10 min, and 20min. Scale bar = 50 µm.

proximal fibers became smaller and smaller. By the time it reached 20 minutes, the spacing between any two fibers became indistinguishable and more crossovers were observed. As a result, the 20-minute period was determined to be the time when the fibers form a single layer that may prevent cells falling out (assuming free cells have a diameter of 10 µm), and it was used in designing the immunohistochemistry experiment.

Figure 4.11 presents a correlation that presents how that variance decreases over duration of collection.

Spacing (µm)	Min	Max	Mean	SD
10 sec	9.3	157.0	50.7	35.8
30 sec	13.2	147.9	54.4	34.9
1 min	5.6	73.7	25.5	15.0
5 min	4.1	37.1	15.3	6.5
10 min	0.6	8.9	2.8	1.6
20 min	N/A	N/A	N/A	N/A

Table 4.3: Statistical analysis on spacing.
20 min samples showed non-distinguishable spacing. n = 30 for each measurement.

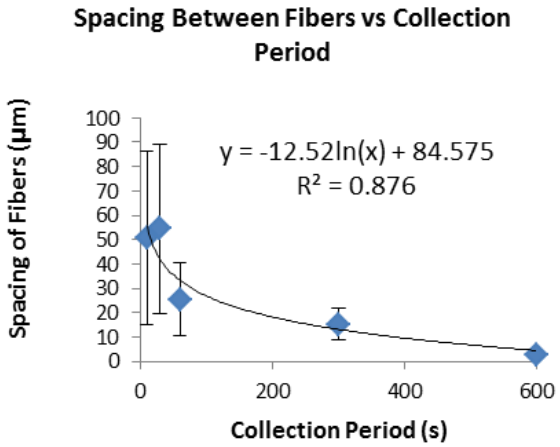

Figure 4.11: Spacing observed between fibers (n = 30).

Data for the degree of alignment of PS is summarized in Table 4.4. The average degree of alignment did not change much in all groups, and the fibers collected were quite perpendicular to the edge of the slide. Student's *t* test indicated that compared to the other average numbers, fibers collected by parallel strips with a 2.5 cm separation

seemed to be most consistent, showing controlled variance. As a result, this separation was utilized for all the cell experiments with PS scaffolds.

Degree of alignment (°)	Mean	SD
PS - 1.5 cm	93.0	11.24
PS - 2.5 cm	92.0	3.3
PS - 3.5 cm	94.0	8.6
PS - 5.5 cm	92.9	7.3
RD	75.0	14.9

Table 4.4: Statistical Data analysis on degree of alignment at different insulator gaps. n = 30.

Fiber diameter measurements are summarized in Table 4.5. Larger insulator gap in PS reduced the fiber diameter. But all data indicated that the fiber diameter was roughly controlled at 1 μm, which would be ideal for cell culture. Student's *t* test showed that $p > 0.05$, indicating that the six conditions selected for this experiment did not generate significant differences in fiber diameter. Therefore, potential effects generated by fiber dimension alone could be neglected.

Diameter (μm)	Min	Max	Mean	SD
1.5 cm	0.781	1.645	1.180	0.261
2.5 cm	0.519	1.505	0.962	0.172
3.5 cm	0.564	1.498	0.950	0.181
5.5 cm	0.556	1.478	0.868	0.179
Rotating Drum	0.567	1.080	0.821	0.127
Random	0.974	1.735	1.201	0.197

Table 4.5: Statistics on diameters of nanofibers. Samples were prepared by metal strips method with different separation, rotating drum at 4000 rpm and random collection (n = 100 for each group).

Figure 4.12 shows the ESEM images of the fibers from the three groups. The PS groups seemed to have mostly straight and individual fibers. Although few beads were found, they did not seem to be significant to affect cell culture. The RD groups showed proper orientation of the fibers, but slightly more secondary bendings were observed from the sample. Cross-over sections were occasionally found. The RM fibers, on the other hand, did not show clear fiber orientation. As a result, the three samples could be interpreted as a transition of degree of cross-over, with PS possessing the least and RM the most cross-over.

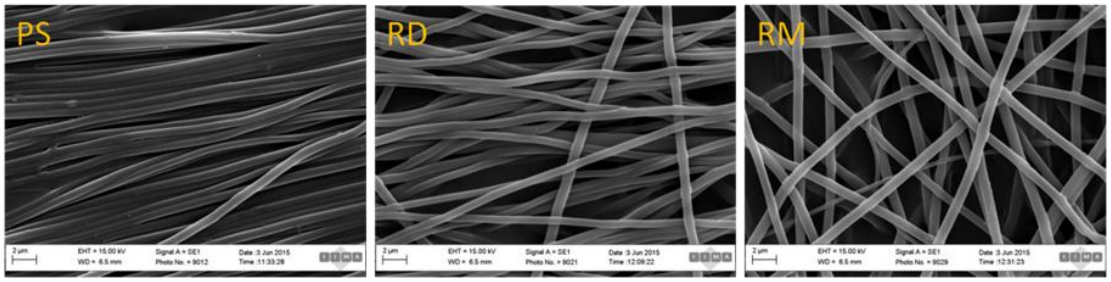

Figure 4.12: ESEM images of PCL/Gelatin nanofibers from different collectors. All images taken at 10kX magnification. Scale bar = 2 μm.

Young's moduli (*E*) of the three groups were derived from the slopes of the trend line of the stress-strain relationship. Representative curves (with *E* values closest to the average of each group) were selected to demonstrate the results of the uniaxial tensile stress tests in Figure 4.13. Statistical values are summarized in Table 4.6. The quality of the curves indicated that the method used to test bundles of nanofibers was reliable. Comparison of the *E* values showed that both alignment methods PS and RD had elevated Young's moduli and were therefore stiffer than the normally collected RM mesh. This is likely due to the fact that the bundled fibers were measured for the macromechanical performance, but significantly fewer fibers were polarized in the RM sample. PS fibers seemed to be slightly stiffer than RD fibers, but showed no significant

difference. The data here serves as a reference for the interpretation of the neurite extension study.

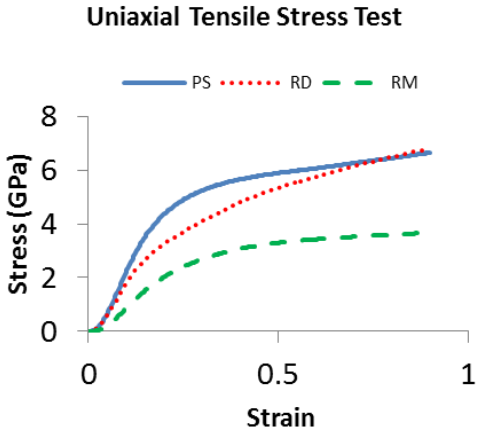

Figure 4.13: Representative stress-strain relationships of the three groups (from at least 5 measurements).

E [GPa]	PS	RD	RM
AVE	24.181	22.022	11.104
SE	4.331	2.450	0.752

Table 4.6: Summary of measured Young's moduli for the three groups (from at least 5 measurements).

4.4 Discussion

4.4.1 Limitation of scanning electron microscope for porosity assessment

Several papers utilized SEM or ESEM as their primary method for the assessment of scaffold porosity. However, in this report it was shown that such assessment can become invalid when (1) the scaffold has a dense fibrous network, and (2) the scaffold is readily three-dimensional. Although ESEM can visualize the scaffolds at nano-scale and can be used to measure porosity (Kellomäki *et al.*, 2000, Walsh *et al.*, 2001, Heydarkhan-Hagvall *et al.*, 2008), it operates basically on the scattering of electrons and is therefore a 2D-based characterization method. When the network becomes denser, it is sometimes difficult to define the pores. On the other hand,

when the scaffold has substantial depth to be seen as a three-dimensional scaffold, ESEM lacks the capacity to look beyond the area that was covered by other fibers, making the porosity assessment impossible. This shows that for proper microscopic assessment of porosity, a method with transmitting signals is essential. Although ESEM can give nano-scale details, it is clearly limited for 3D applications.

4.4.2 Deconvolution as a necessary step for quantification of signals

For fibrillar scaffolds, the fiber size can potentially become a limitation to the quality of the scaffold. According to the literature, MPM can visualize 100 nm fibers if assuming an isotropic PSF and the SNR is well controlled. Super resolution fluorescent microscopy can achieve an optical resolution as high as ~20 nm in the lateral direction and 40–50 nm in axial dimension (Huang *et al.*, 2009). Although by its default design MPM could not reach this resolution, it could still be useful in the analysis of most fibrillar scaffolds, given that individual fibers would be larger than 100 nm in most cases. The caveat, however, is that the SNR has to be precisely enhanced. SHG signal has the natural issue of two-lobe profile, which would likely generate a distorted fluorescent PSF in the Z-planes. Helmchen and Denk (2005) discussed briefly in their paper about calculating the PSF profile. The conical shape of the signal occupies obscure information in the space limited by the depth of the field, which means that it would create a type I error (false positive) when conducting the volumetric assessment. This would eventually lead to an underestimate of the porous volume. Unless the optical components are specifically designed, and the galvanic scanning can be conducted on a motorized stage with precise control that matches the XY resolution, deconvolution becomes the most economical method to reduce the effects from PSF. Blind

deconvolution is an automated process that eliminates the PSF according to a mathematical approximation of the conical profile. This is a well-established method to enhance the SNR in 3D (Ayers & Dainty, 1988, Holmes, 1992, Shaw, 2006, Levin *et al.*, 2009). The results here showed that such a method could eliminate systematic noise in the 3D space and successfully enhance the weak gelatin SHG signals. It is, therefore, an essential step toward proper quantification of the fluorescent signals. Deconvolution also removed the conical signals that obscured the stronger signal from denser collagen population in the freeze-dried scaffolds. Such observation would be important when evaluating the scaffolds function in cell culture. Therefore, it is highly recommended to perform blind deconvolution on all MPM images.

4.4.3 Voxel design, resolution, signal acquisition, and sampling rate

Adjustment for the best resolved image is a tricky matter. A strong resolving power that can lead to useful quantification data requires a good combination of objective magnification, numerical aperture, XY-pixel setting, Z-step, and scanning speed. 10X objective gives a better global view of the scaffold, and is more likely to contribute to easier and unbiased quantification of void space. Although it is desirable to have the 2D frames in finer 1024 x 1024 pixels, 512 x 512 setting allows a longer pixel-dwelling time for 500 lps scanning speed. This is important when the signals from the fibers are weak and hard to separate from the noise and when a low magnification objective (e.g. 10X) is in use. It is worth noting that if the pixel dwelling time is too long, however, it is easier to cause signal saturation or a rise of local temperature, even leading to a burning event. This will cause direct damage to the scaffold and should be avoided. For the radial resolution, 512 x 512 over a 785 x 785 μm^2 area means that each

pixel would represent roughly 1.5 x 1.5 μm^2. This allows the computer to adequately capture all of the optical data from the microscope in a proper sampling manner. Considering the requirement for Nyquist sampling, if two proximal pixels are required for sampling the volume of one fiber, the XY-pixel of choice could sample approximately 95 % of the fibers with larger diameters (evaluated using standard score, or z-score with backward conversion to percentile).

In terms of the axial resolution, sampling is limited to three factors: signal intensity at each plane, DOF, and Z-step. Signal intensity is influenced by laser power and penetration depth. Assuming there is enough signal, the DOF would be overrun by the PSF. In proper sampling, DOF would also need to be greater than two times of Z-steps. In this case, PSF has been fixed by deconvolution, so the recorded signals would come from the plane only. The recorded Z step was 2.65 µm, which is much smaller than the calculated DOF from Equation 4.1 (11.87 µm) and the majority of the fiber diameters. The percentage of the fibers that could be sampled would be approximately 92 %. This resolution would lead to an underestimate of the total volume taken by the electrospun fibers (thus an overestimate of the porosity), but should be representative for the larger freeze-dried samples. As a result, the overall setting for the resolution of the 3D scaffold should be capable for quantification of the void volume inside the samples.

4.4.4 Thickness of fibrillar scaffolds

In Figure 4.6 and Figure 4.7, the deeper focal planes seem to show reduced signal intensity due to absorption and scattering. The maximum achievable imaging depth is proportional to the scattering mean-free-path and depends logarithmically on

available laser power, two-photon advantage and collection efficiency, as mentioned by Oheim, *et al.* (2001). On the other hand, the freeze-dried samples showed a more illuminated thickness (~400 μm) than the electrospun samples (~200 μm) probably because the electrospun fibers contain less gelatin/collagen to start with. It is also reflected by the ATR-FTIR result that, for electrospun samples, the integrated area under the two signature peaks is apparently smaller than that of the freeze-dried samples. Also, according to Andresen *et al.* (2009), SHG signals could diminish as the laser goes deeper into the tissue. For an excitation wavelength of 880 nm, 50 % of the emission would diminish at roughly 30 μm into the tissue, while 100 % diminished at roughly 200 μm. Spatial resolution would also decrease while increasing imaging depth. In visualization of lymph nodes, a penetration depth of 50 um could already lower the spatial resolution by 2 to 5 fold compared to that at the surface (Niesner *et al.*, 2007). It is worth mentioning that typical imaging depths with MPM are limited to less than 300 μm in many tissues due to light scattering, but with proper fixation and clearing, it is possible to achieve a penetration depth and fields of view in excess of 2 mm with mouse organs (Parra *et al.*, 2010). As a result, deep tissue imaging requires a specially designed imaging system, which is not available for this MPM equipment.

4.4.5 A comparison between the two porosity assessments

It is not the purpose of this report to develop MPM as a replacement for physical measurements for porosity. P_{MPM} and P_{LEP} were measured on very different scientific grounds—one simply derived the void space from surface SHG signalling whereas the other takes into account the flow pattern and bulky material interaction with the fluid. The methods can only replace each other when doing so does not cause problems in

interpretation (Bland & Altman, 1986). In this case the two methods may lead to two different interpretations, which are useful in their own areas of study. Nevertheless, on the assumption that scaffold swelling would not occur, a direct comparison between the two methods revealed important considerations that should be included when performing characterization. On the theoretical bases, as long as the used fluid in LEP is not absorbed into the scaffold to cause significant swelling, the MPM estimate of porosity should come close to the measurement by LEP. If such absorption does not occur to the scaffold material, then the lack of data agreement should be investigated with respect to the size of the fibers, optical signal intensity, and the fabrication process of the 3D scaffold.

For the freeze-dried scaffolds, P_{MPM} and P_{LEP} are almost equal to each other (~67 %). This demonstrated the usefulness of MPM as an alternative, non-destructive, and quantitative assessment of scaffold porosity. The bulk of the scaffold was an integrated piece of collagen; therefore, it is correct to assume that the scaffold was homogeneous and isotropic everywhere inside and the estimate from one portion of the scaffold could be properly applied to the whole. The SHG analysis could clearly benefit from this assumption to give a precise estimate of the porosity. The equality with the P_{MPM} and P_{LEP} here also yielded another important message—that the Galwick testing fluid was not absorbed to cause further expansion of the scaffold while passing through, as expected by the service provider. When it comes to proper choice of fluid for LEP, it is essential to make sure that the fluid would not interact strongly with the body of the scaffold. This high similarity in data implied that Galwick is indeed a proper testing solution to minimize its diffusive effect on the scaffold. As a result, the porosity estimates from the surface signal and the bulk material property can become highly

similar for the freeze-dried scaffolds. This proves that the LEP method is a good control for the comparison with the MPM method, since the testing solution does not cause morphological changes to the scaffold body.

For the electrospun membranes, however, there existed a consistent offset between P_{MPM} and P_{LEP}. The main reason for such a decline in data agreement could lie in the bulk of the prepared samples. Due to the nature of the electrospinning process, it is not likely to create thick continuous electrospun scaffolds. Most of the electrospun samples are thin membranes that are typically less than 1 mm in thickness, so will not be compatible with LEP. When it is necessary to have a thicker scaffold, stacking the membranes is a non-ideal yet common practice. This directly results in creating pockets of void region between every two membranes. As the sample becomes thicker, the total pocket space become larger and can cause systematic errors in void space estimation.

This caused a difference between P_{LEP} and P_{MPM}, as P_{LEP} excluded such huge volume for porosity measurement but P_{MPM} seemed to include that instead. In this chapter, the LEP test successfully picked up the volume of these extremely large pores, as shown peaked between 2000 to 3000 μm in Figure 4.8. This means that the LEP test was nonetheless capable of distinguishing between the pores that were present inside the scaffold and the pocket spaces that were enclosed by the membranes, due to LEP's capability to survey the pore size distribution. MPM imaging from SHG sources, however, was not fine enough to distinguish these two types of pores. This causes an overestimate of the void space, as shown in Table 4.2. For the 3D electrospun scaffold, the bulk of the scaffold became inhomogeneous but consistent (with less errors in precision) for both the optical and the liquid extrusion methods. The reason that P_{LEP} was 27 % lower than the P_{MPM} could be that the pockets became dead zones for

Galwick to stagnate during the extrusion process. Considering the design of the extrusion channels, such a pool would require a much larger pressure to be driven through the hole, which may cause damage to the scaffold. As a result, a huge amount of Galwick was retained between the electrospun membranes, causing an underestimate of the total void space. This sort of offset is only assessable when the scaffold is subjected to certain fluids, so MPM imaging on the dried samples was unable to predict the resultant porosity that is relevant to cell migration inside the scaffold. Nevertheless, it is shown that estimated P_{MPM} values were stable. This means that the method might still be compatible if such constant offset is included in the calculation. Still, due to this ambiguity, the P_{MPM} evaluation method was not applied to the remaining electrospun samples in this thesis for porosity determination.

It is essential to consider the scientific ground before choosing the correct method for porosity evaluation. The mechanical principle behind LEP is more related to mass transport, therefore is by definition more related to diffusion and cell migration. Hence, such a method should be more applicable to tissue characterization. However, in this report there existed several limitations. Firstly, it required thick samples. Secondly, it required testing liquids, which may contaminate, damage, or alter the scaffold for further use. Thirdly, the equipment and testing liquid can be costly, but are limited to certain types of scaffolds only. On the other hand, the optical method by MPM is repeatable, well controlled, adaptive to various materials, and non-destructive. By using optical signals originated from the scaffold itself, the structure of the scaffold would be naturally revealed without further processing and modifications. SHG signals can be found in various biomaterials (e.g. elastin, microtubule, muscle myosin, fibronectin), so this optical method is not limited to gelatin/collagen-based materials only. The MPM

method is also more representative for scaffolds that undergo swelling in real-time tissue culture. Although at present this method is labour intensive and certainly requires technical training, the high precision from each measurement has demonstrated that it can at least provide a preliminary guideline for scaffold selection and significantly reduce the material cost for manufacturing. Certain drawbacks, such as the requirement for homogeneous material and structure and the offset calculation for dead-volumes, are important considerations but would not prevent the method from remaining robust. As technology improves, better objective lenses and motorized stages will become available. The outlook for the optical method should be quite promising. The best strategy would be to use the optical method for initial screening and designing of the scaffolds, and use the mass transport method for determinant assessment of the pore characterizations.

4.4.6 Comparison between the two aligned fibers

Amongst various methods to produce aligned fibers, PS and RD are fundamental, reliable, expandable, and economical. PS collects fibers simply through random deposition between collecting grounds. It relies on three presumptions: 1) the two strips are equally grounded, exposed to the same electric field and therefore draw away the fibers in the competitive manner and 2) the shortest distance between the two strips is perpendicular to the edge of the strip, therefore reducing the angle variances between fibers and 3) residual charges on the fibers can repel each other, therefore reducing the frequency of crossover. However, although it has been introduced for some years, there is no report on the real mechanism of how the fibers are aligned and how effective this method is. One of the purposes of this chapter, therefore, was to characterize this

method and identify the useful collection procedure for tissue scaffold. The experiment started from specification of the dimension of the collector. According to the investigation, a critical collecting period is 20 minutes. After 20 minutes, the spacing between fibers became smaller than 5 μm. This is an important value because this period not only yields a spacing smaller than the diameter of most free-floating cells (assumed to be 10 μm in cell body) (Dwane *et al.*, 2013), but also shows limited crossovers of fibers and tremendous high control over alignment angle. This allows cells to be grown on top of a thin membrane that have highly oriented fibers. Finally, a range of separation between the two strips was tested and whether eminent parameters would be affected by this separation was observed. The 2.5 cm separation turned out to be the most reliable, which yielded fibers with the minimum change of alignment angle (therefore minimizing crossover events). Thereafter, the PS method was optimized for controlled collection for later cell culture. The final membrane was visualized with RD and RM samples in Figure 4.12, proved to be a well-designed experimental group to provide contrasts with the RM control.

The RD collector, on the other hand, seemed to collect fibers in a Gaussian-like distribution across the collecting mandrel. The method was harder to control, but an advantage was that it created a wide variety of local fiber density. Therefore, it is easier to custom-make the scaffolds for optimization of cell seeding. The literature shows that at 4000 rpm the fibers are already aligned with only slight secondary bends, so it was used as the collecting speed for the samples here. It is reported, however, that faster rotating speed may result in an increase in the Young's modulus of the fiber macro-structure (Thomas *et al.*, 2006). A paper which presented a similar mechanical testing method can be used for comparison (Pedicini & Farris, 2003). As a result, if stiffness is

deemed as the primary cause to influence neurite extension, then the RD method will have a stronger potential in creating the most appropriate aligned fiber for neurons to grow. ESEM images in Figure 4.12 show that individual fibers have good quality. However, RD samples had a higher occurrence of cross-over occasionally. Therefore, it is ideal to treat RD as a transitional sample between PS and RM. RM fibers, however, have no obvious alignment or orientation, with crossover occuring everywhere in the scaffold. Hence, it served as a control group throughout the study for the evaluation of how crossover could affect the scaffold property and cell morphology.

4.5 Summary

In this chapter the effectiveness of the SHG signals from embedded gelatin as an assessable property was tested for the evaluation of the porosity of fibrillar scaffolds. Commercial porcine gelatin type A was embedded inside PCL electrospun fibers. The designed fiber was then compared with the freeze-dried collagen scaffolds for the integrity of the protein structure and the strength and resolution of the SHG signals for MPM. The results in this chapter showed that after electrospinning, gelatin was able to maintain its signature peaks for the α-helix, and the protein structure remained similar to that of the freeze-dried collagen. With blind deconvolution, the SHG imaging was able to enhance the SNR and distinguish the fibrillar structure for both the electrospun and freeze-dried groups. The scaffold microstructures were reconstructed from the MPM images for the evaluation of porosity. The results were compared with those of LEP. The analysis indicated that porosity evaluation using the combination of SHG signals and image processing is repeatable and non-destructive. Although it cannot fully replace

the standard, mechanical LEP method for porosity assessment because it could not distinguish the pores amongst fibers and the pocket space between membranes, the optical assessment can still be used for initial screening of continuous scaffold microstructure, significantly reducing the manufacturing cost and batch variance.

The fiber materials were then adjusted to create the proof-of-concept AFS. Although alignment methods for electrospun fibers have been developed for many years, it is quite difficult to draw a comparison amongst these methods because they collect fiber using different operating principles. In this report it was demonstrated that these operating principles could be simplified and controlled reasonably by assuming two fundamental methods—parallel metal strips (PS) and rotating drum (RD). Comparison with random fibers (RM) revealed that PS and RD samples were similar in stiffness, and both are stiffer than the RM samples. PS differed from RD in that it had better controlled alignment angle, resulting in less cross-over events.

Following the characterization of its SHG signal and alignment quality, the proof-of-concept AFS was used in a tissue culture experiment in the next chapter to demonstrate how the characterization process can be simplified yet enriched by the designed properties of this AFS.

Chapter 5 **Neurite outgrowth on the aligned fibrillar scaffold**

5.1 Introduction

Previously in Chapter 4, a prototypic 6 % (w/w) PCL-Gelatin fiber was created and investigated. From such a material, oriented fibers made from two fundamental alignment methods—parallel metal strips (PS) and rotating drum (RD)—were created. Their fiber diameter, density, alignment angle, and Young's moduli were characterized. In this chapter, the two fibers were used in the culturing of SH-SY5Y neurons for their potential uses in engineering nerve guidance conduits (NGCs). Results from the two groups are compared on the basis of how much neurite extension they could promote to illustrate the use of MPM for tissue characterization.

5.1.1 Nerve guidance conduits (NGCs)

Nerve injuries may involve severed neural networks, resulting in loss of neurons and forming gaps between connections. In an autograft surgery, which bridges the gap that may be too large for end-to-end anastomosis, several drawbacks exist: an additional surgical site is required, sacrifice of a donor nerve that leads to loss of function at that site, size mismatch between the two nerves, etc. (Evans, 2000, Francel *et al.*, 2003, Gunn *et al.*, 2005, Xie *et al.*, 2010b). Risk of neuroma formation at the donor site is also a serious consideration, which may further complicate the treatment by autograft or allograft. Overall success of this surgery is variable and sometimes incomplete. While xenografts from animal sources remain an alternative, they are subjected to immuno- and disease-related complications. In order to effectively solve these problems,

engineered **nerve guidance conduits (NGCs)** may offer promising alternatives, and several types have been developed with respect to different injury scenarios (Gunn *et al.*, 2005, Schnell *et al.*, 2007, Huang *et al.*, 2015). Advantages provided by such growth conduits include easier implantation in surgery, guidance to sprouting axons, retention of neurotrophic factors secreted from the damaged nerve, and prevention of infiltration from fibrous tissue. Therefore, NGCs have become a practical solution to the existing dilemma in neural surgery.

Although at present NGCs are more likely to be developed for peripheral nerve repairs, they are also promising for the repair of damage to the central nervous system (CNS), such as spinal cord injuries. Mammalian CNS neurons were once thought to be unable to regenerate (Asada *et al.*, 1998). However, studies in recent years have shown that with a proper scaffold/substrate, it is possible to grow CNS neurons or astroglial cells. This can be illustrated by the fact that several papers have been published using CNS neurons or astroglial cells. For example, Deumens *et al.* (2004) demonstrated that the alignment of glial cells on poly(D,L)-lactide matrices could direct neurite outgrowth of CNS neurons. Recknor *et al.* (2004) showed that astroglial cells could be oriented on micropatterned polystyrene substrates, which caused 85 % of the cultured astrocytes to be aligned. But one key issue that delays the NGC research is the lack of a method that would encourage the cultured neurons to grow parallel and longer, which can significantly increase the clinical potential of such a tissue product. Ideally, the NGCs should provide a dynamic range of neurite length for surgical needs. In order to make NGCs more appealing in CNS treatments, it is desirable to have a robust, standardized, economical, agent-deliverable, and surgically possible method to facilitate neurite outgrowth. For this reason, in recent years electrospun membrane has been used to

culture neural tissues that may be used for transplantation (Corey *et al.*, 2007, Ghasemi-Mobarakeh *et al.*, 2008, Wang *et al.*, 2012, Huang *et al.*, 2015). It is worthwhile to look into possible electrospinning methods that may guide neurite growth (e.g. alignment).

5.1.2 SH-SY5Y cells in the literature

SH-SY5Y cells were selected as the neural model for this demonstration. Considering the complexity of this study, it is important to start this investigation with a reliable cell line in order to minimize the effects from cell culture. SH-SY5Y cells are human neuroblastoma cells that have been established as a stable and reliable dopaminergic (DAergic) neuronal cell model for the study of pathogenesis of Parkinson's and Alzheimer's Disease (Agholme *et al.*, 2010, Xie *et al.*, 2010a). These cells were originally obtained from a bone marrow biopsy of a neuroblastoma patient with sympathetic adrenergic ganglial origin in 1970's (Biedler *et al.*, 1973). It was later found that this cell line can differentiate into functionally mature neuronal phenotype under the influence of many agents (Pahlman *et al.*, 1981, Singh & Kaur, 2007, Cernaianu *et al.*, 2008). For example, Encinas *et al.* (2000) showed that sequential exposure of these cells to retinoic acid (RA) and brain-derived neurotrophic factor (BDNF) could generate fully differentiated, neurotrophic factor-dependent neurons. Upon switching the cells into the differentiated state, it is possible to interrupt their proliferation, maintain the cells at a constant and desirable number and facilitate neurite outgrowth (Fagerström *et al.*, 1996). These studies show that it is a neural cell-line that can be controlled at various stages, which is particularly important if a certain level of cell-cell interactions is beneficial for tissue maturation. According to Dwane *et al.* (2013), this cell line is compliable with various material surfaces and can sustain a high percentage of differentiated population. This cell line also presents viable neurons and

apparent neurite formation when cultured in 3D matrices such as collagen or matrigel (Li *et al.*, 2007). Hence, using SH-SY5Y as the prototypic cell line may effectively simplify the design of the experiment.

5.1.3 Cell-substrate interactions

Parameters for cell-substrate interactions are influential for neurite development (Mattson *et al.*, 1988), therefore it is essential to control the physical and chemical parameters as much as possible. There are molecular and substrate factors that may influence neurite outgrowth. This chapter investigates the cell-substrate factors only because an agent-releasing system is best designed with a well-characterized substrate/loader. In terms of the substrate effects, Wang *et al.* (2009) investigated the nanofiber-related parameters when a collection disk was in use to make the aligned poly-L-lactic acid fibers for culturing dorsal root ganglia and rat Schwann cells. They laid out a number of geometric factors that should be considered when developing neurite scaffolds: fiber alignment, fiber density, fiber diameter, and spacing between fibers (width of groove). They also speculated that the diameter of the fibers should be related to the axonal diameter. In terms of the mechanical property of the substrate, Leach *et al.* (2007) showed that neurite outgrowth and branching were limited on very soft substrates. This means that the stiffness of the fibers that are compared would also need to be controlled to a certain range. These provide the challenges in drawing a proper conclusion from such a neurite-outgrowth study.

5.1.4 Culturing neurons with polycaprolactone

Polycaprolactone (PCL) is one of the well-received biomaterials for neural engineering. This synthetic material is able to provide a surface for neuron adhesion,

migration, proliferation and differentiation. Schnell *et al.* (2007) demonstrated that modified poly-Ɛ-caprolactone nanofibers could be used as a suitable substrate for supporting cell proliferation and neurite outgrowth for artificial nerve implants. A PCL fiber with collagen supramolecular organization has also been proved to generate a better collagen/axons suprastructure and more reactive Schwann cells (Maturana *et al.*, 2013). It also possesses the potential to be used in agent delivery if such a chemical reagent is required for cell differentiation (Chang, 2009, Han *et al.*, 2011, Liu *et al.*, 2011, Wang *et al.*, 2012). For example, Low *et al.* (2013) demonstrated that it is possible to direct neuronal differentiation through the use of PCL nanofiber/film that releases siRNA targeting the RE-1 silencing transcription factor (REST). Such a combination of the fiber material and the released agent successfully enhanced the neural stem/progenitor cells (NPCs) commitment toward neurons rather than astrocytes and oligodendrocytes. Another study in 2007 showed that both PCL and PCL-collagen fibers could support oriented neurite outgrowth and glial migration from dorsal root ganglia explants, though the PCL-collagen mixed fiber presented a more suitable substrate for this attempt (Schnell *et al.*, 2007). A collagen-based 3D matrix made from lyophilisation was used to test effects from growth factors on SH-SY5Y cells, and showed that these cells could be successfully cultured and induced into neural phenotypes (Labour *et al.*, 2012). Ramakrishna and colleagues presented a similar PCL-Gelatin study on neural engineering (Ghasemi-Mobarakeh *et al.*, 2008). According to their finding, the PCL-Gelatin 70:30 mixed fiber proved to enhance cell viability and regenerated neurons from C17.2 cells, a neuron precursor cell line from mouse. The formula may also provide extra sites for cell adhesion and less compensation in tensile

strength compared to the PCL-Gelatin 50:50 formula. The same formula should be useful for neural regeneration from the human SH-SY5Y cell line.

5.1.5 Cell growth on aligned nanofibers

It is interesting to investigate how alignment of the electrospun nano-fibrillar scaffold may influence cell morphology. The main reason is that it has been proved to be useful in making biomimetic scaffolds made of synthetic and natural polymers, including protein-based materials, which facilitates the cell-culture process (Li *et al.*, 2005). For tissue engineering, aligned substrate is an important aspect for successful cell differentiation. For example, Daud and colleagues (2012) presented an aligned electrospun PCL scaffold for developing 3D peripheral nerve models *in vitro*. In their study, the longest neurite detected was on 8 µm fibers when cultured alone. Teh *et al.* (2013) show that aligned silk fibroin electrospun scaffold is able to promote the tenogenic differentiation of mesenchymal stem cells (MSCs). Lyu *et al.* (2013) used aligned PLGA-based electrospun fibers for guided bone repair and reconstruction. Gnavi *et al.* (2015) showed that aligned electrospun membrane could be used to culture primary cells, such as RT4-D6P2T cells, primary Schwann Cells, and 50B11 cells. In brief, these prove that research in AFS is state-of-the-art and prominent for complex tissue engineering.

5.1.6 Multiphoton-image processing for tissue characterization

One additional investigation in this chapter is to see how three dimensional (3D) imaging tools such as multiphoton microscopy (MPM) and image processing software can further help to illustrate better cell-substrate interaction and neurite morphology. The use of stereological methods on fluorescent images may provide a new counting

method for the better estimate of viability ratio. While analyzing tissue samples in this manner, a "design-based" method (such as the spot objects) refers to the use of probes and the sampling schemes that are defined *a priori*, so one does not need to take into account for the size, shape, spatial orientation, and spatial distribution of the cells (West, 2002, Schmitz & Hof, 2005). This results in more straightforward data, especially for the estimates of total neuron number while reducing systematic errors. Automated filtering by the cell size made certain that cell debris was uncounted for, as may happen while counting manually. Coupled by the threshold analysis by the current imaging tools, this method takes the advantage of being volumetrically thorough, thus clearly identifying the spatial relationship between the cell clusters and proximal substrate regions. This could increase the precision of the viability estimate and identify the cause if there is apparent decline in the ratio. In order to further increase the reliability of the "design-based" method, it is essential to use either confocal or multiphoton to generate finer sectioning (Peterson, 1999). Considering the rise of the need for non-invasive characterization of tissue products, this semi-automated stereological analysis coupled with infrared light source can provide a reliable solution. The use of stereology may also help illustrate the morphology of neurites in three dimensions, showing how the neurites interact with the scaffold. The use of multichannel recording on MPM can simultaneously display features from both the scaffold and the cells. In a case where neurons would be grown in 3D scaffold, neurite extension can crawl along the nanofiber and be underestimated with conventional 2D imaging such as scanning electron microscopy or fluorescent microscopy. The MPM method acquires slices through the whole 3D space, having more precise measurements on the neurite lengths by a

regression from vertical slices. Therefore, slight differences between neurite lengths in different samples may be identified and analysed statistically.

In short, experiments in this chapter continue from the previous chapter by testing SH-SY5Y neurite outgrowth on the aligned fibrillar scaffolds created by PS and RD alignment methods, and the data are evaluated using MPM and design-based image processing tools for better observations on neurite-substrate interactions.

5.2 Materials and methods

5.2.1 Materials and devices

Polycaprolactone (PCL, Mv 70,000 ~ 90,000 Da) pallets and Type A Gelatin from porcine skin were obtained from Sigma. Hexafluoroisopropanol (HFIP) was obtained from Apollo Scientific Limited. Nunc™ Thermanox™ Coverslips that had tissue-culture treated polyester films surface were obtained from Thermo Scientific. The polymer solutions used for electrospinning were 6 % w/w PCL Only and PCL:Gelatin = 70:30 in HFIP.

5.2.2 The electrospinning process

Aside from the collectors in used, all electrospun fibers were formed with the same condition. The applied voltage for PCL Only fibers was 6.5 kV to 7.0 kV, and that for the PCL-Gelatin fibers was 10 kV to 11.5 kV. The inner diameter of the spinneret was 0.8 mm. The distance between the Taylor cone and any of the three collecting grounds was 13.5 cm. The flow rate of the solutions was 1 mL/hr. 1 bar of nitrogen gas was also applied during the collection.

The experimental samples from the parallel metal strips (PS), rotating drums (RD) and flat metal plate for random collection (RM) were collected using the same collectors in the same manner as described in the previous chapter (Section 4.2.2).

5.2.3 Cell-substrate characterization

SH-SY5Y cells were brought up from liquid nitrogen using Standard Culture Media in T25 flasks, and passed using Trypsin at 90 % confluence every three days. Standard Culture Media consisted of RPMI media, 10 % FBS, 1 % MEM (PAA), 1 % Penicillin/Streptomycin (PAA), and 1 % L-glutamine (PAA). All cells were at passage 9, fed every three days.

Viability tests were conducted using MPM, and the ratio of live/dead objects were analysed with Imaris 7 (Bitplane). Randomly collected membranes (RM) were electrospun for 20 minutes. Two experimental groups—PCL Only vs PCL:Gelatin (70:30)—were created to compare the material preference of the SH-SY5Y cells. The Nunc™ Thermanox™ Coverslips without fiber were used as a 2D cell-culture control. 150,000 cells were added to each sample (n = 3 each). After 3 days of cell culture, the cells were stained with Invitrogen Live/Dead staining kit. Ethidium homodimer would stain the DNA of broken cells in red, whereas calcein-AM would stain plasma membrane of live cells in green.

5.2.4 Multiphoton microscopy

3D images were acquired from a modified BioRad Radiance 2100MP multiphoton microscope (Zeiss; Jena, Germany). Near infrared (NIR) laser beams of λ = 800 nm were generated from a tunable femtosecond pulsed Ti:sapphire laser (Mira 900-F; Coherent, Ely, U.K.) pumped by a 10 W multiline argon ion laser (Verdi; Coherent).

A 20X air-objective (NA = 0.75) was in used. The 3D cell counting was conducted using the spot objects of Imaris 7 with an estimated spot size of 10 µm with respect to observed cell size. Imaging session was completed within 3 hours post staining.

5.2.5 Cell metabolics study

alamarBlue® assay (Invitrogen™ corp., USA) was used to record cell metabolic activities for every 24-hour time point on days 1, 2, and 3. At each time point, the cells were pre-incubated with alamarBlue culture media for 2 hours, with fluorescence intensity read by a spectrophotometer at excitation 560 nm and emission 590 nm (n=4). Each well was loaded with 100 µL and read 30 times. Afterwards, the cells were fed with fresh Standard Culture Media until next time point.

5.2.6 Neurite growth analysis

After fiber characterizations in Chapter 4, it was determined that 20-minute was an ideal duration for all three collectors to create porous 3D scaffolds for neurons. PS fibers were collected with Nunc coverslips with 2.5 cm separation. RD (at 4000 rpm) and RM fibers were collected using foil sheets. All samples were punched into discs that were 13 mm in diameter and sterilized by ultraviolet lights to serve as scaffolds for neurite outgrowth (3 repeats for each group).

In order to analyse scaffold effects on neurite extension, SH-SY5Y cells that were differentiated by nerve growth factor (NGF) and brain-derived neurotrophic factor (BDNF) were used in the final neurite outgrowth study. Cells were cultured using a Differentiation Media that was similar to the Standard Culture Media used in the viability study above, but 10 µM of retinoic acid (RA, all Trans, Sigma-Aldrich) was

included. Cells were initially seeded at 35,000 cells/well in a 24-well plate and cultured for 5 days before neurite stimulation.

For neurite outgrowth stimulation, Neuron Culture Media, which consisted of Neuron Base Medium (PAA), 2 % Stem Cell Supplement (PAA) or B27 (Life Technologies), 1 % MEM (PAA), 1 % L-glutamine (PAA), and 1 % penicillin/streptomycin, were made up. Right before it was used for cell feeding, 50 nM BDNF and 10 nM NGF were added. The cells were then cultured for neurite extension for another 3 days before immunohistochemistry (IHC) staining.

In IHC, the samples were then washed by Dulbecco's Phosphate Buffer Saline (PAA) and fixed by 4 % formaldehyde (Sigma). The cell samples were stained with neuron-specific class III beta-tubulin (Tuj1) markers. Mouse anti-Tuj1 and DAPI antibodies were used to provide fluorescent signals for easier observation of neurites under MPM. With the same computer system in Section 4.2.9, these 3D images were later blindly deconvolved with AutoQuant X3 and reconstructed with isosurface objects for the morphology analysis. 3D neurite lengths were measured by a Fiji plug-in [NeuriteTracer (Pool *et al.*, 2008), n = 100]. The length of a neurite was defined as a cell with a dendrite extension greater than the length of the cell body [on average greater than 10 μm according to Dwane *et al.* (2013)].

5.2.7 Statistics

Measurements on cell viability (n = 3), metabolic (n = 4), and neurite outgrowth (n = 100) were presented as mean ± standard error of the means (SE). Statistical analysis was carried out with either Student's *t* test or one-way Analysis of Variance

(ANOVA) with multiple comparisons against the RM group in GraphPad Prism 6 (version 6.03). $p < 0.05$ was considered to be statistically significant.

5.3 Results

5.3.1 Cell-substrate characterization

The cells were seeded directly on culture plate surface (2D Nunc control) and some random fibers made of PCL and PCL-Gelatin solutions. It was found that the cell viability from 2D was 89.56 ± 0.63 %. The value for PCL only fiber was 50.63 ± 1.61 %, whereas that from the PCL-Gelatin mixed fiber was 65.37 ± 7.81 %. 3D analysis was performed with Imaris 7, and some of the cell-count results are shown in Figure 5.1. The MPM images, though deconvolved, show difficulty in distinguishing one cell from another in cell clusters. Although it was able to show 3D cell culture, such images would be difficult for analysis due to the lack of Z-axis resolution. The spot-object application, however, made it possible to display the population, distribution and penetration of cells in the environment. It was previously shown that 20-minute collection of random fibers could create scaffolds that were porous enough to facilitate 3D cell culture. It was depicted that the cells had different depths of penetration in PCL-Only and PCL-Gelatin scaffolds after 3 days of culture. 3D cultured cells showed reduced viability compared to the 2D control, and PCL-Gelatin mix seemed to increase the cell viability slightly, possibility due to providing more RGD sites for cell adhesion. From Figure 5.2, the alamarBlue assay over a 3 day period supported the observation that both PCL Only and PCL-Gelatin scaffolds could sustain cell growth, long enough

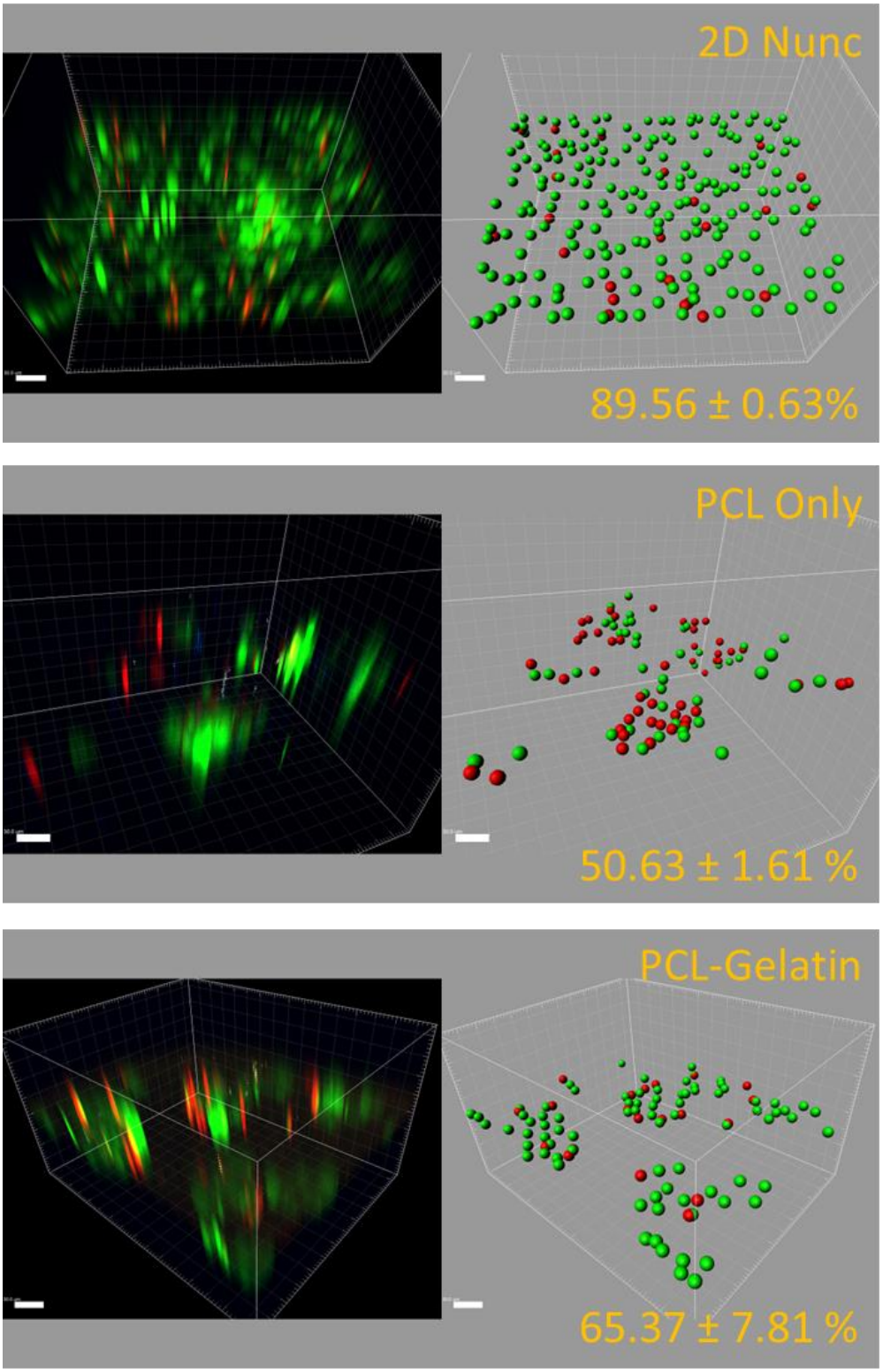

Figure 5.1: Cell viability staining on different randomly spun materials. On the left were deconvolved MPM images. On the right were the same images processed using spot objects. Green spheres indicate live SH-SY5Y cells; red spheres indicate dead SH-SY5Y cells. Major tick = 20 μm; scale bar = 30 μm. Average viability ratio is labeled for each group (with 3 repeats).

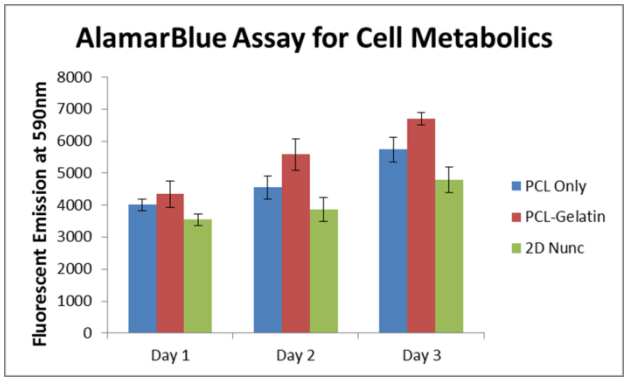

Figure 5.2: alamarBlue assay for cell metabolic activities over three days. All three groups show normally increasing metabolic activities throughout the period (n = 4).

for the differentiation protocol in use. As a result, the PCL:Gelatin (70:30) formula, which showed slightly higher viability for 3D SH-SY5Y cells, was used for the remaining sections of this study.

5.3.2 Neurite Analysis

In IHC the arrangement of neuron-specific class III beta-tubulin (Tuj1) was explored in cells from each group. Figure 5.3 shows isosurface reconstruction of the cells and fibers. PS and RD groups displayed clear neurite outgrowths from cell clusters, which wrapped around the electrospun fibers in a 3D manner. RM neurons, however, did not show clear neurite extensions. Isosurface reconstruction and NeuriteTracer analyses for both the cells and the fiber showed that cells preferred to grow at areas with higher fiber density, then developed neurites along the orientation of the fibers. Growing cells on mesh of this density did not facilitate cell adhesion on single fibers only, but drove neurites to extend away from cell clusters. Histogram of neurite lengths is displayed in Figure 5.4, and the statistical values were summarized in Table 5.1. In

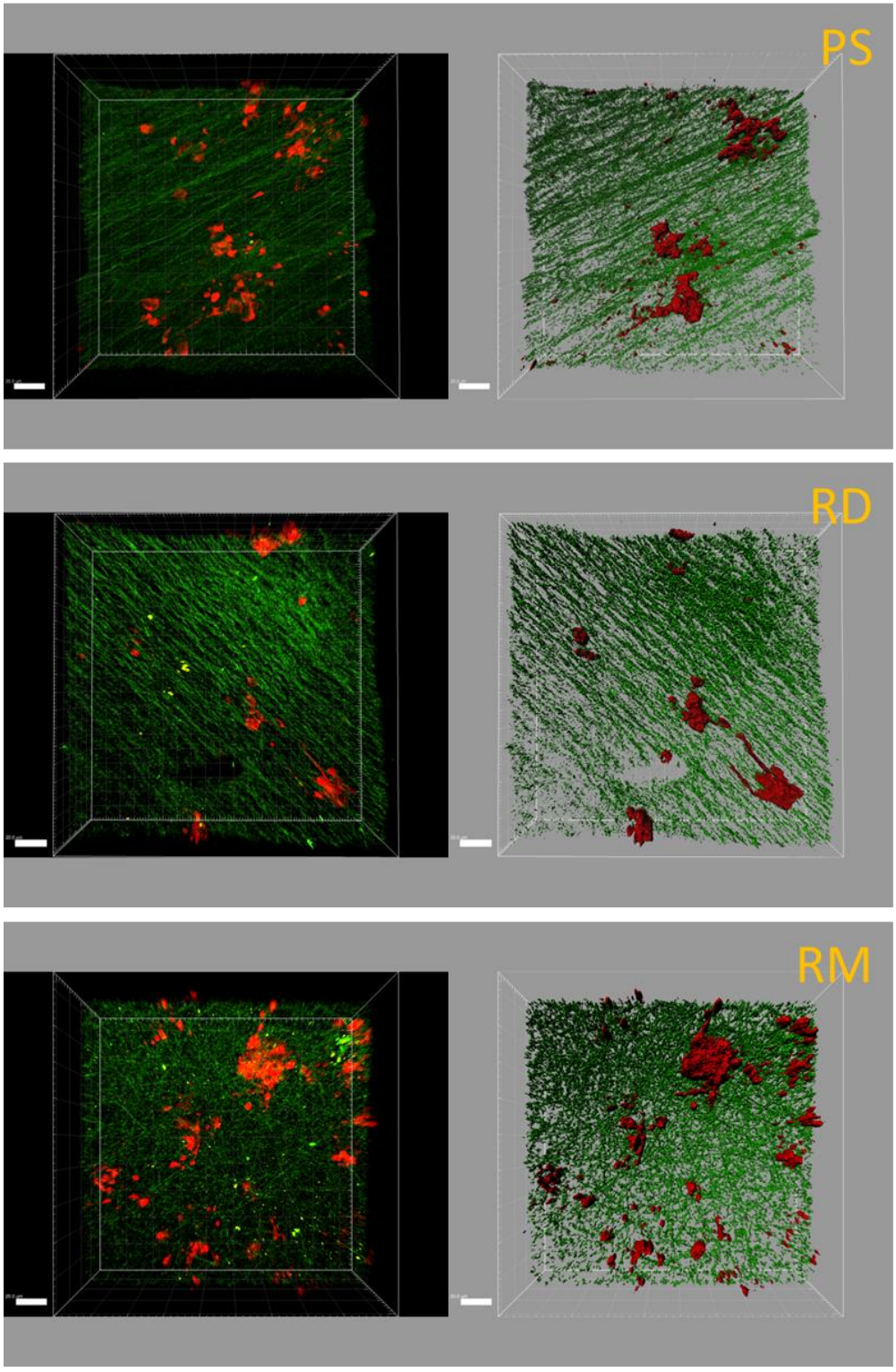

Figure 5.3: Immunohistochemistry results on Tuj1 development in SH-SY5Y cells. LEFT: Deconvolved MPM images. RIGHT: Isosurfaces reconstruction of the fibers and cell clusters to show spatial relationships. Green = SHG signals from the fibers; red = neuron cluster as stained for Tuj1. Scale bar = 20 μm. PS: parallel metal strips; RD: rotating drum; RM: randomly collected. Each group has 3 repeats.

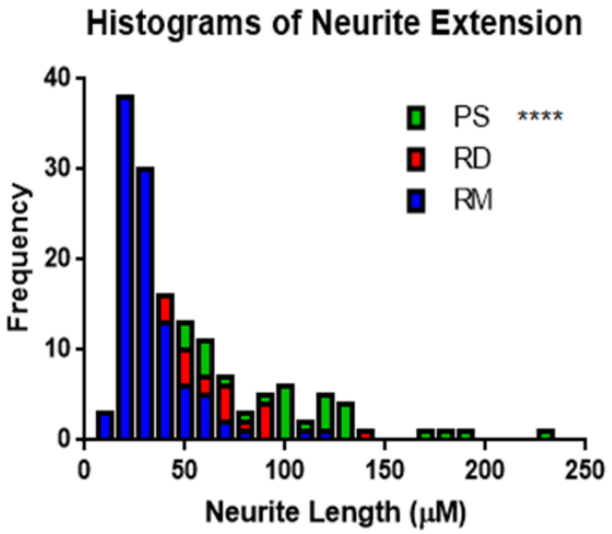

Figure 5.4: Histogram of neurite lengths from the three groups. Neurons on the parallel metal strips (PS) sample showed significantly longer extension compared to the neurons on rotating drum (RD) and randomly collected (RM) electrospun membranes (n = 100, **** means $p < 0.0001$). Statistics assessed using one-way ANOVA with multiple comparisons against the RM group.

Neurite Length (μm)	PS	RD	RM
Minimum	17.0	15.1	14.6
25% Percentile	32.1	23.0	20.8
Median	53.4	33.6	27.0
75% Percentile	90.0	52.6	39.3
Maximum	229.4	144.3	124.3
Mean	**64.1**	**39.6**	**32.5**
Std. Deviation	41.4	22.1	18.2
Std. Error of Mean	4.1	2.2	1.8
Lower 95% CI of mean	55.9	35.3	28.8
Upper 95% CI of mean	72.3	44.0	36.1

Table 5.1: Statistics of neurite length measurements (n = 100).

terms of mean values, PS >> RD > RM. One-way ANOVA with multiple comparison shows that the PS group was significantly different from the RM control group ($p < 0.0001$). RD group, however, was not significantly different from RM. This indicated that the PS mesh was efficient in promoting neurite outgrowth compared to the RD group. Although the two methods were both good at creating aligned fibers, neurons showed higher preference for neurite development on the PS fibers.

5.4 Discussion

5.4.1 Challenges in AFS functional studies

This chapter is novel in that it directly compared neural cultures from two fundamental alignment methods for electrospun AFSs. Although research in AFS design is ongoing and newer alignment methods emerge in the literature every year, there was no report that directly points out the differences amongst them and how such differences may contribute to changes in tissue culture. In other words, there was no indication that a particular factor from the aligned scaffold would actually contribute dramatically to the guided cell culture and therefore the overall tissue function. There are two main reasons for this: (1) it is difficult in practice to directly compare existing alignment methods, and (2) there is a lack of a proper 3D characterization method that may help visualize the scaffold and the cell culture simultaneously.

For reason (1), many of the newer alignment methods were not completely characterized and theorized. Forcing a single electrospun jet to be attracted in a certain direction itself is a very challenging question. The nature of this collecting mechanism requires a point-to-area deposition under the influence of the electric field. The lack of

fine control over the field is the reason that such alignment can only be achieved moderately, at best explained by a probability theory. Yet electrospinning remains the only technique to create continuous nanofibers for AFS design, so it is difficult but necessary to interpret the cell growth from such uncontrolled methods. It is also noteworthy that due to slight differences in the design of the electrospinning apparatus, results from one lab are not likely to be fully reproduced in another. Fortunately, after enough surveying of the existing methods, it was exactly because of the point-to-area nature of electrospinning that these alignment approaches could be converged into the two scenarios: random deposition between plates and drawing mandrel. One relies on the randomness and residual charges on the fibers, and the other relies on the rotary motion to force the fiber to be drawn in an oriented direction. They align the fibers on two very different principles, hence forming the ground for the direct comparison in this chapter.

To elaborate on reason (2), analysis of the tissue culture performance and possible functional recover from a 3D AFS requires a specially designed characterization system. It is challenging to observe and record nano-fibrillar signals in a microscope because such a signal is typically too weak to yield useful information. Even with the help of an SEM, the researcher still risks the contamination and destruction of the scaffold. Without a reliable understanding of where the fibers in the 3D AFS are, it is not likely to draw a correct conclusion on how the cells are guided and grown on the scaffold, not to mention how many physiological functions can be recovered. For example, neurons that are grown on a 3D AFS can show neurite extension in the Z-axis as well. Yet this information is commonly disregarded in many current papers, as they draw conclusions from measurements on 2D images. While

comparing neurite outgrowth on these two highly effective alignment methods, it is necessary to gather complete cell data if possible. The MPM imaging and the NeuriteTracer tool that were presented in this chapter have been proven to be capable of detecting such slight changes. In these images, both the cell morphology and the fiber orientation were recorded and overlapped for the study of cell-substrate interaction in 3D. Such a methodology has created a platform that may be further upgraded for functional assessment or non-invasive tissue/organ characterization. This will provide new design direction and significantly aid current research in 3D AFS targeting successful transplantation and tissue integration.

5.4.2 Tissue culture with PCL:Gelatin fibers

With respect to the cell culture material, the PCL:Gelatin (70:30) fiber seems to be suitable for this study. Spot object analysis from the MPM imaging of cultured SH-SY5Y cells has proved to be useful in analyzing the viability of the cells after 3 days of culture. It is accurate, easy to use, and reliably gives good assessment over viability in 3D cell culture. The "design-based" technique is able to assist researchers in counting objectively with respect to a pre-determined fluorescence intensity representing live or dead cells only, so the results are not biased by the morphology of neurons (West, 1999). PCL-Gelatin fibers also have the advantage of yielding SHG in laser microscopy, which could help researchers understand the cell-substrate interaction without the need of extra staining. The result in Figure 5.1 echoes the alamarBlue test for cell metabolism, as stronger metabolic activities were observed throughout the three day period, and the PCL-Gelatin scaffold showed higher activities than the PCL-Only scaffold at least for the first three days. This proves that the PCL-Gelatin scaffold is useful in promoting cell

adhesion and growth. This period also provided enough coverage over the period for the differentiation protocol, therefore should yield enough contrast to observe differences in neurite developments.

The viability study results show that the PCL:Gelatin (70:30) formula was clearly preferable to the PCL-Only formula. The extra cell adhesion sites and material softening provided by gelatin might be the reason behind this observation. This study also shows that the PCL-Gelatine is not only useful in culturing the C17.2 cells as shown in the previous report (Ghasemi-Mobarakeh *et al.*, 2008), but also useful in culturing SH-SY5Y cells. However, the relatively low cell viability rate (65.37 % vs 70.1 %) indicates that unlike C17.2 cells, the SH-SY5Y cells might less prefer growing on this fiber. Since the SH-SY5Y cells used in this study were relatively young (passage = 9), it is possible that this discrepancy in cell preference came from some innate properties of these two cells, which may involve the expression level of integrin/cadherin on the membrane of both cell types and other subtle factors. More studies into the gene expression profile of the two cell types may provide some insights into how the fiber material properties affect the cell preference.

5.4.3 SHG imaging for 3D scaffold characterization

In the analysis of IHC, the SHG signals from the fibrillar scaffolds were strong enough to be used to generate isosurface. Due to the small size of the fiber diameter, SHG signal from the fibers were weak for volumetric analysis. However, the isosurface technique still provided strong 3D contrast between the neurites and the nanofiber. The result shown in Figure 5.3 indicates that such a method could successfully detect the front edge of the neurites and provide enough separation from the underneath fiber,

which is not something easily done by simple MPM imaging alone. Although there might be limitations on precise volume rendering of the reconstructed fiber, this method can nonetheless assist in the analysis of the fiber alignment and 3D neurite growth.

From the IHC images, it is shown that both PS and RD neurons could develop neurites that grew in the direction of the fibers. The length measurement further shows that PS neurites were significantly longer than the RM neurites, whereas RD neurites showed only a slight increase ($p < 0.05$ when compared by Student's t test). The method was done accurately by going through a range of Z-axis slides in order to obtain a more reliable value, a consideration that is often omitted by conventional 2D microscopy. Considering the results from Young's modulus, it has been shown that stiffness of the fiber was not the major cause that prolonged neurite outgrowth in this case. Although elastic modulus of RD was twice as much as that of RM, RD neurite extension was only slightly longer than that of RM. As a result, the major contributor to whether the neurite can extend longer is the frequency of the crossover events (and therefore the alignment angle). When the frequency increases, neurite extension would be further limited. Hence, in order to promote neurite outgrowth using the aligned fiber method, it is important to have high control over alignment angle. For this reason, the collector design should take advantage from the PS concept.

In IHC, although it is unlikely to separate individual cells in the neuron clusters, it is relatively easy to distinguish the edges between a neurite and the proximal substrate, due to the fact that they were recorded on different channels and could be processed separately. Reconstruction of the nanofibers, although lacking volumetric precision, was able to clearly present the orientation and topography of the scaffold. This becomes important in identifying the neurites that extend under the influence of the surrounding

substrate. Rendering the cell clusters semi-transparent can help demonstrate how the cells adhere to the substrate in a 3D manner—how much wrapping motion is involved in the adhesion of neurons. A caveat, however, is that the Z-step in acquiring the 3D images needs to be small enough so that the collected information can be used in later regression of the cell shape in Z-axis. With proper operation, the resultant images should be a simplified representation of the 3D environment. The next step will be including analysis over the ambient factors, such as local pH, for a more useful data analysis. All these prove that the combination of MPM recording and image processing tools can be valuable in statistical analysis of neurite outgrowth. With minimized preparation, this method eliminated issues resulting from batch variance of scaffold making, thus increasing the credibility of the overall tissue culture results.

5.5 Summary

Functional recovery of the nervous system, which is composed of bundled neurons that show directionality for signalling, requires fully matured, differentiated, and aligned neurons. A properly aligned 3D AFS such as a nerve guidance conduit (NGC) is needed to provide such a ground for tissue culture. NGCs require elongated neurites to become more applicable in transplantation, and it was hypothesized in this chapter that a properly selected alignment method could lead to significantly longer neurite outgrowth. Here, the AFSs from two fundamental alignment methods—parallel metal strips (PS) and rotating drum (RD)—were compared directly for their capability to induce neurite outgrowth of the model neurons SH-SY5Y. A specifically designed 3D SHG/MPM imaging system was designed to provide consistent information

regarding the cell viability, distribution, differentiation, and morphology throughout the experiments in this chapter. According to the results, the PCL:Gelatin fiber in use enhanced SH-SY5Y cell viability and metabolics over the period of 3 days. When such a nanofiber was aligned with PS and RD and used in the culture of differentiated SH-SY5Y, it was found from 3D NeuriteTracer calculations that the neurite length of PS neurons (mean = 64.1 μm) was significant longer than that of the RD neurons (39.6 μm) ($p < 0.0001$). When this data was compared with the data from Section 4.3.6, it could be illustrated that the PS fibers induced longer neurite outgrowth because it had a smaller variance in the degree of alignment (i.e. less frequency of fiber cross-over). Since the Young's modulus and the fiber diameter were not significantly different, it was therefore concluded that the degree of alignment was the most important parameter that caused this extension of SH-SY5Y cells. Overall, the work in this chapter identified the key component for NGC designs, and has provided evidence for the reasoning that a proper choice of the alignment method can optimize the tissue culture, leading towards the promised functional recovery of the designed 3D AFS.

In the next chapter, the imaging strategy that was used in this chapter was applied to a fully 3D scaffold non-invasively for the analysis of the relationship between substrate structure and the scaffold function.

Chapter 6 **Characterization of decellularized cornea scaffolds**

6.1 Introduction

Previously in Chapter 4, it was shown that, with manual thresholding, the isosurface method could characterize the porosity of the homogeneous, 3D freeze-dried collagen scaffold precisely. In this chapter, the focus has been shifted to evaluate the possibility of using automated thresholding for non-invasive characterization of another fully 3D AFS (e.g. decellularized corneal stroma). The analyzed SHG signals may present a novel way to study the relationship between the scaffold microstructure and potential physiological function.

6.1.1 The need of cornea transplant in clinics

Corneal disease is the major cause of blindness, second only to cataracts in overall importance, and its epidemiology is complicated and encompasses a wide variety of infectious and inflammatory eye diseases (Whitcher *et al.*, 2001). Burden of blindness from eye injuries falls most heavily on developing countries (Jackson, 1996). Up to 5% of all blinding conditions in the developing world are directly related to ocular trauma and subsequent infection (Whitcher & Srinivasan, 1997). Trachoma, being the world's leading infectious cause of blindness and ocular morbidity, affecting 146 million people worldwide (Taylor & Taylor, 1999). Eye-bank facilities, modern operating rooms and equipment, and well-trained surgeons and nurses are rare in regions where severe trachoma is endemic. Corneal transplantation (i.e. keratoplasty) is the only form of therapy for the corneal disorders that lead to blindness (George &

Larkin, 2004). The majority of corneal transplants are conducted by the excision of a 7-8 mm diameter circle from the recipient cornea, and replacing it with a specimen of similar diameter from donor cornea. But the treatment, like many other grafting surgeries, has a low number of available donors. It is therefore essential to find an alternative supply for grafting scaffolds.

6.1.2 Physiology and anatomy of cornea

In response to the shortage of transplantable human cornea, porcine cornea may be a good source for developing substitute scaffolds. Porcine cornea is only slightly thicker than human cornea (Faber *et al.*, 2008). The immune privilege in human eyes makes the transplantation with decellularized porcine cornea feasible (Streilein, 2003, Niederkorn, 2006). In terms of anatomy, a porcine cornea has a horizontal diameter of 14.31 mm and vertical diameter of 12.00 mm (Sanchez *et al.*, 2011). The two diameters for human are 11.7 mm and 10.6 mm. As a result, the two types of cornea show similarity in aspect ratio. The central corneal ultrasound pachymetry was measured to be 877.6 ± 13.58 μm and slit-scan pachymetry, 906.2 ± 15.30 μm. The ultrasound pachymetry is between 1013 ± 10 μm *ex vivo* (Jay *et al.*, 2008) and 666 μm (534~797 μm) in a live pig (Faber *et al.*, 2008). It is in general thicker than human cornea and therefore easier to be modified. In terms of biomechanical properties, porcine cornea can be used as a satisfactory model for human cornea research if tensile strength and stress-strain relationship are the only mechanical factors to be considered (Zeng *et al.*, 2001). Stress relaxation, however, is quite different between porcine and human corneas, as also observed by Elsheikh *et al.* (2008). In terms of the stroma structure, porcine and human corneas are similar in that human stroma has collagen lamellae thicknesses that

range between 5 and 8 μm, whereas the porcine ones range between 4 and 5 μm, slightly smaller than human lamellae (Bueno *et al.*, 2011). Collagen fibrils with a small diameter 25-30 nm are regularly packed within lamellae. Human stromal collagen lamellae gradually become less wavy as they get deeper within the cornea. Porcine stromal collagen lamellae, however, do not display this tendency and show two main orientations set approximately 90 degrees apart. Cell bleaching methods for naturally-derived corneal scaffolds have been described in literature (Xu *et al.*, 2008); it is possible to turn a porcine cornea into a 3D parallel scaffold for cell seeding. Therefore, even though few differences in tissue properties are present, porcine cornea can be highly valuable for human cornea research or even transplantation.

While designing corneal scaffold, it is important to set criteria with respect to the human visual mechanism. In general, the cornea consists of five layers: epithelium, Bowman's layer, stroma, Descemet's membrane, and endothelium (DelMonte & Kim, 2011). As a scaffold design criterion, the human pupil opening has a normal range of 2~9 mm in diameter (Winn *et al.*, 1994). Hence, the dimension of the cornea scaffold should be able to fully cover this area. Human cornea is approximately 535 μm in thickness, with the anterior radius of curvature having an average of 7.8 mm (Doughty & Zaman, 2000, Courville *et al.*, 2004). The axial refractive power for an average cornea remains roughly unchanged throughout the area covering pupil (Klein & Mandell, 1995, Hashemi & Mehravaran, 2010). For human, the stroma constitutes 90 % of the total thickness of the cornea (Hassell & Birk, 2010). Similar to porcine stroma, it is made up mainly of type I collagen (Birk *et al.*, 1986), with keratocytes that are interspersed between the fibrils that are regularly packed within the lamella . This allows minimal light scattering to less than 1 % (Jalbert & Stapleton, 2005),

significantly improving visual function. An epithelial layer is also needed to prevent change of water content after transplantation. Overall, corneal constitution is relatively simple, but poses a huge challenge in the preservation of light passage.

6.1.3 Issues related to transparency

Transparency is the most essential characteristic of the cornea, and several papers have discussed the issue of corneal transparency (Benedek, 1971, Farrell *et al.*, 1973, Hassell & Birk, 2010, Qazi *et al.*, 2010). Traditionally, disorder of corneal transparency was explained by a combination of three main factors: (1) abnormal water content; (2) abnormal collagen fiber diameter, spacing, and orientation; and (3) abnormal accumulation of macromolecules (Møller-Pedersen, 2004). Later, biophysical models of corneal transparency have entirely focused on the stromal extracellular matrix and disruption of the parallel collagen array (resulting in loss of local collagen density) as the main reason for haze perception, as previously suggested (Maurice, 1957, Freegard, 1997, Clark, 2004). Modelling of corneal transparency requires quantifiable data for stromal collagen, which is not available from current methods. A quantitative evaluation of transparency may have potential in predicting a full recovery of transparency after rehydration and re-cellularization. Theories about how corneas become transparent have been proposed from physical (Benedek, 1971, Freegard, 1997, Smith, 2007, Casadessus *et al.*, 2011), cellular (Jester, 2008), and molecular (Hassell & Birk, 2010, Qazi *et al.*, 2010) angles. Most mathematical theories are based on the assumption that a transmission light source is in use, mainly because it directly explains how visual perception initiates on retina. When considering its light passage, scattering, which leads to reduction of light received at the retina, can occur either at the surface or

inside the cornea like other optical devices. Most researchers, however, agree that the order of the collagen matrix in stroma is the major contributor to corneal transparency, leading to extremely limited light scattering. Hence, level of transparency may serve as an indicator of whether such a scaffold has undergone significant changes in stromal structure. The artificial graft should be evaluated where a technician can assess its transparency quality in an objective and graded manner prior to corneal transplantation. Nevertheless, currently there is no reliable method to establish the structure-function relationships; theoretical design and structural characterization of the corneal scaffold have therefore been hindered by the lack of such a tool.

6.1.4 Multiphoton microscopy (MPM) of cornea

Multiphoton microscopy (MPM) may be used as a novel method in analysing cell-substrate interaction and structure-function relationship in cornea. At present, there are several techniques that have been used extensively on corneal assessment, including ultrasound pachymetry, confocal microscopy, very-high-frequency digital ultrasound biomicroscopy, optical coherence tomography, and slit-scanning elevation topography (Rio-Cristobal & Martin, 2014). However, most of these techniques focus on getting global physical data (e.g. thickness, curvature, intraocular pressure, etc.), and there is a lack of microstructure analysis of the stromal collagen, which may lead to correlation to optical functions of the corneal scaffold (Meek, 2009). The visualization mechanism of MPM may utilize SHG signals coming from non-centrosymmeric molecules such as collagen in the scaffold. (Zhou *et al.*, 2013, Lai & Tang, 2014). MPM has been used for the analysis of vision. Its variation, two-photon microscopy, was used in the visualization of mouse eye, including corneal epithelium, sclera, and retina, with respect

to different excitation wavelengths being used (Imanishi *et al.*, 2007). MPM is particularly effective for studying the SHG from type I collagen fibrils, radiating from the shell rather than from the bulk (Cox *et al.*, 2003, Williams *et al.*, 2005). This makes it a desirable tool for analysing the corneal stroma. A combined two-photon/SHG microscope could be used to analyse subtle modifications in the collagen assembly's tertiary structure and interfibrillar alignment due to thermally-induced damage (Matteini *et al.*, 2009, Matteini *et al.*, 2012). Lastly, MPM imaging also has the advantages of being non-invasive, non-destructive, and sterile when it comes to sample handling. The recorded images are three-dimensional and multi-channel, with exceptionally high signal-to-noise ratio and reduced photobleaching. These render MPM useful for the analysis of the decellularized corneal stroma.

6.1.5 Image processing and its potential use with MPM

Image processing tools may serve as a new method to MPM analyses of corneal scaffold by transforming the SHG signals into quantifiable data. Several papers have been published on using image processing to look into the biofilm formation (Yang *et al.*, 2000, Xavier *et al.*, 2001, Yang *et al.*, 2001b, Baveye, 2002, Beyenal *et al.*, 2004, Yerly *et al.*, 2007) Biofilms are polymeric matrix containing colonies of micro-organisms; their structures may confer high tolerance to antimicrobial agents and biocides. As a result, researchers have been focusing on characterizing biofilm structural features in a quantitative manner. It is common to use confocal laser scanning microscopy (CLSM) on the study of biofilm; CLSM is similar to MPM in that it is non-invasive, non-destructive, and multi-channel. Tools such as deconvolution and isosurface have contributed by providing strong contrast to identifying edges of biofilm.

It can also be used in determining viability inside of bacterial biofilms. There is, however, a continuous debate over the proper processing controls and enhancement over the signal-to-noise (SNR) ratio for a reliable threshold between different features. Selection of methods should comply with the nature of the biological sample and manufacturing processes that have been applied to such a sample in order to achieve the optimal output.

Making proper constraints on the image acquisition is crucial for turning MPM imaging from qualitative into quantitative data. Cox *et al.* (2003) discussed how the point-spread-function (PSF) of SHG might be controlled. This is important because without good control over PSF, the image would be too blurry to be quantified, especially in a case where a full 3D AFS is visualized, where strong absorption and background noises would be expected. Fortunately, excitation wavelength about 800 nm has been proven to have the highest transmission through the cornea around the visible wavelength (Freegard, 1997). This therefore places MPM in a better position compared to CLSM, which utilizes ultraviolet lights for characterization. A better transmission means that there would be less attenuation, therefore reducing the need of compensation processing and increasing the confidence in quantification. Another main advantage of an MPM is its inherent optical sectioning capability that eliminates out-of-focus signals by the nonlinear dependence on the illumination intensity at focal plane (Tal *et al.*, 2005). Although SHG and MPM have been used extensively for analyzing collagen scaffolds, currently there is a lack of proper method to analyze the surface texture of the scaffold. When it comes to the analysis of transparency of cornea, this becomes a problem in the current MPM approach. The main issue at hand is that considering the MPM images were taken into stacks, it is difficult to process several slices

simultaneously to deduce reliable surface descriptors. When analyzing the surface from stromal collagen, it is important to evaluate the thickness of collagen fibers, smoothness, orientation, and effect from extreme peaks or valleys. To answer this question, the Extended Depth of Field plug-in, which was previously developed for images from the transmission light microscope, may provide a promising solution to the generation of a representative 2D height map. This allows image fusion that makes calculation of surface descriptors easier. Solving these issues may contribute to the need of quantitative analysis for tissue optimization and comparative research.

Therefore, it is interesting to see if SHG signals from collagen fibers, MPM, and image processing tools can be utilized together to illustrate structural changes in the stroma that may lead to changes in corneal transparency. In this chapter, a number of completely packed, dried 3D corneal scaffolds (n = 80) were evaluated for their potentials in generating functional recovery. Since this was an end-point, custom evaluation prior to transplantation, there lacked a standard method for testing the transparency function. A novel method that utilized a transparency meter was employed and further validated by the multiphoton analysis of the screened samples. It was necessary to provide measurements that were relevant to the clinical workflow and desired functional recovery. These corneal scaffolds (in their sealed condition) were directly tested for their Total Transmittance (%T, a physical and objective measurement for transparency) and Haze (%H, relevant to the patient's visual perception). Outlier samples were then investigated by MPM for their structural defects in order to provide a solid ground on how these extreme values in transparency were contributed to the microstructure of the aligned collagen fibrils (assuming that the decellularization process was complete). Interior parameters (e.g. local collagen density) and exterior

parameters (e.g. surface roughness, kurtosis, skewness) were be calculated for the correlation between scaffold structure and function. The result of this study should provide a convenient, non-destructive, and quantifiable evaluation for the end-point tissue engineered products that may be used in transplantation immediately.

6.2 Materials and methods

6.2.1 Scaffold preparation

Cornea scaffolds (n=80) were provided by China Bio-Med Regeneration Technology Limited (CBMRT™, Hong Kong, China). These scaffolds were created from cell-bleaching methods and standardized dissection so only part of the stromal section with the same thickness underneath the epithelial layer of the cornea was retrieved. The scaffolds were placed in a small plastic Petri dish, dried, and vacuum-sealed into a semi-transparent nylon-based plastic bag. The same packaging without a scaffold inside was used to provide a reference reading for the transparency meter.

6.2.2 Parameters to be characterized for functional study

According to Lai and Tang (2014), it is correct to assume that there will be no significant difference in refractive index in the 7 mm area scanned by the transparency meter. Also, pupil opening has a normal range of 2~9 mm in diameter (Winn *et al.*, 1994). With regard to these, it is important to record other structural and functional values for the region above the pupil, for it contributes directly to the patient's visual perception. Transparency parameters (e.g. Total Transmittance and Haze) would be recorded to provide functional references. Structural features of interest were shown in

Figure 6.1. The presence of remaining cells was checked by the raw MPM images. Any change in collagen density was evaluated by isosurface processing, which had a threshold set at the most distinguishable level for high and low local collagen density. The *number of broken surfaces* and the *volume ratio of the low-density region/total ROI volume* would be analyzed. The surface roughness values (e.g. roughness, skewness, and kurtosis) were also calculated.

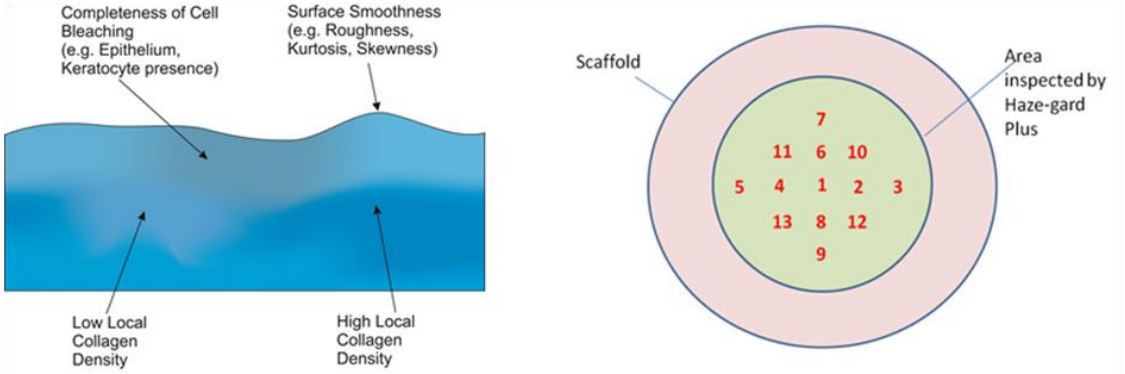

Figure 6.1: Parameters and positions to be evaluated by MPM. LEFT: Schematics of the parameters that may be related to transparency of the scaffold. Completeness of the cell removal, surface texture in terms of rms roughness, kurtosis, and skewness would be evaluated from the MPM images. Collagen fibrilar density was calculated using Isosurfaces at threshold that provided the strongest contrast. RIGHT: Locations and numbering of the fields of view recorded using MPM. In total they covered ~20 % of the total area tested by the transparency meter.

6.2.3 Transparency measurements

Transparency of individual scaffolds was initially assessed using Haze-gard Plus (BYK-Gardner, Germany). Percentages of Total Transmittance (%T) and Haze (%H) were recorded for later normalizations. The transmission haze here is defined as the percentage of light in passing through shows wide angle scattering deviating from the incident beam greater than 2.5 degrees on average (according to ASTM D 1003). A 7

mm adaptor was attached on the detector side to allow controlled collection of any incident beam passing through the central area of the scaffolds. The average reference values were subtracted from the experimental values. From this data, a group of functionally representative samples were selected for MPM mosaic scanning (i.e. either $p < 0.05$ for %T or %H, and the sample that had values closest to the normalized center of both readouts). They were analyzed to determine if some structural integrity issue could be related to the changes in Total Transmittance or Haze.

6.2.4 Multiphoton microscopy

Three-dimensional fluorescent images were obtained from a modified BioRad Radiance 2100 MP Multiphoton Microscope (Zeiss; Jena, Germany). Near infrared (NIR) laser beams (wavelength = 800 nm) were obtained from a tunable 76 MHz femtosecond pulsed Ti:sapphire laser (Mira 900-F, Coherent, Ely, U.K.) pumped by a 10 W multiline argon ion laser (Verdi; Coherent). A Nikon S Fluor 10X water-immersion objective with a numerical aperture of 0.30 was used for all images. The emission filters/channels selected were: 495 nm for blue, 525 nm for green, and 595 nm for red. For each scaffold, thirteen fields of view (0.785 µm x 0.785 µm each, in total roughly 20 % of the 7 mm area tested by the transparency meter, 1 mm from each field to another) were scanned for the investigation of cornea structure. 500 lps was used as the scanning speed for creating enough surface resolution. Z-step is 1.95 µm, and there are 512 x 512 pixels in each plane. All image files were taken in exactly the same way, with 310 sections, same laser power, and same gain/offset settings.

6.2.5 Image processing

The computer spec was described in Section 4.2.9. The raw files first underwent 3D blind deconvolution treatment using AutoQuant X3, then were reconstructed with the isosurface object of Imaris 7.6.1 according to the signal intensity from collagen (shown in the blue channel by its second harmonic generation). This allowed a direct observation of the interior structure of the scaffolds. Two isosurfaces were created for each image. The blue isosurface presents outer surface morphology of the scaffold. The red isosurface [with signal threshold selected automatically according to Ridler and Calvard (1978)] calculated the cubic region of interest (ROI) volume right underneath the surface. The volume ratio of the red isosurface to the ROI that contained it could reveal whether there are significantly denser/looser collagen bundles. This method not only provided visual contrast, but also could quantify the level of compactness for samples showing significant optical functions.

Deconvolved files were also analyzed using Fiji (Schindelin *et al.*, 2012) and two plugins—Extended Depth of Field (Forster *et al.*, 2004) and SurfCharJ (Chinga *et al.*, 2003, Chinga *et al.*, 2007). Several surface descriptors [e.g. root-mean-square roughness (R_q), kurtosis (R_{ku}), skewness (R_{sk})] may be characterized to provide explanations to functional observations. The images were first rearranged using the Easy Mode of Extended Depth of Field; afterwards, the height-maps were used to calculate the surface parameters using the default SurfCharJ setting.

6.2.6 Statistics

All the values were reported in mean ± sample standard deviation (SD) manner (n = 13 for each group as depicted in Figure 6.1). One-way ANOVA was performed

with multiple comparisons against the Normal Center sample for significant findings ($p < 0.05$).

6.3 Results

6.3.1 Results from the transparency meter

The Total Transmittance and Haze values were first assessed to reveal samples of interest. After recording over 80 processed scaffolds and subtracting the average background, the average experimental %T was -2.16 ± 1.69 SD, and %H was 15.29 ± 3.89 SD. Histograms for their distribution are shown in Figure 6.2. Non-linear regression shows that the data fit well with the Gaussian curve (R^2 are 0.7984 for Total Transmittance and 0.9452 for Haze), indicating that there existed a normalized population, with reasonable convergences for both Total Transmittance and Haze. The Gaussian curve for %T had a mean of -2.66 ± 1.63 SD; for %H it was 14.77 ± 2.74 SD. From these histograms, a number of samples were selected for MPM structural analysis. Some of these samples—LowT, HighT, LowH, and HighH—were selected because either their %T or their %H was outside of the 95 % normal distribution. As a comparison, a sample (named Normal Center) that was closest to the middle of both normalized mean of %T and %H is selected to reflect the optical properties and structural composition of the majority of the group. Values of these five samples were summarized in Table 6.1. LowT sample, despite having the lowest Total Transmittance, had a Haze value close to the Normal Center sample. Considering the definitions of Total Transmittance and Haze provided by Haze-gard Plus, it is likely that for this

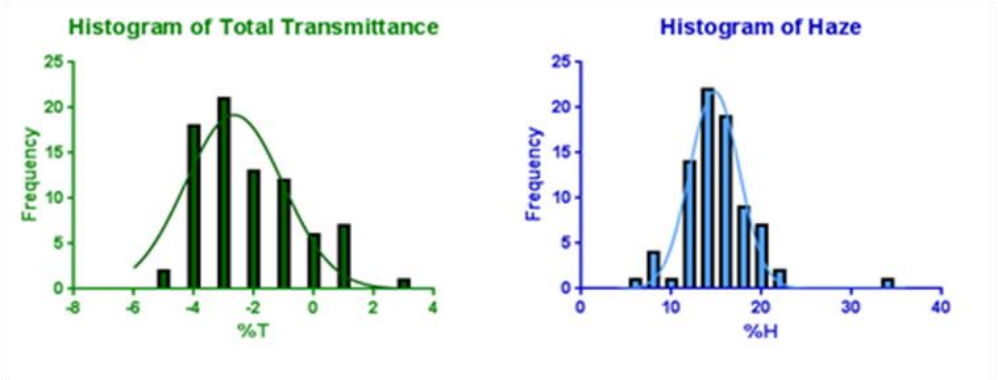

Figure 6.2: Histograms of Total Transmittance (%T) and Haze (%H) by Haze-gard Plus. A Gaussian curve was fit onto them to see whether this group of samples show normal distribution. Samples with extreme values were later selected for structural analysis. n = 80 for either %T or %H.

	Total Transmittance (%T)	Haze (%H)
Sample ID	Average	Average
LowT	-5.32	14.19
HighT	2.89	8.99
LowH	-2.72	5.39
HighH	-0.91	34.09
Normal Center	-2.52	14.59

Table 6.1: Samples that displayed extreme values in either Total Transmittance (%T) or Haze (%H). Values were the averages taken from the 13 fields in Figure 6.1.

sample, a huge portion of light was absorbed internally, but the through light rays did not deviate too much. The HighH sample was the opposite in that it allowed more light rays to pass through, but most rays were refracted in wide angles. HighT and LowH samples both had rather low %H, but LowH had a %T closer to the Normal Center. Structural analyses then needed to be investigated for the slight differences.

6.3.2 MPM imaging of the packed scaffolds after deconvolution

MPM images were taken at the thirteen locations previously described in Figure 6.1. A representative image from location 1 of the Normal Center is shown in Figure 6.3.

All samples were found to have clear SHG signals from collagen only. No remaining cell presence was found, as there was no green SHG signal specific to cells was

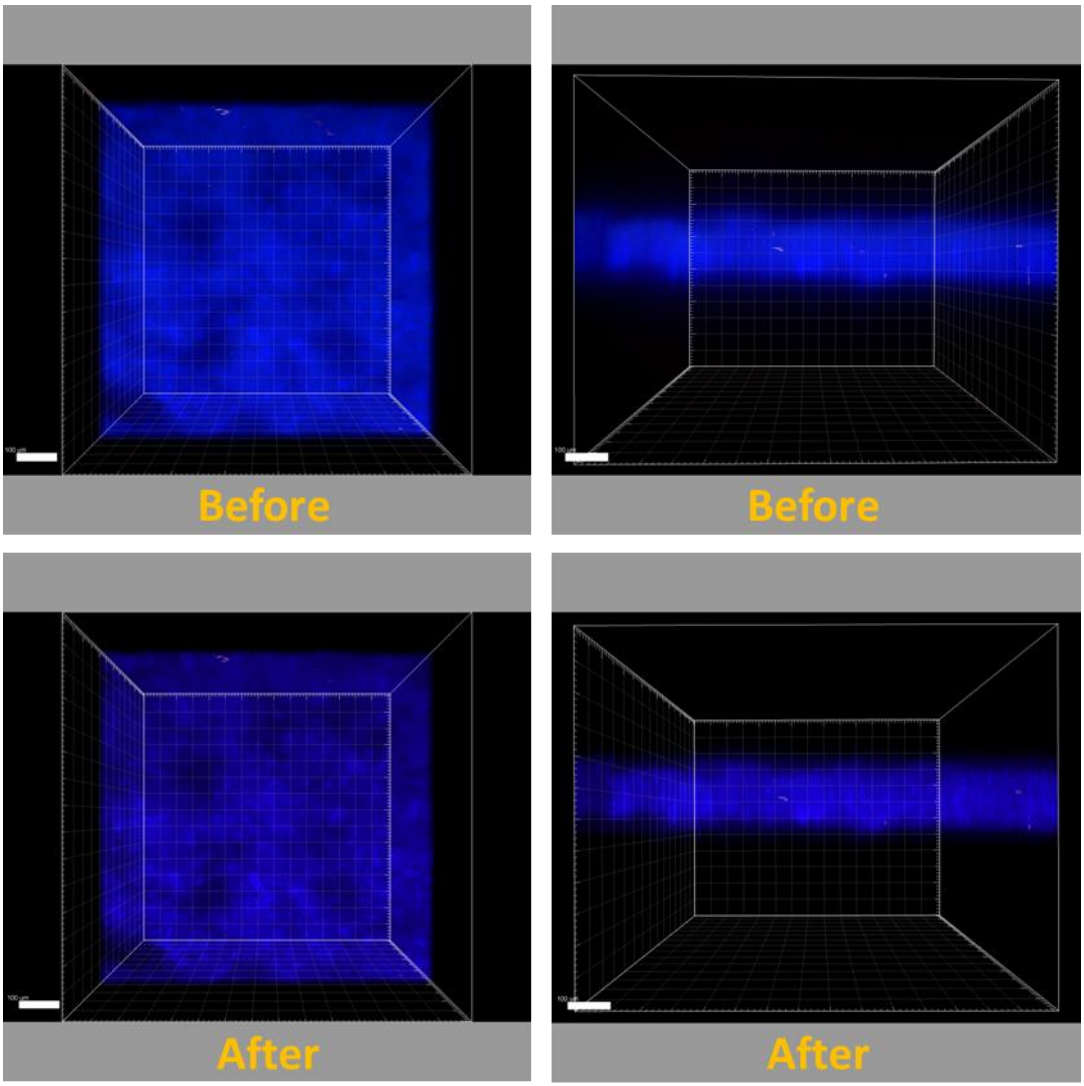

Figure 6.3: 3D SHG signals from the Normal Center sample (location 1). The image is representative of the acquisition of the images taken from the five samples, observed from the XY- and XZ sides. TOP: acquired image before deconvolution. BOTTOM: same image after blind deconvolution. Scale bar = 150 µm, major tickmark = 50 µm.

collected as described by Zoumi *et al.* (2002). All image files were taken with the same voxel definition, with intentionally left empty space for better image processing. From the image files it was observed that aside from the collagen signal (presented in blue channel), there was no cell presence in other channels, suggesting that the cell bleaching

process was complete and the stroma samples could be treated as aligned collagen fibers. Considering the simplicity of the cell-depleted cornea scaffold, which was made from part of the stromal region of the porcine cornea, the main difference in Total Transmittance and Haze came directly from the distribution of collagen.

6.3.3 Isosurfaces of the outer surface and internal structure

Next, two isosurfaces were built for all thirteen locations of the five samples, as shown in Figure 6.4. The blue isosurface gave a visual representation of the outer surface of the scaffold. It illustrated the boundaries of the scaffold for signal processing and showed whether the scaffold remained integrated. The red isosurface represented the internal structure. It was built with a cubic region of interest (ROI) volume between the boundaries and constructed with an automatically selected threshold. This arrangement allowed the two isosurfaces to be calculated using two different noise levels—one that was merely from air and the other from the inside of the scaffold. Coincidentally, all red isosurfaces had the automated threshold set at 15.3663, indicating that the images were taken with strict sample preparation and noise control. From Figure 6.4 it could be shown that such setting was able to distinguish internal structural differences amongst the five samples. As a reference, the Normal Center sample showed uniformly distributed and compact collagen fibrils. It did not have apparent holes, nor does it have loosened collagen bundles. LowT sample, on the other hand, seemed to have a large amount of low-density collagen regions, which may be inferred to as the *lakes* as mentioned in the article by Benedek (1971). LowT was also showing thousands of small broken surfaces, suggesting that the collagen

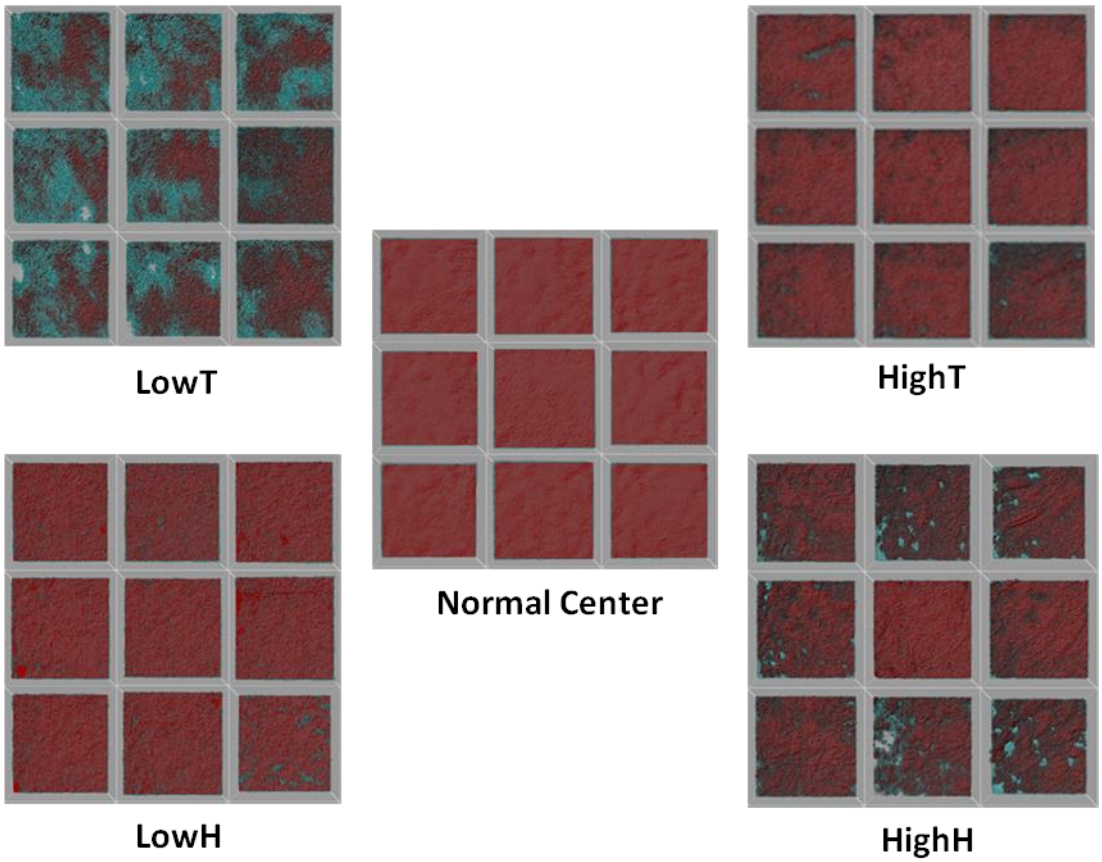

Figure 6.4: Isosurface reconstruction of the density of the interior collagen fibrils. The blue isosurfaces were semi-transparent for easier observation of the outer surface and integrity of the scaffold. Red isosurfaces were cubic volumes underneath the surface and were representative of areas that had a denser fibrillary collagen population. Threshold was selected by an automatic iterative bimodal method. Locations 1, 2, 4, 6, 8, 10, 11, 12, 13 from Figure 6.1 were selected here for easier comparison.

bundles were loosened in a global manner. In comparison, the HighT sample, though showing denser internal collagen, still had a few lakes distributed at all locations. The LowH sample was the closest to the Normal Center, though its fibrils were less compact compared to that as well. The HighH sample apparently had local differences in the lake presence and number of broken surfaces. In that regard it is similar to the LowT sample.

The isosurfaces were not only able to provide a strong contrast to visually observe the structural differences; it also allowed data to be quantified for statistical

analysis. Figure 6.5 is the statistical evaluation of the significance of broken surfaces and lake presence. It is shown that in terms of the number of small broken surfaces, LowT sample was significantly higher in the number compared to all the other groups ($p < 0.0001$). Together with Figure 6.4, this indicates that the loosening event took place globally throughout this sample, creating differences in local density (therefore

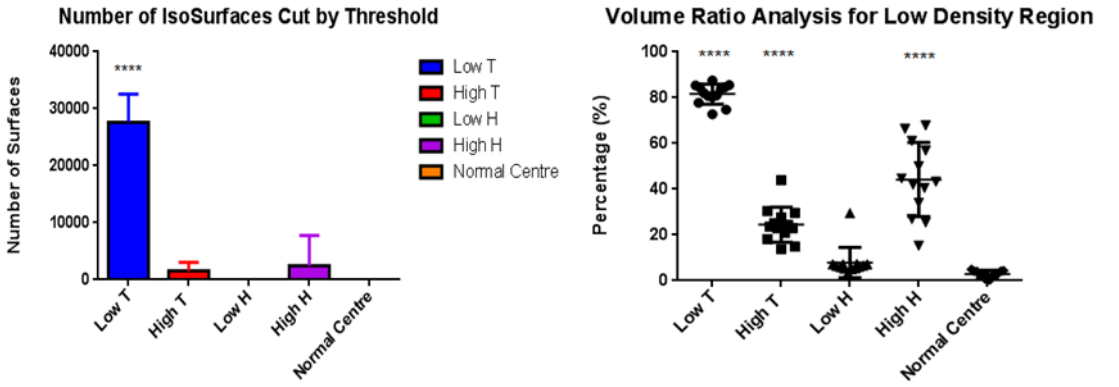

Figure 6.5: Surface analysis of various samples showing differences in transparency. LEFT: It is shown that the total number of surfaces broken by the selected signal threshold may influence the Total Transmittance directly. RIGHT: When compared to the Normal Center, the other four samples show a variety of differences in the volume ratio study. n = 13 for each group.

differences in internal refraction and loss of transmitted light). Volume ratio of the sum of all surfaces over the cubic ROI volume used for isosurface analysis show that LowT, HighT, and HighH were all significantly different from the Normal Center ($p < 0.0001$), but in different ways. LowT and HighT both showed globally loosening effect, but LowT loosening occurred at a much larger scale (e.g. on average 81.62 ± 4.38 % of its collagen bundles had reduced density) whereas HighT showed a smaller scale (e.g. about 24.52 ± 7.73 % only, still significantly higher than the Normal Center). The loosening effect in HighH was still significantly different, but the effect varies from point to point, as echoed in the observation in Figure 6.4. It averaged at 44.19 ± 16.18 %,

showing a much wider variance. The averages of the LowH (7.92 ± 6.60 %) and the Normal Center (3.23 ± 1.87 %) seemed to be close, suggesting that there was not much change in its collagen density. In short, global reduction of collagen density throughout the scaffold could result in either an increase in %T or a decrease in %T, depending on the degree of scaffold integrity, when interpreted as the number of broken surfaces. The higher the number of broken surfaces, the more likely the loss of transmitted light. Regional reduction in volume ratio, on the other hand, made the local refraction highly variable, producing more astray lights passing through, interpreted as increase in blurry perception (i.e. increase in %H). A corneal scaffold with higher collagen density would likely to have proper visual perception.

6.3.4 Evaluation of surface texture

The two transparency parameters may also be influenced by the surface texture of the scaffold. Figure 6.6 shows the related characterization for surface smoothness. From Figure 6.6A it can be shown from the root mean squared (rms) roughness that LowT and HighH had wider changes in surface elevation, whereas HighT, LowH showed a similar surface profile to that of the Normal Center. The rms roughness in Figure 6.6A can only suggest that surface roughness may be one factor that affects light passage. But in Figure 6.6B, skewness for the HighT, LowH, and Normal Centre all had negative values, whereas LowT and HighH, the samples that prevented proper light passage throughout the scaffold, started to show positive skewness. This shift means that skewness might be a real parameter for determining transparency properties. As the skewness becomes more positive, it may impede the light from staying in its

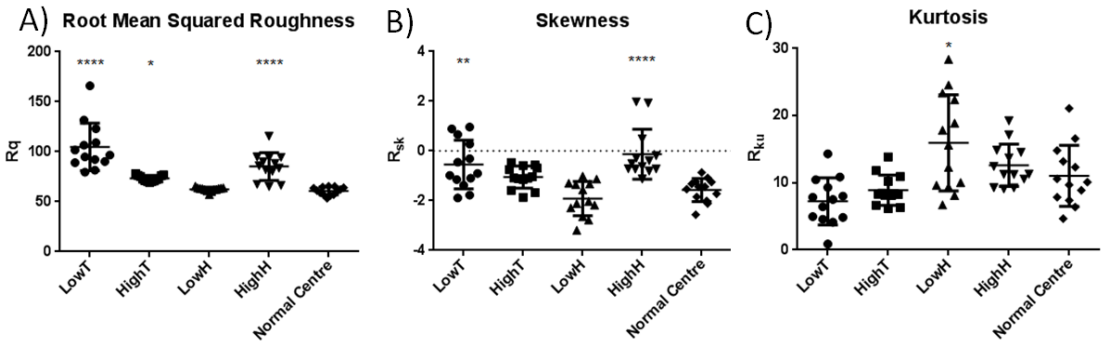

Figure 6.6: Surface parameters of the samples. Judging from how light passes through the cornea, it is possible that the first contact at the anterior surface can make a difference in transparency. A) rms roughness values of LowT and HighH show that the overall surface roughness can directly impede the light passing through properly. B) Further analyses on the skewness indicate that LowT and HighH started to show positive skewness partially. C) Kurtosis analysis show that the LowH sample differed from other samples in that it had a high variance in the local peak presence ($p < 0.05$), suggesting that the wide variance may actually reduce refraction angles overall. n = 13 for each group.

course, therefore reducing the amount of light collected at the receiving end. Figure 6.6C investigates whether the rms roughness values were contributed by kurtosis, the effect from extreme peak values. It shows that LowH, while being not significant in the rms roughness analysis, had a high variance in the kurtosis values recorded at different locations ($p < 0.05$).

6.4 Discussion

6.4.1 Overall discussion of observed structure-function relationship

Although LowT and HighH samples seemed to have similar smoothness values in R_q and R_{sk}, they ended up having different optical functions. As a result, it became important to evaluate their performances based on the internal collagen analyses. LowT had a much reduced collagen density globally and a higher number of broken surfaces,

whereas HighH had a huge variance in collagen density but showed only a small amount of broken surfaces. This means that the major reason for losing light in the cornea scaffold is that the scaffold had a much loosened and broken structure globally, which increased internal reflection significantly. This may be translated into a severe level of losing the inherent lamellae structure. On the other hand, the increase in local variance of collagen density may permit more light to pass through, but with a widely refracted angle that causes hazy perception. Although surface roughness contributes to the decrement of light passing through, the main reason for bad vision still come from the internal collagen structure.

When comparing LowT and HighT, it is interesting to see that a slight loss of dense collagen allows more light transmission, whereas a huge loss of dense collagen worked in the opposite way preventing the passage. The number of surface analyses explained this by showing the major difference between the two was the presence of small broken surfaces inside the stroma. Therefore, it is likely that this number of broken surfaces could be related to the amount of light that is transmitted. With further quantification, it might be possible to find an optimal number for broken surfaces where a higher amount of light can be permitted without too much sacrifice in terms of haze.

The HighT and LowH samples were similar in many ways. On the inside both had a low number of broken surfaces. On the outside the two samples were similar in rms roughness and skewness. The slight difference here was kurtosis, where the LowH sample showed a wide spread of R_{ku} values at different regions but the HighT remained converged. Also, the volume ratio analysis shows that the HighT was significantly different from the Normal Centre whereas the LowH was not. Joined together, they indicated that the wider spread of peaks on the outer surface might help the LowH

sample to maintain its collagen density. And although LowH was similar to the Normal Center in many ways, it had a much lower %H recorded. Therefore, from a surface modification point of view, a higher variance in kurtosis on the outer surface may help reduce the hazy perception, while keeping the collagen structure intact inside.

In short, if the ideal cornea should be high in Total Transmittance but low in Haze, there may be an optimal volume ratio for the global collagen density inside stroma and a wider variance in kurtosis on its surface.

6.4.2 Issues related to deconvolution

Deconvolution significantly helped to distinguish SHG signals from different collagen fibrils, leading to better analyses on the internal and surface structures. Although 3D resolution of MPM is much improved by the control of the mode-lock laser, it still contains severe anisotropy caused by PSF that requires further image reconstruction. Deconvolution is a procedure that has preceded the introduction of biological confocal microscopes (Agard *et al.*, 1989). It provides better images by first fitting a curve to the noisy data points, then dividing the image transform point-by-point by the optical transfer function, eventually remove blurry point-spread-functions. It has been recommended by Shaw (2006) that deconvolution is in general helpful, or even necessary, for the acquisition of best resolution on 3D structures. Blind deconvolution is used on the assumption that the impulse response of the system is unknown and it assumes a Poisson random-point-process model for photon detection (Holmes, 1992). In this chapter it was found that without deconvolution, the background fluorescence from the stroma, with collagen fibrils fully occupying the space, would be too strong for broken surface analysis, rendering it statistically insignificant by having too many small

surfaces previously regarded as noise. This apparently would also hinder the analysis for potential keratocyte migration into the stroma in the future study of the cornea scaffold. Hence, the deconvolution process is essential in improving the quantification of the cornea scaffold.

6.4.3 Issues relating to thresholding

When reconstructing the internal collagen isosurfaces for the analysis of lower density regions, selection of a cutoff signal threshold became the most challenging issue. In order to be most effective on isosurface generation, the whole imaging process has to be as automatic as possible in order to reduce human errors or ambient noise. With this in mind, the experiments were designed by comparing data with the semi-automatic transparency meter. The only human effort involved was to load the sample in front of the detector properly, whereas other potential errors were reduced by the design of the machine. This avoids the use of panel experts, which many researchers see as a source of bias (Baveye, 2002). The blind deconvolution is also an automatic process as discussed above. Thresholding for isosurface, however, presents the greatest challenge for automation and requires the images to be taken carefully. In order to facilitate this, all the MPM images were taken in exactly the same manner, with the same laser power, gain, offset, sectioning, pixels, and translational Z-steps. Ample dark space (> 50 % of the total imaged volume) was left for better deconvolution. It was also pre-determined that an automatic thresholding method should be used to ensure valid statistics.

In that regard, the iterative thresholding method proposed by Ridler and Calvard (1978) was employed for its bimodal natural and simple algorithm. Although several thresholding or segmentation methods are available (Xavier *et al.*, 2001, Yang *et al.*,

2001b, Yerly *et al.*, 2007), the candidate became clear after initial imaging, which revealed that these scaffolds did not have cell debris or other unbleached components. Considering the fact that the only source of signal that remained in this scaffold was the SHG from collagen, it was speculated that the bimodal method may be useful for the simplicity of material. Although the scaffold could be compared to a highly dense collagen gel that has limited transition in the gray-scale of SHG, the clear dark space and the fact that keratocytes were fully removed indicate that there is a potential that such gray-scale may actually present a bimodal histogram. They may potentially transform the seemly unimodal histogram, which showed an inadequate separation of the collagen fibrils and the interstitial spaces in stroma. It was eventually proved by the observation that the automatically selected cutoff intensity value for all internal isosurfaces was 15.3663, despite the fact that global collagen density profile varies from sample to sample. This illustrates that after considering the biological and material processing of the corneal scaffold, a proper threshold can be drawn for the construction of isosurfaces, making them reliable for quantification analysis.

6.4.4 Issues related to surface analysis

During the investigation, it was found that the Extended Depth-of-Field module developed by Forster *et al.* could be used to analyze MPM data. The ImageJ plug-in was used to create the height map for surface characterization (Forster *et al.*, 2004). Although it was not recommended in the original paper to apply this plug-in to reflective and transparent specimen, it seemed to be effective in this study. One of the reasons is that in MPM imaging, only the Z-plane that was excited by the mode-lock laser at that time would be recorded. Therefore, the in-focus point for each Z-position

was quite unique, as required by this software. The other main reason is that the image signals were originated from the SHG of the scaffold rather than the transmission/reflection of light. This reduced issues such as diffraction or attenuation that would create false height map. In order to optimize the results, the translation step in this thesis was much smaller than the real DOF estimated from the stats of the objective, and the specimen was recorded thoroughly. As a result, the height maps were able to reveal slight changes in surface altitude, giving statistically significant data consequently.

While using SurfCharJ, the surface descriptors that were calculated from the height map could be used to explain outcomes from the contacts with light. When comparing the R_q data of LowT and HighH with that of the other three samples in Figure 6.6, it is shown that samples with significantly reduced light passage could be filtered out by surface analysis. Their singular light obstruction property is also reflected in Figure 6.5, where both show a higher percentage of low density regions compared to the average. These results indicated that SurfCharJ works effectively in evaluating the surface parameters, and it may be used to analyze transparency properly in this case.

6.4.5 Contribution to the field

In this chapter, a novel screening method using a transparency meter was developed for the end-point, completely sealed, sterile, and quantitative evaluation of the cornea AFS deemed ready for transplantation. Due to these special conditions, existing standard method for cornea evaluation (such as pachymetry for corneal thickness) was not useful. Ultrasonic approaches might be able to calculate the scaffold thickness, but do not have enough image resolution for microstructural analysis and are

irrelevant to the determination of transparency. Confocal laser scanning microscopy (CLSM) that relies on UV light was unable to penetrate the plastic package. Hence, the transparency meter, which utilizes a transmission white light for transparency determination, was one of the few remaining options for sample screening. However, there lacked a standard, controlled method for the transparency meter to be compared with. It is therefore necessary to validate the transparency results with another method that can establish the theoretical background for data analysis. Fortunately, the scaffolds were simple in material and structure and were fully decellularized. This made it possible to use the infrared laser in MPM for 3D SHG analysis of the arrangement of the collagen fibrils. From the interior and exterior analyses of the collagen signals, the MPM results were able to suggest a correlation between the 3D fibrillar arrangement and the transparency functions (%T and %H). This discovery backed the use of the transparency meter on the end-point analysis of processed corneal scaffolds, providing a possible indicator for the readiness of the tested scaffold for transplantation.

In terms of tissue characterization, the MPM image processing method itself can be an invaluable tool to study tissue maturation. Firstly, the sample can remain vacuum sealed and sterilized after characterization for the outer surface and the internal structure. This reduces batch variances, and allows direct observation of post-seeding cell-substrate interaction of samples that have been previously characterized. It not only reduces the manufacturing cost of the scaffold, but also simplifies the cell seeding process for more reliable tissue assessment. An understanding of the lamellae arrangement can help researchers evaluate how keratocytes will migrate into the interior of the scaffold, which will eventually lead to recovery of normal corneal functions such as transparency and wound healing. Surface texture characterization, on the other hand,

might influence how the epithelial cells attach and migrate on the scaffold (Atsuta *et al.*, 2014). Cell migration rate with respect to varying levels of surface roughness can be evaluated using time-lapse MPM. Due to the material simplicity of this scaffold, it might also be possible to correlate SHG signal intensity with some mechanical properties. Therefore, this quantification tool can directly engage in some of the most important cell biology issues regarding corneal tissue maturation.

For the transparency study, isosurface analysis for the internal collagen density is important because the degree of loosening is a quantifiable indicator of how lamellae have been rearranged. Surface analysis of corneal scaffold also contributes to the understanding of light scattering. Together with visual perception studies conducted using a single-pass transmission light source (De Brouwere *et al.*, 2008), they may provide a useful tool for mathematical modelling and design of corneal scaffolds. MPM image processing can also contribute to the modelling of corneal transparency from the cellular and molecular angles. The multi-channel recording allows direct observation of keratocytes, which have a compact cell body and crystalline proteins in their cytoplasm that may reduce light scattering (Jester, 2008). During embryonic development, keratoblasts invasion and differentiation into keratocytes are important in replacing the hyaluronan rich ECM with a collagen fibril/proteoglycan rich ECM, turning the stroma transparent. Considering the thickness of the tissue, MPM may be the best method for studying this cell-substrate interaction. Direct 3D observation is also needed for the study of stratification of keratocytes, which depends on the assembly of collagen fibrils and deposition in the matrix. The epithelium and endothelium maintain corneal transparency by serving as a mechanical barrier to fluid diffusion and by creating a gradient that enables osmotic transport of water out of the stroma (Edelhauser, 2006).

Using appropriate staining and multi-channel recording, it is possible to not only observe the adhesion/migration/proliferation of these cells, but also quantify the transportation of water *in situ*. From the molecular point of view, proteoglycans determine the architecture of the corneal matrix and its water-retaining properties by interacting with collagen fibrils (Borcherding *et al.*, 1975). It is proposed that the reason $Lum^{-/-}$ mice develop corneal haze and abnormally thick collagen fibers in the posterior corneal stroma may be due to abnormal fibril assembly, lateral fusion of fibrils due to an absent lumican protein core, and altered interfibrillar spacing (Iozzo, 1999, Chakravarti *et al.*, 2000). With this MPM tool, the changes in interfibrillar spacing can be quantified while varying the presence of proteoglycans. Lastly, the tool can also provide a way to evaluate the success of scaffold rehydration in terms of thickness changes and water retention, which is one of the main reasons for the loss of transparency post-surgery.

6.5 Summary

In this thesis a non-destructive, quantitative method for the analysis of a 3D AFS made from decellularized porcine cornea was proposed, which may lead to more understanding of the underlying principles of corneal transparency. This method combined MPM and several image processing tools for the analysis of the collagen fibrils in the stroma, which could be related to Total Transmittance and Haze that depicted the degree of transparency. The results show that there may be an optimal volume ratio for the global collagen density inside the stroma and a wider variance in kurtosis on its surface that will enable the design of a corneal scaffold with high light transmission and improved visual perception. The method utilized seems to have

achieved initial goals and may provide useful analyses in the rehydration process and tissue culture.

Chapter 7 **Conclusion and future work**

7.1 Conclusion

Three dimensional (3D) aligned fibrillar scaffolds (AFS) could be used to create some of the most complicated tissues, thus helping medical treatment progress toward a new era while presenting huge commercial potential. Such scaffolds would provide an alternative solution to current difficulties in functional recoveries in tissue/organ regeneration. One of the most prominent approaches is to employ electrospinning in the creation of continuous nanofibers that may mimic the ECM of the targeted tissue. This method has received huge attention in recent years, showing a promising future for the realization of transplantation with artificial scaffolds. Nevertheless, there are several difficulties that need to be overcome before the 3D AFS products pass regulatory and quality assessments prior to transplantation. One of the major challenges is that there lacks a perfect control over the alignment of electrospun fibers, so the proper selection of existing alignment methods becomes crucial for cell culture and function generation. The other major challenge mainly originates from ineffective and destructive scaffold/tissue characterization processes, which collectively impede the progress of tissue engineering as a viable option before transplantation. This thesis, therefore, attempted to investigate the challenges involved in fabrication and characterization, thereby hoping to provide guidance in effective AFS design for functional recovery and to see if there exists a certain characterization method that could reduce the cost, time, batch variance, and technical difficulties while enhancing precision of measurements, quality of product, and convenience toward transplantation.

For the fabrication of 3D AFS, it was hypothesized that aligned nanofibers would allow aligned cell growth, which would lead to the recovery of needed functions as the tissue matures. The investigation started with a literature research of available materials that may be modified for agent release and cell adhesion. A prototypic AFS material that was made from polycaprolactone (PCL) and gelatin was therefore created. This prototype was then moderately aligned by two fundamental alignment methods (i.e. parallel metal strips=PS and rotating drum=RD) and was characterized for fiber diameter, stiffness, and degree of alignment. Finally, the PS and RD fibers were directly compared for their effects on SH-SY5Y neurite extension, which would provide guidance for the proper selection of alignment methods to be used in the development of functional nerve guidance conduits (NGCs).

For the novel characterization method, a reverse thinking strategy was developed on the grand assumption that there may be a characterization method that can non-destructively provide necessary information with regard to the conditions of both the AFS scaffold and its cultured tissue all the way from scaffold fabrication to transplantation. Such a strategy would need to attain several conditions: (1) The characterization method has to be non-invasive and non-destructive for 3D deep tissue samples, so the same sample can be monitored at every step throughout the process. (2) This method would need to provide the necessary information in a quantitative manner, so the results could be assessed statistically. (3) This method had to be able to acquire not only cell/tissue information, but also the information regarding scaffold properties. This thesis then explored the existing literature in Chapter 2 related to these three conditions. Condition (1) significantly limits the available methods for characterization. An optical method was therefore preferred since such an electromagnetic wave is in

general not harmful to most materials while penetrating. In response to condition (2), the method would likely rely on light or fluorescent microscopy, which gives qualitative real-time visuals of the cell culture (thus may potentially provide the most information). But it may require image processing works to transform these images into quantitative data. In conjunction with condition (1), for deep 3D tissue to be visualized, it was then discovered that MPM would seem to be the most reasonable approach for such a complicated task. Lastly, if such a method had to acquire scaffold information as well, then the scaffold would need to react with the MPM laser. It was later found that SHG-capable materials might be able to provide enough signals to fulfil this wish. Hence, the schematic design of this new strategy was formed, with SHG signal control, non-invasive MPM imaging, and quantitative image processing as the key components to be investigated. The best way to illustrate the usefulness of such a strategy was through the earlier proof-of-concept AFS.

Through this study, the following conclusions are derived:

1. The parallel metal strips (PS) method is more likely to create AFS with better alignment that may benefit guided neurite outgrowth than the rotating drum (RD) approach
2. 3D MPM imaging that utilized both SHG and TPEF was proved to be powerful for quantitative analysis of AFS tissue characterization
3. Zero-order-like controlled release profile may be achieved while tuning the AFS material composition to be more amphiphilic, and electrospun fibers that were created from blended polymer solution showed a better release control
4. Collagen/gelatin would be a desirable material to be blended into AFS composition, for it may not only lower the hydrophobicity of the synthetic

material for better tissue culture but also provide SHG sources for high-precision scaffold analysis

5. A fluorescent technique such as MPM imaging is useful in that it induces and records signals that come directly from the scaffold structure; furthermore, the NIR laser used in MPM makes it possible to non-invasively acquire detailed information regarding deep tissue 3D microstructure
6. Existing image processing tools can not only enhance SNR control but also transform qualitative microscopic information into quantitative data for the analysis of statistical significance. This provides a novel method for the illustration of structure-function relationships for engineered tissues

Works in this thesis were able to prove that the quality of alignment of the nanofiber is the most important factor for an AFS to provide guided cell growth, and that the parallel metal strips (PS) collector design was more effective in creating highly aligned AFS. MPM imaging results in Chapters 4 and 5 indicated that the degree of alignment was directly involved in guided neurite extension. This showed that the aligned substrate did provide extra cues for the cultured cells to mature differently, and even slight changes in fiber alignment could cause a significant change in pseudopod developments when surface morphology and stiffness were kept at a similar level. Although there are many alignment methods developed for electrospun fibers, at present there is no direct experimental comparison that indicates which method would be more useful for the creation of nerve guidance conduits due to technical difficulties in controlling the electrospun fibers. Works in Chapter 4 narrowed down these choices to two fundamental methods and proved that the parallel metal strips (PS) method overtook the rotating drum (RD) method to be more effective in creating highly aligned

AFSs. Later neurite outgrowth experiments further demonstrated that the PS fibers allowed longer neurite development. This discovery illustrated an important fact linking fiber alignment to successful NGC design. It is possible that such a design may also come to benefit the cultures of other cell types, such as muscles or tendons.

Visualization of MPM played a crucial role in the analysis of the fine-controls over the orientation of electrospun fibers and proved that they were suitable for the induction of different cellular responses. 3D cell-substrate interaction is usually difficult to acquire. On the one hand, SHG signals from nanofibers, if there are any, are typically too weak to be distinguished from the background noise and may bleed into multiple channels, causing non-specific recording. On the other hand, it is also difficult to inspect cell morphology and penetration information in the Z-axis because it typically shows the lowest resolution. In this thesis, simultaneous recording of both scaffold SHG and cell TPEF signals were distinguishable after deconvolution treatment, and the precision in the measurement of neurite length was improved. The NeuriteTracer analysis from the 3D image slices successfully distinguished significant neurite outgrowth from different groups. This showed that the presented characterization method was able to generate a quantitative analysis over cell-substrate interaction despite the fact that these fibers were in the nano-scale and in a 3D environment. It may be interesting to use MPM to see how other modifications in AFS can cause different tissue culture results. As AFS remains a prominent research direction for artificial tissue, it seems to be promising to further explore the combined applications of both SHG and TPEF signals.

Changes in AFS material of choice would result in direct modification of important properties such as agent release and cell adhesion; and fabrication by

polymer-blending seemed to be an appropriate approach to satisfy both. Every year new electrospinning fabrication methods emerge at a rapid pace. Many of them aim to create fibers that are compartmentalized, porous, or emulsive for extra controls over agent release. From the study in Chapter 3, however, it was shown that agent release from electrospun fibers would likely be completed in less than one week. This was mainly due to the fact that the fiber was ultrafine enough for water to thoroughly diffuse into. Because the release profile is rapid and short, the simpler homogenous blending of the polymer materials seemed to create a fiber that may actually function in a more controlled manner. Modification in overall hydrophobicity may present an opportunity for the reduction of uncontrolled burst release and easier cell adhesion simultaneously; both are critical scaffold functions for tissue culture. It was therefore important for this thesis to further explore precise characterization of blended fibers, both for their structures and promised functions.

SHG signals from embedded gelatin/collagen proved to be strong enough for quantitative analysis of 3D AFS structure and porosity. Many biomaterials that may be used for AFS design are also capable of emitting SHG signals. In this thesis SHG-capable gelatin was blended with PCL to create the proof-of-concept fiber. Gelatin, which can be seen as degraded collagen, was selected also because it is inexpensive, relatively hydrophilic, commonly used in scaffold design, and may promote cell-adhesion. Works in Chapter 4 showed that the fabrication processes of PCL:Gelatin = 70:30 fiber and freeze-dried collagen scaffolds did not degrade the gelatin/collagen structures. Although porosity analysis of the PCL-Gelatin electrospun fiber was inconclusive, it was useful in Chapter 5 for the simultaneous recording of cell-substrate interaction and showed that fibers that were blended with gelatin displayed higher cell

viability in 3D culture. The SHG signal from collagen, however, has been proven to be quantifiable for both porosity measurement in Chapter 4 and the analysis of significant microstructural differences in porcine corneal scaffolds in Chapter 6. This presents a novel method for the characterization of a full 3D AFS. Utilization of the innate SHG signals presents a promising alternative that may yield precise void-space and scaffold structural information without some of the major drawbacks (e.g. destruction of the sample) presented in many current characterization methods.

MPM can be seen as the most resourceful characterization method for 3D tissue in terms of image quality, data quantification, signal penetration and non-invasiveness; it would be an important tool for academic research and industrial investigations alike. Image resolution at its best can distinguish 100 nm features, offering high SNR for each frame recorded. Multi-channel recording allows observation of targeted features individually, whether they come from the cells or the scaffold. Near infrared (NIR) laser provides deep tissue penetration without damaging the sample, and actually resets the constraints of penetration to the available laser power and the working distance of the objective. These advantages were clearly demonstrated in the experiments in Chapter 6. Due to high similarity of the vacuum-sealed corneal scaffold to the freeze-dried collagen scaffold visualized in Chapter 4, the isosurface objects were used once again for studying the microstructure of these dried corneas. From the literature it was known that the collagen fibers in corneal stroma are highly aligned in a 3D manner in order to contribute to lens transparency. Therefore, it was hypothesized that any disruption in the alignment would lead to not only the loss in transparency, but also the loosening of the collagenous network (reducing local collagen density to create more lake/void space). Although corneal stroma has been visualized by MPM in many reports (Jay *et al.*, 2008,

Bueno *et al.*, 2011), at present there is no quantitative analysis to illustrate this phenomenon. The works in this thesis showed that (1) the proposed non-invasive strategy was useful even if the scaffolds were already in complete package, and (2) that quantitative assessment of the relationship between the corneal microstructure and the level of transparency (in terms of Total Transmittance and Haze) may be achieved. The data suggested that there may be an optimal volume ratio for the global collagen density inside stroma and a wider variance in kurtosis on its surface that will enable the design of a corneal scaffold with high light transmission and improved visual perception. The proposed strategy was able to fully utilize the 3D SHG signals and conduct statistical analysis for both interior and exterior properties without damaging or contaminating the scaffold. Therefore, this characterization method successfully presented a quantitative method that may be further developed to meet the need for AFS tissue engineering. Such a method should not only be influential for academic research in 3D AFS tissue, but also for industrial investigation of sterile tissue products before their use in transplantation.

Image processing tools can reveal many hidden differences in the tissue when they work together with SHG imaging; this partnership may further enhance the usefulness of this characterization strategy primarily through the generation of quantifiable data. Several tools were applied to the 3D MPM images from Chapters 4 to 6, including blind deconvolution, automated thresholding, spot and isosurface objects, Fiji, NeuriteTracer, Extended Depth of Field and SurfCharJ. These available tools have made it readily possible to transform microscopic images into something that may be statistically meaningful. Traditionally, it would be difficult to analyse SHG signals. It was even more difficult in this study because the used MPM system could only collect

backward SHG, which is much weaker than the forward SHG considering their differences in emission profiles. The use of blind deconvolution, however, successfully eliminated excess signals and fixed them in a certain range in the Z-axis. This is a crucial step in tuning SHG into a reliable signal for almost all of the experiments done with MPM imaging. The use of spot and isosurface objects helped to illustrate the viability ratio, number, and morphological changes of the SH-SY5Y cells in the neural engineering works in Chapter 5. It was expected that time-lapse MPM could even reveal information regarding cell proliferation or migration. Automated thresholding is an important prerequisite of a fully automated characterization system, and the method used in Chapter 6 seemed to have taken a further step from Chapter 4 to render deep-tissue collagen SHG useful for micro-structural analysis. Utilizing the same image files, SurfCharJ turned the focus from the interior to the exterior of the corneal scaffold, and was able to draw on the relationship to the hazy perception in the eye. This proved that the 3D MPM hyperstacks contained rich information that may be used for tissue characterization, and the correct combination of existing image processing tools was able to reveal some that may be impossible to acquire using traditional MPM or other imaging methods. Research in the development of newer image processing tools, if taking microscopy techniques and sample preparation into consideration, may be able to create some newer characterization methods that can prove to be essential in the field of 3D tissue engineering.

In summary, the proof-of-concept fiber demonstrated that simplification of the tissue engineering process can be achieved if the following modifications are employed:

1. ESEM characterization on the properties of nanofibers
2. Use of SHG-capable materials to provide extra signals from the scaffold

3. MPM characterization for 3D deep tissue and non-invasive imaging
4. Use of image processing tools to quantify data for statistical analysis

This combination has taken into account the potential needs in agent release, alignment control, fiber characterization, and cell-substrate monitoring, which would be valuable as an affordable platform for researchers to conduct initial 3D tissue culture testing. Overall, works in this thesis have shown that with certain considerations and preparations, a highly applicable 3D AFS can be created with least effort in fabrication and characterization and can be carried on to complete the remaining tasks in product manufacturing and tissue regeneration. Modification along the same line of logic should be benefited from shorter research time, less capital spending, controlled batch variances, high efficiency in characterization/quality control, and good precision in quantitative measurement in completing the tissue engineering process.

7.2 Future work

Based on the outcome of this research and related progress in the field, the following works are suggested as possible continuation:

1. Develop the PCL-Gelatin fiber into an agent-eluting 3D scaffold that may serve as a platform for early-screening of 3D tissue culture
2. Design a micro-bioreactor to accommodate the PCL-Gelatin fiber for high throughput screening (HTS) needs
3. Utilize the alignment methods for engineering of complex 3D tissues
4. Improve imaging resolution in order to reduce the reliance on the invasive SEM characterization

5. Revisit the PSF of gelatin/collagen SHG and determine if there would be a better deconvolution method for fluorescence control
6. Develop the characterization strategy into a fully automated and standardized process

The PCL-Gelatin fiber that was produced during this investigation may provide a useful platform for agent release and 3D cell culture tests. One of the tasks that would help the project progress in this direction is to further optimize the PCL:Gelatin ratio and see which blended combination would give the best fiber in terms of controlled release and cell culture. With the easily prepared PCL-Gelatin fiber, parallel metal-strips collector, and extremely powerful MPM that is partnered with state-of-the-art image processing tools, it is reasonable that tissue engineering designs modified from this fiber may also gain several advantages from the proposed characterization strategy. For the construction of a highly versatile and robust platform, however, it would be desirable to have standardized results with respect to the agent release of various useful agents (e.g. NGF, BDNF, silver nanoparticles) and common cell types (e.g. mesenchymal stem cells, induced pluripotent stem cells) . A larger database would allow better comparison of data that can help researchers select the best fabrication method for agent release.

The proposed platform may be more useful if it were coupled to an established micro-bioreactor design to form a powerful 3D tissue-testing system. Some of the micro-bioreactor systems have been used in the literature with reliable results, such as the TissueFlex® perfused microbioreactor system [CN Bio Innovations Limited (CNBIO), U.K.] (Li *et al.*, 2013). This combination would create a useful HTS system for *in vitro* 3D artificial tissue testing, which utilizes only necessary materials to form a

piece of human tissue. Tissue engineering research that is done using this system may bypass the tremendous challenge that is involved in the design of artificial blood vessels, while maintaining high standards in 3D tissue culture using a well-controlled environment. Such a system may reduce the high cost and research time in HTS of tens of thousands of agents.

Another future direction would be to directly use the aligned fiber for complex 3D tissue designs. Slight differences exist between PS and RD fibers, which may imply that it would be wise to apply them to the manufacture of different tissues. For example, RD fibers show similar morphology to the fibers inside blood vessel wall and tendon. It might be a better alignment method for creating these tissues. This thesis suggested that the PS collector can create highly smooth and aligned fibrillar scaffolds for the creation of NGCs. In either case, the rigid, aligned nano-fibrillar mesh can be rolled, folded, or cut into smaller units for cultured tissue that may be used for the creation of complex tissues. Here, it was shown in this thesis that neurons may show longer extension on the PS fibers, so such an aligned membrane may also be used in an upright manner to create nerve conduits for the spinal cord. Therefore, the surveyed alignment method provides a guide for future engineering of some tissue products.

Further improvement in image resolution can dramatically enhance the usefulness of the proposed characterization strategy, possibly reducing the need of SEM on fiber characterization. It would be desirable if this characterization strategy could include super-resolution fluorescent imaging, such as stochastic optical reconstruction microscopy (STORM) (Rust *et al.*, 2006, Bates *et al.*, 2007, Huang *et al.*, 2009). It is apparent that in this thesis SEM remains an essential tool in the characterization of the nanofibers because MPM does not have enough resolution to resolve surface details of

the fiber. With the help of STORM, the achievable lateral resolution would be 20 nm with bright, photo-switchable probes with distinct colours. If such resolution can be included in the strategy, it might provide an alternative to the use of SEM. Most electrospun fibers that target tissue engineering uses have a fiber range from 500 nm to 1.5 μm. MPM resolution with SHG is rather limited to 100 nm. If such resolution can be improved by five times, it is possible that SEM characterization of the fiber body would become unnecessary. This may realize the grand assumption of this thesis with one non-invasive, quantitative method that works at every step of the tissue engineering process.

Better characterization of the PSF from the SHG signal would likely improve the quantification power of the characterization strategy. This phenomenon was omitted in this thesis because of the unavailability of a PSF assessment method. Nevertheless, considering the fact that effective voxel control is the key to successful quantification, it was assumed that blind deconvolution could retrieve reliable backward SHG signals for processing. Although the results in Chapters 4 and 6 showed that such an image process could help generate signals that were specific enough to illustrate structural differences, it would certainly create more precise data if the PSF were deconvolved with a protocol that matches the real profile. This may possibly improve the quantification works for finer details in the 3D image.

Lastly, MPM with proper image processing has huge potential to become a novel modelling method for studying 3D AFSs. There are three major challenges to make this method a more reliable tool—faster scanning, automatic image processing, and standardized sample loading. The first is the design of a faster, overlooking scan system. A major drawback of MPM is the relatively long requisite image-acquisition

time due to mechanical scanning and serial acquisition of image frames (Tal *et al.*, 2005). It also demands a lot of memory storage to scan for larger areas using mosaic scanning. In Chapter 6 it was proven that existing image processing algorithms could successfully distinguish slight changes in local collagen density. What remains is an automation solution to connect all the needed processes—look-up table, deconvolution, isosurface, extended depth of field, and surface characterization. This reduces human error and standardizes the calculation for modelling works. Sample preparation and loading are also important parameters that should be controlled. It is important to load the cornea samples in proper positions that can be reproduced. A specifically designed loading chamber might be helpful in standardizing this work. If such an automated system exists, it could help research in 3D AFS by providing a modelling tool using data acquired from a real scaffold. This may significantly affect how researchers in the field approach characterization works and make it easier to observe slight differences in 3D AFSs tissue developments.

References

AFIFI, A. M., NAKAJIMA, H., YAMANE, H., KIMURA, Y. & NAKANO, S. (2009) Fabrication of aligned poly(L-lactide) fibers by electrospinning and drawing. *Macromolecular Materials and Engineering.* **294**, pp. 658-665.

AGARD, D. A., HIRAOKA, Y., SHAW, P. & SEDAT, J. W. (1989). Fluorescence Microscopy in Three Dimensions. In: TAYLOR, D. L. & WANG, Y.-L. (eds.) *Methods in Cell Biology Vol 30(B).* San Diego, CA, U.S.: Academic Press.

AGARWAL, S., GREIMER, A. & WENDORFF, J. H. (2009) Electrospinning of manmade and biopolymer nanofibers—Progress in techniques, materials, and applications. *Advanced Functional Materials.* **19**, pp. 2863-2879.

AGHOLME, L., LINDSTRÖM, T., KÅGEDAL, K., MARCUSSON, J. & HALLBECK, M. (2010) An *in vitro* model for neuroscience: Differentiation of SH-SY5Y cells into cells with morphological and biochemical characteristics of mature neurons. *Journal of Alzheimer's Disease.* **20**, pp. 1069-1082.

ALLISON, S. D. (2008) Analysis of initial burst in PLGA microparticles. *Expert Opinion on Drug Delivery.* **5**(6), pp. 615-628.

AN, J., ZHANG, H., ZHANG, J., ZHAO, Y. & YUAN, X. (2009) Preparation and antibacterial activity of electrospun chitosan/poly(ethylene oxide) membranes containing silver nanoparticles. *Colloid and Polymer Science.* **287**, pp. 1425-1434.

ANDERSSON, R. L., STRÖM, V., GEDDE, U. W., MALLON, P. E., HEDENQVIST, M. S. & OLSSON, R. T. (2014) Micromechanics of ultra-toughened electrospun PMMA/PEO fibres as revealed by *in-situ* tensile testing in an electron microscope. *Scientific Reports.* **4**(6335), pp. 1-8.

ANDRESEN, V., ALEXANDER, S., HEUPEL, W.-M., HIRSCHBERG, M., HOFFMAN, R. M. & FRIEDL, P. (2009) Infrared multiphoton microscopy: Subcellular-resolved deep tissue imaging. *Curr Opin Biotechnol.* **20**, pp. 1-9.

ASADA, Y., KAWAGUCHI, S., HAYASHI, H. & NAKAMURA, T. (1998) Neural repair of the injured spinal cord by grafting: Comparison between peripheral

nerve segments and embryonic homologous structures as a conduit of CNS axons. *Neuroscience Research.* **31**, pp. 241-249.

ATHANASIOU, K. A., AGRAWAL, C. M., BARBER, F. A. & BURKHART, S. S. (1998) Orthopaedic applications for PLA-PGA biodegradable polymers. *Arthroscopy: The Journal of Arthroscopic & Related Surgery.* **14**(7), pp. 726-737.

ATSUTA, I., AYUKAWA, Y., FURUHASHI, A., OGINO, Y., MORIYAMA, Y., TSUKIYAMA, Y. & KOYANO, K. (2014) In vivo and in vitro studies of epithelial cell behavior around titanium implants with machined and rough surfaces. *Clinical Implant Dentistry and Related Research.* **16**(5), pp. 772-781.

AYERS, G. R. & DAINTY, J. C. (1988) Iterative blind deconvolution method and its applications. *Optics Letters.* **13**(7), pp. 547-549.

BADAMI, A. S., KREKE, M. R., THOMPSON, M. S., RIFFLE, J. S. & GOLDSTEIN, A. S. (2006) Effect of fiber diameter on spreading, proliferation, and differentiation of osteoblastic cells on electrospun poly(lactic acid) substrates. *Biomaterials.* **27**, pp. 596-606.

BADROSSAMAY, M. R., MCILWEE, H. A., GOSS, J. A. & PARKER, K. K. (2010) Nanofiber assembly by rotary jet-spinning. *Nano Letters.* **10**, pp. 2257-2261.

BAGHERZADEH, R., LATIFI, M., NAJAR, S. S., TEHRAN, M. A. & KONG, L. (2013) Three-dimensional pore structure analysis of nano/microfibrous scaffolds using confocal laser scanning microscopy. *Journal of Biomedical Materials Research Part A.* **101A**, pp. 765-774.

BAKALAR, M., SCHROEDER, J. L., PURSLEY, R., POHIDA, T. J., GLANCY, B., TAYLOR, J., CHESS, D., KELLMAN, P., XUE, H. & BALABAN, R. S. (2012) Three-dimensional motion tracking for high-resolution optical microscopy, *in vivo*. *Journal of Microscopy.* **246**(3), pp. 237-247.

BANDTLOW, C., ZACHLEDER, T. & SCHWAB, M. E. (1990) Oligodendrocytes arrest neurite growth by contact inhibition. *The Journal of Neuroscience.* **10**(12), pp. 3837-3848.

BASHUR, C. A., DAHLGREN, L. A. & GOLDSTEIN, A. S. (2006) Effect of fiber diameter and orientation on fibroblast morphology and proliferation on electrospun poly (D, L-lactic-*co*-glycolic acid) meshes. *Biomaterials.* **27**, pp. 5681-5688.

BATES, M., HUANG, B., DEMPSEY, G. T. & ZHUANG, X. (2007) Multicolor super-resolution imaging with photo-switchable fluorescent probes. *Science.* **317**(5845), pp. 1749-1753.

BAVEYE, P. (2002) Comment on "Evaluation of biofilm image thresholding methods". *Water Research.* **36**, pp. 805-806.

BAYRAK, A., PRÜGER, P., STOCK, U. A. & SEIFERT, M. (2013) Absence of immune responses with xenogeneic collagen and elastin. *Tissue Engineering Part A.* **19**(13-14), pp. 1592-1600.

BENEDEK, G. B. (1971) Theory of transparency of the eye. *Applied Optics.* **10**(3), pp. 459-473.

BERGSMA, J. E., DE BRUIJN, W. C., ROZEMA, F. R., BOS, R. R. M. & BOERING, G. (1995) Late degradation tissue response to poly(L-lactide) bone plates and screws. *Biomaterials.* **16**(1), pp. 25-31.

BEYENAL, H., DONOVAN, C., LEWANDOWSKI, Z. & HARKIN, G. (2004) Three-dimensional biofilm structure quantification. *Journal of Microbiological Methods.* **59**, pp. 395-413.

BHARDWAJ, N. & KUNDU, S. C. (2010) Electrospinning: A fascinating fiber fabrication technique. *Biotechnology Advances.* **28**(3), pp. 325-347.

BIEDLER, J. L., HELSON, L. & SPENGLER, B. A. (1973) Morphology and growth, tumorigenicity, and cytogenetics of human neuroblastoma cells in continuous culture. *Cancer Research.* **33**(11), pp. 2643-2652.

BILATI, U., ALLÉMANN, E. & DOELKER, E. (2005) Poly(D, L-lactide-co-glycolide) protein-loaded nanoparticles prepared by the double emulsion method-processing and formulation issues for enhanced entrapment efficiency. *Journal of Microencapsulation.* **22**(2), pp. 205-214.

BIRK, D. E., FITCH, J. M. & LINSENMAYER, T. F. (1986) Organization of collagen types I and V in the embryonic chicken cornea. *Investigative Ophthalmology & Visual Science.* **27**(10), pp. 1470-1477.

BLAKENEY, B. A., TAMBRALLI, A., ANDERSON, J. M., ANDUKURI, A., LIM, D.-J., DEAN, D. R. & JUN, H.-W. (2011) Cell infiltration and growth in a low

density, uncompressed three-dimensional electrospun nanofibrous scaffold. *Biomaterials.* **32**, pp. 1583-1590.

BLAND, J. M. & ALTMAN, D. G. (1986) Statistical methods for assessing agreement between two methods of clinical measurement. *Lancet.* **327**(8476), pp. 307-310.

BORCHERDING, M. S., BLACIK, L. J., SITTIG, R. A., BIZZELL, J. W., BREEN, M. & WEINSTEIN, H. G. (1975) Proteoglycans and collagen fibre organization in human corneoscleral tissue. *Exp Eye Res.* **21**, pp. 59-70.

BOSE, G. M. (1745) *Recherches sur la cause et sur la veritable téorie de l'électricité*. Slomac.

BOYD, R. W. (1980) Intuitive explanation of the phase anomaly of focused light beams. *J Opt Soc Am.* **70**(7), pp. 877-880.

BUENO, J. M., GUALDA, E. J. & ARTAL, P. (2011) Analysis of corneal stroma organization with wavefront optimized nonlinear microscopy. *Cornea.* **30**(6), pp. 692-701.

BURGER, C., HSIAO, B. S. & CHU, B. (2006) Nanofibrous materials and their applications. *Annu Rev Mater Res.* **36**, pp. 333-368.

CAMPILLO-FERNÁNDEZ, A. J., UNGER, R. E., PETERS, K., HALSTENBERG, S., SANTOS, M., SÁNCHEZ, M. S., DUEÑAS, J. M. M., PRADAS, M. M., RIBELLES, J. L. G. & KIRKPATRICK, C. J. (2009) Analysis of the biological response of endothelial and fibroblast cells cultured on synthetic scaffolds with various hydrophilic/hydrophobic ratios: Influence of fibronectin adsorption and conformation. *Tissue Engineering Part A.* **15**(6), pp. 1331-1341.

CAO, X. & SHOICHET, M. S. (1999) Delivering neuroactive molecules from biodegradable microspheres for application in central nervous system disorders. *Biomaterials.* **20**, pp. 329-339.

CASADESSUS, O., GEORGES, G., SIOZADE-LAMOINE, L., DEUMIÉ, C., CONRATH, J. & HOFFART, L. Published. Scattering properties and transparency characterization of human corneal grafts. *In:* LEITGEB, R. A. & BOUMA, B. E., eds. Optical Coherence Tomography and Coherence Techniques V, 2011 Munich. Proc. of SPIE-OSA Biomedical Optics, SPIE, p. 80911G.

CENTONZE, V. E. & WHITE, J. G. (1998) Multiphoton excitation provides optical sections from deeper within scattering specimens than confocal imaging. *Biophysical Journal.* **75**, pp. 2015-2024.

CERNAIANU, G., BRANDMAIER, P., SCHOLZ, G., ACKERMANN, O. P., ALT, R., ROTHE, K., CROSS, M., WITZIGMANN, H. & TRÖBS, R. B. (2008) All-*trans* retinoic acid arrests neuroblastoma cells in a dormant state. Subsequent nerve growth factor/brain-derived neurotrophic factor treatment adds modest benefit. *Journal of Pediatric Surgery.* **43**, pp. 1284-1294.

CHAKRAPANI, V. Y., GNANAMANI, A., GIRIDEV, V., MADHUSOOTHANAN, M. & SEKARAN, G. (2012) Electrospinning of type I collagen and PCL nanofibers using acetic acid. *Journal of Applied Polymer Science.* **125**(4), pp. 3221-3227.

CHAKRAVARTI, S., PETROLL, W. M., HASSELL, J. R., JESTER, J. V., LASS, J. H., PAUL, J. & BIRK, D. E. (2000) Corneal opacity in lumican-null mice: Defects in collagen fibril structure and packing in the posterior stroma. *Investigative Ophthalmology & Visual Science.* **41**(11), pp. 3365-3373.

CHANG, C.-J. (2009) The effect of pulse-released nerve growth factor from genipin-crosslinked gelatin in schwann cell-seeded polycaprolactone conduits on large-gap peripheral nerve regeneration. *Tissue Engineering Part A.* **15**(3), pp. 547-557.

CHAUREY, V., CHIANG, P.-C., POLANCO, C., SU, Y.-H., CHOU, C.-F. & SWAMI, N. S. (2010) Interplay of electrical forces for alignment of sub-100 nm electrospun nanofibers on insulator gap collectors. *Langmuir.* **26**(24), pp. 19022-19026.

CHEN, J., LEE, J.-W., HERNANDEZ DE GATICA, N. L., BURKHARDT, C. A., HERCULES, D. M. & GARDELLA JR, J. A. (2000) Time-of-flight secondary ion mass spectrometry studies of hydrolytic degradation kinetics at the surface of poly(glycolic acid). *Macromolecules.* **33**(13), pp. 4726-4732.

CHEVILLE, N. F. & STASKO, J. (2014) Techniques in electron microscopy of animal tissue. *Veterinary Pathology.* **51**(1), pp. 28-41.

CHINGA, G., GREGERSEN, O. & DOUGHERTY, B. (2003) Paper surface characterisation by laser profilometry and image analysis. *Microscopy and Analysis.* **96**, pp. 21-23.

CHINGA, G., JOHNSEN, P. O., DOUGHERTY, R., BERLI, E. L. & WALTER, J. (2007) Quantification of the 3D microstructure of SC surfaces. *Journal of Microscopy.* **227**(3), pp. 254-265.

CHRISTOPHERSON, G. T., SONG, H. & MAO, H.-Q. (2009) The influence of fiber diameter of electrospun substrates on neural stem cell differentiation and proliferation. *Biomaterials.* **30**, pp. 556-564.

CLARK, J. I. (2004) Order and disorder in the transparent media of the eye. *Exp Eye Res.* **78**, pp. 427-432.

COOLEY, J. F. (1902) *Apparatus for electrically dispersing fluids*. U.S. patent application No. 692,631. 4 Feb. 1902.

COREY, J. M., LIN, D. Y., MYCEK, K. B., CHEN, Q., SAMUEL, S., FELDMAN, E. L. & MARTIN, D. C. (2007) Aligned electrospun nanofibers specify the direction of dorsal root ganglia neurite growth. *Journal of Biomedical Materials Research Part A.* **83A**, pp. 636-645.

COURVILLE, C. B., SMOLEK, M. K. & KLYCE, S. D. (2004) Contribution of the ocular surface to visual optics. *Exp Eye Res.* **78**, pp. 417-425.

COX, G., KABLE, E., JONES, A., FRASER, I., MANCONI, F. & GORRELL, M. D. (2003) 3-dimensional imaging of collagen using second harmonic generation. *Journal of Structural Biology.* **141**, pp. 53-62.

CROTTS, G. & PARK, T. G. (1997) Stability and release of bovine serum albumin encapsulated within poly(D,L-lactide-co-glycolide) microparticles. *Journal of Controlled Release.* **44**, pp. 123-134.

DAUD, M. F. B., PAWAR, K. C., CLAEYSSENS, F., RYAN, A. J. & HAYCOCK, J. W. (2012) An aligned 3D neuronal-glial co-culture model for peripheral nerve studies. *Biomaterials.* **33**, pp. 5901-5913.

DE BROUWERE, D., GINIS, H., KYMIONIS, G., NAOUMIDI, I. & PALLIKARIS, I. (2008) Forward scattering properties of corneal haze. *Optometry and Vision Science.* **85**(9), pp. 843-848.

DELMONTE, D. W. & KIM, T. (2011) Anatomy and physiology of the cornea. *Journal of Cataract and Refractive Surgery.* **37**, pp. 588-598.

DENK, W., STRICKLER, J. H. & WEBB, W. W. (1990) Two-photon laser scanning fluorescence microscopy. *Science.* **248**(4951), pp. 73-76.

DEUMENS, R., KOOPMANS, G. C., DEN BAKKER, C. G. J., MAQUET, V., BLACHER, S., HONIG, W. M. M., JÉRÔME, R., PIRARD, J.-P., STEINBUSCH, H. W. M. & JOOSTEN, E. A. J. (2004) Alignment of glial cells stimulates directional neurite growth of CNS neurons *in vitro*. *Neuroscience.* **125**(3), pp. 591-604.

DI LULLO, G. A., SWEENEY, S. M., KÖRKKÖ, J., ALA-KOKKO, L. & SAN ANTONIO, J. D. (2002) Mapping the ligand-binding sites and disease-associated mutations on the most abundant protein in the human, type I collagen. *Journal of Biological Chemistry.* **277**(6), pp. 4223-4231.

DING, B., KIM, H.-Y., LEE, S.-C., LEE, D.-R. & CHOI, K.-J. (2002) Preparation and characterization of nanoscaled poly(vinyl alcohol) fibers via electrospinning. *Fibers and Polymers.* **3**(2), pp. 73-79.

DJAGNY, K. B., WANG, Z. & XU, S. (2001) Gelatin: A valuable protein for food and pharmaceutical industries: Review. *Critical Reviews in Food Science and Nutrition.* **41**(6), pp. 481-492.

DONG, B., ARNOULT, O., SMITH, M. E. & WNEK, G. E. (2009) Electrospinning of collagen nanofiber scaffolds from benign solvents. *Macromolecular Rapid Communications.* **30**, pp. 539-542.

DONG, Y., LI, P., CHEN, C.-B., WANG, Z.-H., MA, P. & CHEN, G.-Q. (2010) The improvement of fibroblast growth on hydrophobic biopolyesters by coating with polyhydroxyalkanoate granule binding protein PhaP fused with cell adhesion motif RGD. *Biomaterials.* **31**, pp. 8921-8930.

DOSHI, J. & RENEKER, D. H. (1995) Electrospinning process and applications of electrospun fibers. *Journal of Electrostatics.* **35**, pp. 151-160.

DOUGHTY, M. J. & ZAMAN, M. L. (2000) Human corneal thickness and its impact on intraocular pressure measures: A review and meta-analysis approach. *Survey of Ophthalmology.* **44**(5), pp. 367-408.

DUAN, B., YUAN, X., ZHU, Y., ZHANG, Y., LI, X., ZHANG, Y. & YAO, K. (2006) A nanofibrous composite membrane of PLGA–chitosan/PVA prepared by electrospinning. *European Polymer Journal.* **42**, pp. 2013-2022.

DUBRUEL, P., UNGER, R., VAN VLIERBERGHE, S., CNUDDE, V., JACOBS, P. J. S., SCHACHT, E. & KIRKPATRICK, C. J. (2007) Porous gelatin hydrogels: 2. In vitro cell interaction study. *Biomacromolecules.* **8**(2), pp. 338-344.

DWANE, S., DURACK, E. & KIELY, P. A. (2013) Optimising parameters for the differentiation of SH-SY5Y cells to study cell adhesion and cell migration. *BMC Research Notes.* **6**, p. 366.

DZIADEK, M., MENASZEK, E., ZAGRAJCZUK, B., PAWLIK, J. & CHOLEWA-KOWALSKA, K. (2015) New generation poly(ε-caprolactone)/gel-derived bioactive glass composites for bone tissue engineering: Part I. Material properties. *Materials Science and Engineering C.* **56**, pp. 9-21.

EDELHAUSER, H. F. (2006) The balance between corneal transparency and edema: The Proctor Lecture. *Investigative Ophthalmology & Visual Science.* **47**(5), pp. 1755-1767.

EDWARDS, M. D., MITCHELL, G. R., MOHAN, S. D. & OLLEY, R. H. (2010) Development of orientation during electrospinning of fibres of poly(ε-caprolactone). *European Polymer Journal.* **46**(6), pp. 1175-1183.

EGERTON, R. F., LI, P. & MALAC, M. (2004) Radiation damage in the TEM and SEM. *Micron.* **35**(6), pp. 399-409.

ELSHEIKH, A., ALHASSO, D. & RAMA, P. (2008) Biomechanical properties of human and porcine corneas. *Exp Eye Res.* **86**, pp. 783-790.

ENCINAS, M., IGLESIAS, M., LIU, Y., WANG, H., MUHAISEN, A., CEÑA, V., GALLEGO, C. & COMELLA, J. X. (2000) Sequential treatment of SH-SY5Y cells with retinoic acid and brain-derived neurotrophic factor gives rise to fully differentiated, neurotrophic factor-dependent, human neuron-like cells. *Journal of Neurochemistry.* **75**(3), pp. 991-1003.

EVANS, G. R. D. Published. Challenges to nerve regeneration. Seminars in Surgical Oncology, 2000. Wiley Online Library, pp. 312-318.

FABER, C., SCHERFIG, E., PRAUSE, J. U. & SØRENSEN, K. E. (2008) Corneal thickness in pigs measured by ultrasound pachymetry in vivo. *Scandinavian Journal of Laboratory Animal Science.* **35**(1), pp. 39-43.

FAGERSTRÖM, S., PÅHLMAN, S., GESTBLOM, C. & NÅNBERG, E. (1996) Protein kinase C-ε is implicated in neurite outgrowth in differentiating human neuroblastoma cells. *Cell Growth and Differentiation.* **7**, pp. 775-785.

FAN, H., LIU, H., WONG, E. J. W., TOH, S. L. & GOH, J. C. H. (2008) In vivo study of anterior cruciate ligament regeneration using mesenchymal stem cells and silk scaffold. *Biomaterials.* **29**, pp. 3324-3337.

FARRELL, R. A., MCCALLY, R. L. & TATHAM, P. E. R. (1973) Wave-length dependencies of light scattering in normal and cold swollen rabbit corneas and their structural implications. *Journal of Physiology.* **233**(3), pp. 589-612.

FENG, S. & WINFUL, H. G. (2001) Physical origin of the Gouy phase shift. *Optics Letters.* **26**(8), pp. 485-487.

FERRO, D. P., VIEIRA-DAMIANI, G., ADAM, R. L., CESAR, C. L. & METZE, K. Published. Nonlinear optics for the study of human scar tissue. SPIE BiOS, 2012 San Francisco, CA. International Society for Optics and Photonics., pp. 82263J-82263J.

FILOVÁ, E., BURDÍKOVÁ, Z., RAMPICHOVÁ, M., BIANCHINI, P., ČAPEK, M., KOŠT'ÁKOVÁ, E., AMLER, E. & KUBÍNOVÁ, L. (2010) Analysis and three-dimensional visualization of collagen in artificial scaffolds using nonlinear microscopy techniques. *J Biomed Opt.* **15**(6), pp. 066011-066011.

FINE, S. & HANSEN, W. P. (1971) Optical second harmonic generation in biological systems. *Applied Optics.* **10**(10), pp. 2350-2353.

FORMHALS, A. (1934) *Process and apparatus for preparing artificial threads*. U.S. patent application No. 1,975,504. 2 Oct. 1934.

FORSTER, B., VAN DE VILLE, D., BERENT, J., SAGE, D. & UNSER, M. (2004) Complex wavelets for extended depth-of-field: A new method for the fusion of multichannel microscopy images. *Microscopy Research and Technique.* **65**, pp. 33-42.

FRANCEL, P. C., SMITH, K. S., STEVENS, F. A., KIM, S. C., GOSSETT, J., GOSSETT, C., DAVIS, M. E., LENAERTS, M. & TOMPKINS, P. (2003) Regeneration of rat sciatic nerve across a LactoSorb bioresorbable conduit with interposed short-segment nerve grafts. *Journal of Neurosurgery.* **99**, pp. 549-554.

FRANKEN, P. A., HILL, A. E., PETERS, C. W. & WEINREICH, G. (1961) Generation of optical harmonics. *Physical Review Letters.* **7**(4), pp. 118-119.

FREEGARD, T. J. (1997) The physical basis of transparency of the normal cornea. *Eye.* **11**(4), pp. 465-471.

FUNG, Y. (2001) A proposal to the National Science Foundation for an engineering research centre at USCD. *Center for the Engineering of Living Tissues UCSD.* **865023**, 2001.

GASPAR, M. M., BLANCO, D., CRUZ, M. E. M. & ALONSO, M. J. (1998) Formulation of L-asparaginase-loaded poly(lactide-co-glycolide) nanoparticles: Influence of polymer properties on enzyme loading, activity and in vitro release. *Journal of Controlled Release.* **52**, pp. 53-62.

GELAIN, F. (2008) Novel opportunities and challenges offered by nanobiomaterials in tissue engineering. *International Journal of Nanomedicine.* **3**(4), pp. 415-424.

GEORGAKOUDI, I., RICE, W. L., HRONIK-TUPAJ, M. & KAPLAN, D. L. (2008) Optical spectroscopy and imaging for the noninvasive evaluation of engineered tissues. *Tissue Engineering Part B Reviews.* **14**(4), pp. 321-340.

GEORGE, A. J. T. & LARKIN, D. F. P. (2004) Corneal transplantation: The forgotten graft. *American Journal of Transplantation.* **4**, pp. 678-685.

GHASEMI-MOBARAKEH, L., PRABHAKARAN, M. P., MORSHED, M., NASR-ESFAHANI, M.-H. & RAMAKRISHNA, S. (2008) Electrospun poly(ε-caprolactone)/gelatin nanofibrous scaffolds for nerve tissue engineering. *Biomaterials.* **29**(34), pp. 4532-4539.

GIANOTTI, S. M., MARSHALL, S. W., HUME, P. A. & BUNT, L. (2009) Incidence of anterior cruciate ligament injury and other knee ligament injuries: A national population-based study. *Journal of Science and Medicine in Sport.* **12**, pp. 622-627.

GILDING, D. K. & REED, A. M. (1979) Biodegradable polymers for use in surgery—polyglycolic/poly(actic acid) homo- and copolymers: 1. *Polymer.* **20**, pp. 1459-1464.

GNAVI, S., FORNASARI, B. E., TONDA-TURO, C., LAURANO, R., ZANETTI, M., CIARDELLI, G. & GEUNA, S. (2015) The effect of electrospun gelatin fibers

alignment on schwann cell and axon behavior and organization in the perspective of artificial nerve design. *International Journal of Molecular Sciences.* **16**(6), pp. 12925-12942.

GÖPPERT-MAYER, M. (1931) Über elementarakte mit zwei quantensprüngen. *Annalen der Physik.* **401**(3), pp. 273-294.

GORGIEVA, S. & KOKOL, V. (2011). Collagen- vs. gelatine-based biomaterials and their biocompatibility: Review and perspectives. In: PIGNATELLO, R. (ed.) *Biomaterials Applications for Nanomedicine.* INTECH Open Access Publisher.

GOUY, L. G. (1890) *Sur une propriété nouvelle des ondes lumineuses*. Gauthier-Villars.

GOVENDER, T., STOLNIK, S., GARNETT, M. C., ILLUM, L. & DAVIS, S. S. (1999) PLGA nanoparticles prepared by nanoprecipitation: Drug loading and release studies of a water soluble drug. *Journal of Controlled Release.* **57**, pp. 171-185.

GRASL, C., ARRAS, M. M. L., STOIBER, M., BERGMEISTER, H. & SCHIMA, H. (2013) Electrodynamic control of the nanofiber alignment during electrospinning. *Applied Physics Letters.* **102**, pp. 053111-053111.

GREENSPAN, P., MAYER, E. P. & FOWLER, S. D. (1985) Nile red: A selective fluorescent stain for intracellular lipid droplets. *Journal of Cell Biology*. **100**, pp. 965-973.

GREINER, A. & WENDORFF, J. H. (2007) Electrospinning: A fascinating method for the preparation of ultrathin fibers. *Angewandte Chemie - International Edition.* **46**, pp. 5670-5703.

GUNN, J. W., TURNER, S. D. & MANN, B. K. (2005) Adhesive and mechanical properties of hydrogels influence neurite extension. *Journal of Biomedical Materials Research Part A.* **72A**, pp. 91-97.

GUPTA, D., VENUGOPAL, J., PRABHAKARAN, M. P., DEV, V. R. G., LOW, S., CHOON, A. T. & RAMAKRISHNA, S. (2009) Aligned and random nanofibrous substrate for the in vitro culture of Schwann cells for neural tissue engineering. *Acta Biomaterialia.* **5**, pp. 2560-2569.

HAMMOUDA, B. (2006) Solvation characteristics of a model water-soluble polymer. *Journal of Polymer Science Part B: Polymer Physics.* **44**, pp. 3195-3199.

HAN, N., RAO, S. S., JOHNSON, J., PARIKH, K. S., BRADLEY, P. A., LANNUTTI, J. J. & WINTER, J. O. (2011) Hydrogel-electrospun fiber mat composite coatings for neural prostheses. *Frontiers in Neuroengineering.* **4**(2), pp. 1-8.

HAR-EL, Y.-E., GERSTENHABER, J. A., BRODSKY, R., HUNEKE, R. B. & LELKES, P. I. (2014) Electrospun soy protein scaffolds as wound dressings: Enhanced reepithelialization in a porcine model of wound healing. *Wound Medicine.* **5**, pp. 9-15.

HARRIS, J. M. & CHESS, R. B. (2003) Effect of pegylation on pharmaceuticals. *Nature Reviews Drug Discovery.* **2**(3), pp. 214-221.

HASHEMI, H. & MEHRAVARAN, S. (2010) Day to day clinically relevant corneal elevation, thickness, and curvature parameters using the orbscan II scanning slit topographer and the pentacam scheimpflug imaging device. *Middle East African Journal of Ophthalmology.* **17**(1), pp. 44-55.

HASSELL, J. R. & BIRK, D. E. (2010) The molecular basis of corneal transparency. *Exp Eye Res.* **91**, pp. 326-335.

HAUPERT, L. M. & SIMPSON, G. J. (2009) Chirality in nonlinear optics. *Annual Review of Physical Chemistry.* **60**, pp. 345-365.

HELMCHEN, F. & DENK, W. (2005) Deep tissue two-photon microscopy. *Nature Methods.* **2**(12), pp. 932-940.

HEUNIS, T., BSHENA, O., KLUMPERMAN, B. & DICKS, L. (2011) Release of bacteriocins from nanofibers prepared with combinations of poly(D, L-lactide) (PDLLA) and poly(ethylene oxide) (PEO). *International Journal of Molecular Sciences.* **12**, pp. 2158-2173.

HEYDARKHAN-HAGVALL, S., SCHENKE-LAYLAND, K., DHANASOPON, A. P., ROFAIL, F., SMITH, H., WU, B. M., SHEMIN, R., BEYGUI, R. E. & MACLELLAN, W. R. (2008) Three-dimensional electrospun ECM-based hybrid scaffolds for cardiovascular tissue engineering. *Biomaterials.* **29**, pp. 2907-2914.

HO, S. T. & HUTMACHER, D. W. (2006) A comparison of micro CT with other techniques used in the characterization of scaffolds. *Biomaterials.* **27**, pp. 1362-1376.

HOLMES, T. J. (1992) Blind deconvolution of quantum-limited incoherent imagery: Maximum-likelihood approach. *J Opt Soc Am A.* **9**(7), pp. 1052-1061.

HORBETT, T. A., WALDBURGER, J. J., RATNER, B. D. & HOFFMAN, A. S. (1988) Cell adhesion to a series of hydrophilic–hydrophobic copolymers studied with a spinning disc apparatus. *Journal of Biomedical Materials Research.* **22**(5), pp. 383-404.

HOU, H. & RENEKER, D. H. (2004) Carbon nanotubes on carbon nanofibers: A novel structure based on electrospun polymer nanofibers. *Advanced Materials.* **16**(1), pp. 69-73.

HSU, W.-M., CHEN, K.-H., LAI, J.-Y. & HSIUE, G.-H. (2013) Transplantation of human corneal endothelial cells using functional biomaterials: Poly (N-isopropylacrylamide) and gelatin. *Journal of Experimental & Clinical Medicine.* **5**(2), pp. 56-64.

HUANG, B., BATES, M. & ZHUANG, X. (2009) Super-resolution fluorescence microscopy. *Annual Review of Biochemistry.* **78**, pp. 993-1016.

HUANG, C., OUYANG, Y., NIU, H., HE, N., KE, Q., JIN, X., LI, D., FANG, J., LIU, W., FAN, C. & LIN, T. (2015) Nerve guidance conduits from aligned nanofibers: Improvement of nerve regeneration through longitudinal nanogrooves on a fiber surface. *ACS Applied Materials and Interfaces.* **7**, pp. 7189-7196.

HUANG, L., NAGAPUDI, K., APKARIAN, R. P. & CHAIKOF, E. L. (2001) Engineered collagen–PEO nanofibers and fabrics. *Journal of Biomaterials Science, Polymer Edition.* **12**(9), pp. 979-993.

HUANG, Z.-M., ZHANG, Y.-Z., KOTAKI, M. & RAMAKRISHNA, S. (2003) A review on polymer nanofibers by electrospinning and their applications in nanocomposites. *Composites Science and Technology.* **63**, pp. 2223-2253.

HUANG, Z. & YANG, A. (2006) Encapsulation of pure drugs into the central part of polycaprolactone ultrafine fibers. *Acta Polymerica Sinica.* **1**, pp. 48-52.

HUMPHRIES, J. D., BYRON, A. & HUMPHRIES, M. J. (2006) Integrin ligands at a glance. *Journal of Cell Science.* **119**(19), pp. 3901-3903.

HUTMACHER, D. W. (2000) Scaffolds in tissue engineering bone and cartilage. *Biomaterials.* **21**, pp. 2529-2543.

IMANISHI, Y., LODOWSKI, K. H. & KOUTALOS, Y. (2007) Two-photon microscopy: Shedding light on the chemistry of vision. *Biochemistry.* **46**(34), pp. 9674-9684.

IOZZO, R. V. (1999) The biology of the small leucine-rich proteoglycans: Functional network of interactive proteins. *Journal of Biological Chemistry.* **274**(27), pp. 18843-18846.

JACKSON, H. (1996) Bilateral blindness due to trauma in Cambodia. *Eye.* **10**, pp. 517-520.

JACKSON, M., CHOO, L.-P. I., WATSON, P. H., HALLIDAY, W. C. & MANTSCH, H. H. (1995) Beware of connective tissue proteins: Assignment and implications of collagen absorptions in infrared spectra of human tissues. *Biochimica et Biophysica Acta.* **1270**, pp. 1-6.

JAIN, R. A. (2000) The manufacturing techniques of various drug loaded biodegradable poly(lactide-co-glycolide) (PLGA) devices. *Biomaterials.* **21**, pp. 2475-2490.

JALBERT, I. & STAPLETON, F. (2005) The corneal stroma during contact lens wear. *Contact Lens and Anterior Eye.* **28**, pp. 3-12.

JAY, L., BROCAS, A., SINGH, K., KIEFFER, J.-C., BRUNETTE, I. & OZAKI, T. (2008) Determination of porcine corneal layers with high spatial resolution by simultaneous second and third harmonic generation microscopy. *Optics Express.* **16**(21), pp. 16284-16293.

JESTER, J. V. (2008) Corneal crystallins and the development of cellular transparency. *Seminars in Cell and Developmental Biology.* **19**, pp. 82-93.

JIANG, H., HU, Y., LI, Y., ZHAO, P., ZHU, K. & CHEN, W. (2005) A facile technique to prepare biodegradable coaxial electrospun nanofibers for controlled release of bioactive agents. *Journal of Controlled Release.* **108**, pp. 237-243.

JIANG, H., HU, Y., ZHAO, P., LI, Y. & ZHU, K. (2006) Modulation of protein release from biodegradable core-shell structured fibers prepared by coaxial electrospinning. *Journal of Biomedical Materials Research Part B: Applied Biomaterials.* **79**(1), pp. 50-57.

JOHANSEN, P., MEN, Y., AUDRAN, R., CORRADIN, G., MERKLE, H. P. & GANDER, B. (1998) Improving stability and release kinetics of

microencapsulated tetanus toxoid by co-encapsulation of additives. *Pharmaceutical Research.* **15**(7), pp. 1103-1110.

KANNUS, P. (2000) Structure of the tendon connective tissue. *Scandinavian Journal of Medicine & Science in Sports.* **10**, pp. 312-320.

KATAGIRI, Y., BREW, S. A. & INGHAM, K. C. (2003) All six modules of the gelatin-binding domain of fibronectin are required for full affinity. *Journal of Biological Chemistry.* **278**(14), pp. 11897-11902.

KATTA, P., ALESSANDRO, M., RAMSIER, R. & CHASE, G. (2004) Continuous electrospinning of aligned polymer nanofibers onto a wire drum collector. *Nano Letters.* **4**(11), pp. 2215-2218.

KELLOMÄKI, M., NIIRANEN, H., PUUMANEN, K., ASHAMMAKHI, N., WARIS, T. & TÖRMÄLÄ, P. (2000) Bioabsorbable scaffolds for guided bone regeneration and generation. *Biomaterials.* **21**, pp. 2495-2505.

KELSO, J. M. (1999) The gelatin story. *Journal of Allergy and Clinical Immunology.* **103**(2), pp. 200-202.

KHIL, M.-S., CHA, D.-I., KIM, H.-Y., KIM, I.-S. & BHATTARAI, N. (2003) Electrospun nanofibrous polyurethane membrane as wound dressing. *Journal of Biomedical Materials Research Part B: Applied Biomaterials.* **67B**, pp. 675-679.

KIM, B. M., EICHLER, J., REISER, K. M., RUBENCHIK, A. M. & DA SILVA, L. B. (2000) Collagen structure and nonlinear susceptibility: Effects of heat, glycation, and enzymatic cleavage on second harmonic signal intensity. *Lasers in Surgery and Medicine.* **27**, pp. 329-335.

KIM, D.-H. & MARTIN, D. C. (2006) Sustained release of dexamethasone from hydrophilic matrices using PLGA nanoparticles for neural drug delivery. *Biomaterials.* **27**, pp. 3031-3037.

KIM, G., YOON, H. & PARK, Y. (2010) Drug release from various thicknesses of layered mats consisting of electrospun polycaprolactone and polyethylene oxide micro/nanofibers. *Applied Physics A.* **100**, pp. 1197-1204.

KIM, H. K. & PARK, T. G. (1999) Microencapsulation of human growth hormone within biodegradable polyester microspheres: Protein aggregation stability and

incomplete release mechanism. *Biotechnology and Bioengineering.* **65**(6), pp. 659-667.

KIM, K., YU, M., ZONG, X., CHIU, J., FANG, D., SEO, Y.-S., HSIAO, B. S., CHU, B. & HADJIARGYROU, M. (2003) Control of degradation rate and hydrophilicity in electrospun non-woven poly (D, L-lactide) nanofiber scaffolds for biomedical applications. *Biomaterials.* **24**, pp. 4977-4985.

KISELEV, P. & ROSELL-LLOMPART, J. (2012) Highly aligned electrospun nanofibers by elimination of the whipping motion. *Journal of Applied Polymer Science.* **125**, pp. 2433-2441.

KLEIN, S. A. & MANDELL, R. B. (1995) Shape and refractive powers in corneal topography. *Investigative Ophthalmology & Visual Science.* **36**(10), pp. 2096-2109.

KLOTZ, S. A. & SMITH, R. L. (1995) Gelatin fragments block adherence of *Candida albicans* to extracellular matrix proteins. *Microbiology.* **141**, pp. 2681-2684.

KNIGHT, M. M., ROBERTS, S. R., LEE, D. A. & BADER, D. L. (2003) Live cell imaging using confocal microscopy induces intracellular calcium transients and cell death. *American Journal of Physiology-Cell Physiology.* **284**, pp. C1083-C1089.

KOKARE, C. R. (2008) *Pharmaceutical Microbiology-Principles and Applications,* 6th Edition. Pune: Nirali Prakashan.

KUMAR, M. N. V. R., BAKOWSKY, U. & LEHR, C. M. (2004) Preparation and characterization of cationic PLGA nanospheres as DNA carriers. *Biomaterials.* **25**, pp. 1771-1777.

LABOUR, M.-N., BANC, A., TOURRETTE, A., CUNIN, F., VERDIER, J.-M., DEVOISSELLE, J.-M., MARCILHAC, A. & BELAMIE, E. (2012) Thick collagen-based 3D matrices including growth factors to induce neurite outgrowth. *Acta Biomaterialia.* **8**, pp. 3302-3312.

LABOUTA, H. I., KRAUS, T., EL-KHORDAGUI, L. K. & SCHNEIDER, M. (2011) Combined multiphoton imaging-pixel analysis for semiquantitation of skin penetration of gold nanoparticles. *International Journal of Pharmaceutics.* **413**, pp. 279-282.

LACOMB, R., NADIARNYKH, O., TOWNSEND, S. S. & CAMPAGNOLA, P. J. (2008) Phase matching considerations in second harmonic generation from tissues: Effects on emission directionality, conversion efficiency and observed morphology. *Optics Communications.* **281**, pp. 1823-1832.

LAI, J.-Y. & HSIEH, A.-C. (2012) A gelatin-*g*-poly (N-isopropylacrylamide) biodegradable in situ gelling delivery system for the intracameral administration of pilocarpine. *Biomaterials.* **33**, pp. 2372-2387.

LAI, T. & TANG, S. (2014) Cornea characterization using a combined multiphoton microscopy and optical coherence tomography system. *Biomedical Optics Express.* **5**(5), pp. 1494-1511.

LAM, E. Y. & GOODMAN, J. W. (2000) Iterative statistical approach to blind image deconvolution. *J Opt Soc Am A.* **17**(7), pp. 1177-1184.

LANGER, R. & CHASIN, M. (eds.) (1990) *Biodegradable Polymers as Drug Delivery Systems.* New York: Marcel Dekker.

LEACH, J. B., BROWN, X. Q., JACOT, J. G., DIMILLA, P. A. & WONG, J. Y. (2007) Neurite outgrowth and branching of PC12 cells on very soft substrates sharply decreases below a threshold of substrate rigidity. *Journal of Neural Engineering.* **4**, pp. 26-34.

LEE, H., YOON, H. & KIM, G. (2009) Highly oriented electrospun polycaprolactone micro/nanofibers prepared by a field-controllable electrode and rotating collector. *Applied Physics A.* **97**, pp. 559-565.

LEONG, K. F., CHUA, C. K., SUDARMADJI, N. & YEONG, W. Y. (2008) Engineering functionally graded tissue engineering scaffolds. *Journal of the Mechanical Behavior of Biomedical Materials.* **1**(2), pp. 140-152.

LEUNG, V., HARTWELL, R., YANG, H., GHAHARY, A. & KO, F. (2011) Bioactive nanofibres for wound healing applications. *J Fiber Bioeng Informat.* **4**(1), pp. 1-14.

LEVIN, A., WEISS, Y., DURAND, F. & FREEMAN, W. T. Published. Understanding and evaluating blind deconvolution algorithms. 2009 IEEE Computer Society Conference on Computer Vision and Pattern Recognition Workshops, CVPR Workshops 2009, 2009 Miami, FL. pp. 1964-1971.

LI, C., VEPARI, C., JIN, H.-J., KIM, H. J. & KAPLAN, D. L. (2006) Electrospun silk-BMP-2 scaffolds for bone tissue engineering. *Biomaterials.* **27**, pp. 3115-3124.

LI, D., HERRICKS, T. & XIA, Y. (2003a) Magnetic nanofibers of nickel ferrite prepared by electrospinning. *Applied Physics Letters.* **83**(22), pp. 4586-4588.

LI, D., WANG, Y. & XIA, Y. (2003b) Electrospinning of polymeric and ceramic nanofibers as uniaxially aligned arrays. *Nano Letters.* **3**(8), pp. 1167-1171.

LI, D. & XIA, Y. (2004) Electrospinning of nanofibers: Reinventing the wheel? *Advanced Materials.* **16**(14), pp. 1151-1170.

LI, F., YU, D., LIN, X., LIU, D., XIA, H. & CHEN, S. (2012a) Biodegradation of poly(ε-caprolactone)(PCL) by a new *Penicillium oxalicum* strain DSYD05-1. *World Journal of Microbiology and Biotechnology.* **28**, pp. 2929-2935.

LI, G. N., LIVI, L. L., GOURD, C. M., DEWEERD, E. S. & HOFFMAN-KIM, D. (2007) Genomic and morphological changes of neuroblastoma cells in response to three-dimensional matrices. *Tissue Engineering.* **13**(5), pp. 1035-1047.

LI, H., YAO, Z., JIANG, J., HUA, Y., CHEN, J., LI, Y., GAO, K. & CHEN, S. (2012b) Biologic failure of a ligament advanced reinforcement system artificial ligament in anterior cruciate ligament reconstruction: A report of serious knee synovitis. *Arthroscopy: The Journal of Arthroscopic & Related Surgery.* **28**(4), pp. 583-586.

LI, M., MONDRINOS, M. J., GANDHI, M. R., KO, F. K., WEISS, A. S. & LELKES, P. I. (2005) Electrospun protein fibers as matrices for tissue engineering. *Biomaterials.* **26**, pp. 5999-6008.

LI, W.-J., LAURENCIN, C. T., CATERSON, E. J., TUAN, R. S. & KO, F. K. (2002) Electrospun nanofibrous structure: A novel scaffold for tissue engineering. *Journal of Biomedical Materials Research.* **60**, pp. 613-621.

LI, Z., SUN, H., ZHANG, J., ZHANG, H., MENG, F. & CUI, Z. (2013) Development of in vitro 3D TissueFlex® islet model for diabetic drug efficacy testing. *PLoS One.* **8**(8), p. e72612.

LIU, J.-J., WANG, C.-Y., WANG, J.-G., RUAN, H.-J. & FAN, C.-Y. (2011) Peripheral nerve regeneration using composite poly(lactic acid-caprolactone)/nerve growth

factor conduits prepared by coaxial electrospinning. *Journal of Biomedical Materials Research Part A.* **96A**, pp. 13-20.

LIU, L. & DZENIS, Y. A. (2008) Analysis of the effects of the residual charge and gap size on electrospun nanofiber alignment in a gap method. *Nanotechnology.* **19**, p. 355307.

LOSCERTALES, I. G., BARRERO, A., GUERRERO, I., CORTIJO, R., MARQUEZ, M. & GAÑÁN-CALVO, A. M. (2002) Micro/nano encapsulation via electrified coaxial liquid jets. *Science.* **295**(5560), pp. 1695-1698.

LOW, W. C., RUJITANAROJ, P.-O., LEE, D.-K., MESSERSMITH, P. B., STANTON, L. W., GOH, E. & CHEW, S. Y. (2013) Nanofibrous scaffold-mediated REST knockdown to enhance neuronal differentiation of stem cells. *Biomaterials.* **34**, pp. 3581-3590.

LU, W. & PARK, T. G. (1995) Protein release from poly(lactic-co-glycolic acid) microspheres: Protein stability problems. *PDA Journal of Pharmaceutical Science and Technology.* **49**(1), pp. 13-19.

LYU, S., HUANG, C., YANG, H. & ZHANG, X. (2013) Electrospun fibers as a scaffolding platform for bone tissue repair. *Journal of Orthopaedic Research.* **31**(9), pp. 1382-1389.

MA, P. X. & ZHANG, R. (2001) Microtubular architecture of biodegradable polymer scaffolds. *Journal of Biomedical Materials Research.* **56**(4), pp. 469-477.

MAKADIA, H. K. & SIEGEL, S. J. (2011) Poly lactic-co-glycolic acid (PLGA) as biodegradable controlled drug delivery carrier. *Polymers.* **3**, pp. 1377-1397.

MANICKAVASAGAM, A., HIRVONEN, L. M., MELITA, L. N., CHONG, E. Z., COOK, R. J., BOZEC, L. & FESTY, F. (2014) Multimodal optical characterisation of collagen photodegradation by femtosecond infrared laser ablation. *Analyst.* **139**, pp. 6135-6143.

MATTEINI, P., CICCHI, R., RATTO, F., KAPSOKALYVAS, D., ROSSI, F., DE ANGELIS, M., PAVONE, F. S. & PINI, R. (2012) Thermal transitions of fibrillar collagen unveiled by second-harmonic generation microscopy of corneal stroma. *Biophysical Journal.* **103**(6), pp. 1179-1187.

MATTEINI, P., RATTO, F., ROSSI, F., CICCHI, R., STRINGARI, C., KAPSOKALYVAS, D., PAVONE, F. S. & PINI, R. (2009) Photothermally-induced disordered patterns of corneal collagen revealed by SHG imaging. *Optics Express.* **17**(6), pp. 4868-4878.

MATTHEWS, J. A., WNEK, G. E., SIMPSON, D. G. & BOWLIN, G. L. (2002) Electrospinning of collagen nanofibers. *Biomacromolecules.* **3**, pp. 232-238.

MATTSON, M. P., GUTHRIE, P. B. & KATER, S. B. (1988) Components of neurite outgrowth that determine neuronal cytoarchitecture: Influence of calcium and the growth substrate. *Journal of Neuroscience Research.* **20**, pp. 331-345.

MATURANA, L. G., PIERUCCI, A., SIMÕES, G. F., VIDIGAL, M., DUEK, E. A. R., VIDAL, B. C. & OLIVEIRA, A. L. R. (2013) Enhanced peripheral nerve regeneration by the combination of a polycaprolactone tubular prosthesis and a scaffold of collagen with supramolecular organization. *Brain and Behavior*. **3**(4), pp. 417-430.

MAURICE, D. M. (1957) The structure and transparency of the cornea. *The Journal of Physiology*. **136**(2), pp. 263-286.

MEEK, K. M. (2009) Corneal collagen—its role in maintaining corneal shape and transparency. *Biophysical Reviews.* **1**(2), pp. 83-93.

MEINEL, L., KARAGEORGIOU, V., FAJARDO, R., SNYDER, B., SHINDE-PATIL, V., ZICHNER, L., KAPLAN, D., LANGER, R. & VUNJAK-NOVAKOVIC, G. (2004) Bone tissue engineering using human mesenchymal stem cells: Effects of scaffold material and medium flow. *Annals of Biomedical Engineering.* **32**(1), pp. 112-122.

MERTZ, J. & MOREAUX, L. (2001) Second-harmonic generation by focused excitation of inhomogeneously distributed scatterers. *Optics Communications.* **196**, pp. 325-330.

MEYLE, J., GÜLTIG, K., WOLBURG, H. & VON RECUM, A. F. (1993) Fibroblast anchorage to microtextured surfaces. *Journal of Biomedical Materials Research.* **27**(12), pp. 1553-1557.

MØLLER-PEDERSEN, T. (2004) Keratocyte reflectivity and corneal haze. *Exp Eye Res.* **78**, pp. 553-560.

MOREAUX, L., SANDRE, O., CHARPAK, S., BLANCHARD-DESCE, M. & MERTZ, J. (2001) Coherent scattering in multi-harmonic light microscopy. *Biophysical Journal.* **80**, pp. 1568-1574.

MORGAN, S. P., ROSE, F. R. & MATCHER, S. J. (eds.) (2013a) *Optical Techniques in Regenerative Medicine.* Boca Raton, Florida: CRC Press.

MORGAN, S. P., WILSON, B. C., VITKIN, I. A. & ROSE, F. R. A. J. (2013b). The Role of Optical Techniques in Regenerative Medicine. In: MORGAN, S. P., ROSE, F. R. & MATCHER, S. J. (eds.) *Optical Techniques in Regenerative Medicine.* Boca Raton, Florida: CRC Press.

MORONI, L., LICHT, R., DE BOER, J., DE WIJN, J. R. & VAN BLITTERSWIJK, C. A. (2006) Fiber diameter and texture of electrospun PEOT/PBT scaffolds influence human mesenchymal stem cell proliferation and morphology, and the release of incorporated compounds. *Biomaterials.* **27**, pp. 4911-4922.

MORTON, W. J. (1902) *Method of dispersing fluids*. U.S. patent application No. 705,691. 29 Jul. 1902.

MUGURUMA, K., NISHIYAMA, A., ONO, Y., MIYAWAKI, H., MIZUHARA, E., HORI, S., KAKIZUKA, A., OBATA, K., YANAGAWA, Y., HIRANO, T. & SASAI, Y. (2010) Ontogeny-recapitulating generation and tissue integration of ES cell-derived Purkinje cells. *Nature Neuroscience.* **13**(10), pp. 1171-1180.

MULLINS, R. J. (2003) Anaphylaxis: Risk factors for recurrence. *Clinical & Experimental Allergy.* **33**, pp. 1033-1040.

MUNDARGI, R. C., BABU, V. R., RANGASWAMY, V., PATEL, P. & AMINABHAVI, T. M. (2008) Nano/micro technologies for delivering macromolecular therapeutics using poly(D, L-lactide-*co*-glycolide) and its derivatives. *Journal of Controlled Release.* **125**, pp. 193-209.

MURPHY, D. B. (2002) *Fundamentals of light microscopy and electronic imaging*. New York: John Wiley & Sons.

NANCI, A., ZALZAL, S., GOTOH, Y. & MCKEE, M. D. (1996) Ultrastructural characterization and immunolocalization of osteopontin in rat calvarial osteoblast primary cultures. *Microscopy Research and Technique.* **33**(2), pp. 214-231.

NATU, M. V., SARDINHA, J. P., CORREIA, I. J. & GIL, M. H. (2007) Controlled release gelatin hydrogels and lyophilisates with potential application as ocular inserts. *Biomedical Materials.* **2**, pp. 241-249.

NAYAK, R., PADHYE, R., KYRATZIS, I. L., TRUONG, Y. B. & ARNOLD, L. (2011) Recent advances in nanofibre fabrication techniques. *Textile Research Journal.* **82**(2), pp. 129-147.

NIEDERKORN, J. Y. (2006) See no evil, hear no evil, do no evil: The lessons of immune privilege. *Nature Immunology.* **7**(4), pp. 354-359.

NIESNER, R., ANDRESEN, V., NEUMANN, J., SPIECKER, H. & GUNZER, M. (2007) The power of single and multibeam two-photon microscopy for high-resolution and high-speed deep tissue and intravital imaging. *Biophysical Journal.* **93**, pp. 2519-2529.

O'SHEA, S. & DANIELS, F. B. (2012). Combination Products. In: PIÑA, K. R. & PINES, W. L. (eds.) *A Practical Guide to FDA's Food and Drug Law and Regulation.* 4 ed. Washington, D.C., U.S.: Food and Drug Law Institute.

OHEIM, M., BEAUREPAIRE, E., CHAIGNEAU, E., MERTZ, J. & CHARPAK, S. (2001) Two-photon microscopy in brain tissue: Parameters influencing the imaging depth. *Journal of Neuroscience Methods.* **111**, pp. 29-37.

ORCHEL, A., JELONEK, K., KASPERCZYK, J. & DZIERZEWICZ, Z. (2010) Growth of human fibroblasts in the presence of 6-hydroxyhexanoic acid. *Acta Poloniae Pharmaceutica - Drug Research.* **67**(6), pp. 710-712.

PAHLMAN, S., ODELSTAD, L., LARSSON, E., GROTTE, G. & NILSSON, K. (1981) Phenotypic changes of human neuroblastoma cells in culture induced by 12-*O*-tetradecanoyl-phorbol-13-acetate. *International Journal of Cancer.* **28**, pp. 583-589.

PAHUJA, P., ARORA, S. & PAWAR, P. (2012) Ocular drug delivery system: A reference to natural polymers. *Expert Opinion on Drug Delivery.* **9**(7), pp. 837-861.

PAN, H., LI, L., HU, L. & CUI, X. (2006) Continuous aligned polymer fibers produced by a modified electrospinning method. *Polymer.* **47**, pp. 4901-4904.

PARK, E. K., KIM, S. Y., LEE, S. B. & LEE, Y. M. (2005) Folate-conjugated methoxy poly(ethylene glycol)/poly(ε-caprolactone) amphiphilic block copolymeric micelles for tumor-targeted drug delivery. *Journal of Controlled Release.* **109**, pp. 158-168.

PARK, T. G., LEE, H. Y. & NAM, Y. S. (1998) A new preparation method for protein loaded poly(D,L-lactic-co-glycolic acid) microspheres and protein release mechanism study. *Journal of Controlled Release.* **55**, pp. 181-191.

PARK, T. G., LU, W. & CROTTS, G. (1995) Importance of *in vitro* experimental conditions on protein release kinetics, stability and polymer degradation in protein encapsulated poly(D, L-lactic acid-co-glycolic acid) microspheres. *Journal of Controlled Release.* **33**, pp. 211-222.

PARRA, S. G., CHIA, T. H., ZINTER, J. P. & LEVENE, M. J. (2010) Multiphoton microscopy of cleared mouse organs. *J Biomed Opt.* **15**(3), p. 036017.

PATINO, M. G., NEIDERS, M. E., ANDREANA, S., NOBLE, B. & COHEN, R. E. (2003) Cellular inflammatory response to porcine collagen membranes. *Journal of periodontal research.* **38**(5), pp. 458-464.

PEDICINI, A. & FARRIS, R. J. (2003) Mechanical behavior of electrospun polyurethane. *Polymer.* **44**, pp. 6857-6862.

PENA, A.-M., BOULESTEIX, T., DARTIGALONGUE, T. & SCHANNE-KLEIN, M.-C. (2005) Chiroptical effects in the second harmonic signal of collagens I and IV. *Journal of the American Chemical Society.* **127**, pp. 10314-10322.

PETERSON, D. A. (1999) Quantitative histology using confocal microscopy: Implementation of unbiased stereology procedures. *Methods.* **18**, pp. 493-507.

PHAM, Q. P., SHARMA, U. & MIKOS, A. G. (2006) Electrospun poly(ε-caprolactone) microfiber and multilayer nanofiber/microfiber scaffolds: Characterization of scaffolds and measurement of cellular infiltration. *Biomacromolecules.* **7**(10), pp. 2796-2805.

PITT, C. G., GRATZL, M. M., JEFFCOAT, A. R., ZWEIDINGER, R. & SCHINDLER, A. (1979) Sustained drug delivery systems II: Factors affecting release rates from poly(ε-caprolactone) and related biodegradable polyesters. *Journal of Pharmaceutical Sciences.* **68**(12), pp. 1534-1538.

POOL, M., THIEMANN, J., BAR-OR, A. & FOURNIER, A. E. (2008) NeuriteTracer: A novel ImageJ plugin for automated quantification of neurite outgrowth. *Journal of Neuroscience Methods.* **168**, pp. 134-139.

POOL, V., BRAUN, M. M., KELSO, J. M., MOOTREY, G., CHEN, R. T., YUNGINGER, J. W., JACOBSON, R. M. & GARGIULLO, P. M. (2002) Prevalence of anti-gelatin IgE antibodies in people with anaphylaxis after measles-mumps-rubella vaccine in the United States. *Pediatrics.* **110**(6), p. e71.

PRASHER, D. C., ECKENRODE, V. K., WARD, W. W., PRENDERGAST, F. G. & CORMIER, M. J. (1992) Primary structure of the Aequorea victoria green-fluorescent protein. *Gene.* **111**, pp. 229-233.

PRYSTUPA, D. A. & DONALD, A. M. (1996) Infrared study of gelatin conformations in the gel and sol states. *Polymer Gels and Networks.* **4**, pp. 87-110.

QAZI, Y., WONG, G., MONSON, B., STRINGHAM, J. & AMBATI, B. K. (2010) Corneal transparency: Genesis, maintenance and dysfunction. *Brain Research Bulletin.* **81**, pp. 198-210.

QU, H., WEI, S. & GUO, Z. (2013) Coaxial electrospun nanostructures and their applications. *Journal of Materials Chemistry A.* **1**, pp. 11513-11528.

RALSTON, E., SWAIM, B., CZAPIGA, M., HWU, W.-L., CHIEN, Y.-H., PITTIS, M. G., BEMBI, B., SCHWARTZ, O., PLOTZ, P. & RABEN, N. (2008) Detection and imaging of non-contractile inclusions and sarcomeric anomalies in skeletal muscle by second harmonic generation combined with two-photon excited fluorescence. *Journal of Structural Biology.* **162**, pp. 500-508.

RAMAY, H. R. & ZHANG, M. (2003) Preparation of porous hydroxyapatite scaffolds by combination of the gel-casting and polymer sponge methods. *Biomaterials.* **24**, pp. 3293-3302.

RATCLIFFE, A., BUTLER, D. L., DYMENT, N. A., CAGLE JR, P. J., PROCTOR, C. S., RATCLIFFE, S. S. & FLATOW, E. L. (2015) Scaffolds for tendon and ligament repair and regeneration. *Annals of Biomedical Engineering.* **43**(3), pp. 819-831.

RATNER, B. D., HOFFMAN, A. S., SCHOEN, F. J. & LEMONS, J. E. (eds.) (2004) *Biomaterials Science: An Introduction to Materials in Medicine.* 2nd Edition. San Diego, California, U.S.: Academic Press.

RAYLEIGH, L. (1882) XX. On the equilibrium of liquid conducting masses charged with electricity. *The London, Edinburgh, and Dublin Philosophical Magazine and Journal of Science.* **14**(87), pp. 184-186.

RECKNOR, J. B., RECKNOR, J. C., SAKAGUCHI, D. S. & MALLAPRAGADA, S. K. (2004) Oriented astroglial cell growth on micropatterned polystyrene substrates. *Biomaterials.* **25**, pp. 2753-2767.

REED, A. M. & GILDING, D. K. (1981) Biodegradable polymers for use in surgery—poly(glycolic)/poly(Iactic acid) homo and copolymers: 2. *In vitro* degradation. *Polymer.* **22**, pp. 494-498.

RENEKER, D. H. & CHUN, I. (1996) Nanometre diameter fibres of polymer, produced by electrospinning. *Nanotechnology.* **7**, pp. 216-223.

RENEKER, D. H., YARIN, A. L., FONG, H. & KOOMBHONGSE, S. (2000) Bending instability of electrically charged liquid jets of polymer solutions in electrospinning. *Journal of Applied Physics.* **87**(9), pp. 4531-4547.

RENEKER, D. H., YARIN, A. L., ZUSSMAN, E. & XU, H. (2007) Electrospinning of nanofibers from polymer solutions and melts. *Advances in Applied Mechanics.* **41**, pp. 43-195,345-346.

REZNIK, S. N., YARIN, A. L., THERON, A. & ZUSSMAN, E. (2004) Transient and steady shapes of droplets attached to a surface in a strong electric field. *Journal of Fluid Mechanics.* **516**, pp. 349-377.

RIDLER, T. W. & CALVARD, S. (1978) Picture thresholding using an iterative selection method. *IEEE Transactions on Systems, Man and Cybernetics.* **SMC-8**(8), pp. 630-632.

RIO-CRISTOBAL, A. & MARTIN, R. (2014) Corneal assessment technologies: Current status. *Survey of Ophthalmology.* **59**(6), pp. 599-614.

RITGER, P. L. & PEPPAS, N. A. (1987a) A simple equation for description of solute release I. Fickian and non-Fickian release from non-swellable devices in the form of slabs, spheres, cylinders or discs. *Journal of Controlled Release.* **5**, pp. 23-36.

RITGER, P. L. & PEPPAS, N. A. (1987b) A simple equation for description of solute release II. Fickian and anomalous release from swellable devices. *Journal of Controlled Release.* **5**, pp. 37-42.

ROBB, B. & LENNOX, B. (2011). The Electrospinning Process, Conditions and Control. In: BOSWORTH, L. & DOWNES, S. (eds.) *Electrospinning for Tissue Regeneration.* Cambridge, U.K.: Woodhead Publishing Limited.

RUBERT, M., DEHLI, J., LI, Y.-F., TASKIN, M. B., XU, R., BESENBACHER, F. & CHEN, M. (2014) Electrospun PCL/PEO coaxial fibers for basic fibroblast growth factor delivery. *Journal of Materials Chemistry B.* **2**, pp. 8538-8546.

RUST, M. J., BATES, M. & ZHUANG, X. (2006) Stochastic optical reconstruction microscopy (STORM) provides sub-diffraction-limit image resolution. *Nature Methods.* **3**(10), pp. 793-795.

SAHAY, R., THAVASI, V. & RAMAKRISHNA, S. (2011) Design modifications in electrospinning setup for advanced applications. *Journal of Nanomaterials.* **2011**, pp. 1-17.

SAKAGUCHI, M., HORI, H., HATTORI, S., IRIE, S., IMAI, A., YANAGIDA, M., MIYAZAWA, H., TODA, M. & INOUYE, S. (1999) IgE reactivity to α1 and α2 chains of bovine type I collagen in children with bovine gelatin allergy. *Journal of Allergy and Clinical Immunology.* **104**(3), pp. 695-699.

SAKAGUCHI, M. & INOUYE, S. (2000) IgE sensitization to gelatin: The probable role of gelatin-containing diphtheria–tetanus–acellular pertussis (DTaP) vaccines. *Vaccine.* **18**, pp. 2055-2058.

SAKAI, Y., YAMATO, R., ONUMA, M., KIKUTA, T., WATANABE, M. & NAKAYAMA, T. (1998) Non-antigenic and low allergic gelatin produced by specific digestion with an enzyme-coupled matrix. *Biol Pharm Bull.* **21**(4), pp. 330-334.

SANCHEZ, I., MARTIN, R., USSA, F. & FERNANDEZ-BUENO, I. (2011) The parameters of the porcine eyeball. *Graefe's Archive for Clinical and Experimental Ophthalmology.* **249**, pp. 475-482.

SCHINDELIN, J., ARGANDA-CARRERAS, I., FRISE, E., KAYNIG, V., LONGAIR, M., PIETZSCH, T., PREIBISCH, S., RUEDEN, C., SAALFELD, S., SCHMID, B., TINEVEZ, J.-Y., WHITE, D. J., HARTENSTEIN, V., ELICEIRI, K.,

TOMANCAK, P. & CARDONA, A. (2012) Fiji: An open-source platform for biological-image analysis. *Nature Methods.* **9**(7), pp. 676-682.

SCHMIDT, C. E. & LEACH, J. B. (2003) Neural tissue engineering: Strategies for repair and regeneration. *Annual Review of Biomedical Engineering.* **5**, pp. 293-347.

SCHMITZ, C. & HOF, P. R. (2005) Design-based stereology in neuroscience. *Neuroscience.* **130**, pp. 813-831.

SCHNELL, E., KLINKHAMMER, K., BALZER, S., BROOK, G., KLEE, D., DALTON, P. & MEY, J. (2007) Guidance of glial cell migration and axonal growth on electrospun nanofibers of poly-ε-caprolactone and a collagen/poly-ε-caprolactone blend. *Biomaterials.* **28**, pp. 3012-3025.

SHANER, N. C., STEINBACH, P. A. & TSIEN, R. Y. (2005) A guide to choosing fluorescent proteins. *Nature Methods.* **2**(12), pp. 905-909.

SHAW, P. J. (2006). Comparison of widefield/deconvolution and confocal microscopy for three-dimensional imaging. In: PAWLEY, J. B. (ed.) *Handbook of Biological Confocal Microscopy.* U.S. : Springer.

SHEPPARD, C. J. R. & WILSON, T. (1978) Depth of field in the scanning microscope. *Optics Letters.* **3**(3), pp. 115-117.

SHIMOMURA, O., JOHNSON, F. H. & SAIGA, Y. (1962) Extraction, purification and properties of aequorin, a bioluminescent protein from the luminous hydromedusan, Aequorea. *Journal of Cellular and Comparative Physiology.* **59**(3), pp. 223-239.

SHIN, Y. M., HOHMAN, M. M., BRENNER, M. P. & RUTLEDGE, G. C. (2001) Electrospinning: A whipping fluid jet generates submicron polymer fibers. *Applied Physics Letters.* **78**(8), pp. 1149-1151.

SIMPSON, G. J. (2004) Molecular origins of the remarkable chiral sensitivity of second-order nonlinear optics. *ChemPhysChem.* **5**, pp. 1301-1310.

SINGH, J. & KAUR, G. (2007) Transcriptional regulation of polysialylated neural cell adhesion molecule expression by NMDA receptor activation in retinoic acid-differentiated SH-SY5Y neuroblastoma cultures. *Brain Research.* **1154**, pp. 8-21.

SINHA, V. R., BANSAL, K., KAUSHIK, R., KUMRIA, R. & TREHAN, A. (2004) Poly-ϵ-caprolactone microspheres and nanospheres: An overview. *International Journal of Pharmaceutics.* **278**, pp. 1-23.

SMITH, T. B. (2007) Modeling corneal transparency. *American Journal of Physics.* **75**(7), pp. 588-596.

SONG, F., WANG, X.-L. & WANG, Y.-Z. (2011) Poly(N-isopropylacrylamide)/poly(ethylene oxide) blend nanofibrous scaffolds: Thermo-responsive carrier for controlled drug release. *Colloids and Surfaces B: Biointerfaces.* **88**, pp. 749-754.

STREILEIN, J. W. (2003) Ocular immune privilege: Therapeutic opportunities from an experiment of nature. *Nature Reviews Immunology.* **3**, pp. 879-889.

SU, Y., SU, Q., LIU, W., JIN, G., MO, X. & RAMAKRISHNA, S. (2012) Dual-drug encapsulation and release from core-shell nanofibers. *Journal of Biomaterials Science, Polymer Edition.* **23**, pp. 861-871.

SUN, Z., ZUSSMAN, E., YARIN, A. L., WENDORFF, J. H. & GREINER, A. (2003) Compound core-shell polymer nanofibers by co-electrospinning. *Advanced Materials.* **15**(22), pp. 1929-1932.

SUNDARAY, B., SUBRAMANIAN, V., NATARAJAN, T. S., XIANG, R.-Z., CHANG, C.-C. & FANN, W.-S. (2004) Electrospinning of continuous aligned polymer fibers. *Applied Physics Letters.* **84**(7), pp. 1222-1224.

TAL, E., ORON, D. & SILBERBERG, Y. (2005) Improved depth resolution in video-rate line-scanning multiphoton microscopy using temporal focusing. *Optics Letters.* **30**(13), pp. 1686-1688.

TAYLOR, G. (1969) Published. Electrically driven jets. Proceedings of the Royal Society of London A: Mathematical, Physical and Engineering Sciences, 26 March 1969. The Royal Society, pp. 453-475.

TAYLOR, K. I. & TAYLOR, H. R. (1999) Distribution of azithromycin for the treatment of trachoma. *British Journal of Ophthalmology.* **83**(2), pp. 134-135.

TEH, T. K. H., TOH, S. L. & GOH, J. C. H. (2013) Aligned fibrous scaffolds for enhanced mechanoresponse and tenogenesis of mesenchymal stem cells. *Tissue Engineering Part A.* **19**(11-12), pp. 1360-1372.

TEO, W. E., KOTAKI, M., MO, X. M. & RAMAKRISHNA, S. (2005) Porous tubular structures with controlled fibre orientation using a modified electrospinning method. *Nanotechnology.* **16**, pp. 918-924.

THERON, A., ZUSSMAN, E. & YARIN, A. L. (2001) Electrostatic field-assisted alignment of electrospun nanofibres. *Nanotechnology.* **12**, pp. 384-390.

THOMAS, V., JOSE, M. V., CHOWDHURY, S., SULLIVAN, J. F., DEAN, D. R. & VOHRA, Y. K. (2006) Mechano-morphological studies of aligned nanofibrous scaffolds of polycaprolactone fabricated by electrospinning. *Journal of Biomaterials Science, Polymer Edition.* **17**(9), pp. 969-984.

TORNELLO, P. R. C., CARACCIOLO, P. C., CUADRADO, T. R. & ABRAHAM, G. A. (2014) Structural characterization of electrospun micro/nanofibrous scaffolds by liquid extrusion porosimetry: A comparison with other techniques. *Materials Science and Engineering C.* **41**, pp. 335-342.

TSIEN, R. Y. (1989) Fluorescent probes of cell signaling. *Annual Review of Neuroscience.* **12**, pp. 227-253.

VALMIKINATHAN, C. M., DEFRODA, S. & YU, X. (2009) Polycaprolactone and bovine serum albumin based nanofibers for controlled release of nerve growth factor. *Biomacromolecules.* **10**(5), pp. 1084-1089.

VAN VLIERBERGHE, S., CNUDDE, V., DUBRUEL, P., MASSCHAELE, B., COSIJNS, A., DE PAEPE, I., JACOBS, P. J. S., VAN HOOREBEKE, L., REMON, J. P. & SCHACHT, E. (2007) Porous gelatin hydrogels: 1. Cryogenic formation and structure analysis. *Biomacromolecules.* **8**(2), pp. 331-337.

VAN VLIERBERGHE, S., DE WAEL, K., BUSCHOP, H., ADRIAENS, A., SCHACHT, E. & DUBRUEL, P. (2008a) Ozonization and cyclic voltammetry as efficient methods for the regeneration of gelatin-coated SPR chips. *Macromolecular Bioscience.* **8**, pp. 1090-1097.

VAN VLIERBERGHE, S., DUBRUEL, P., LIPPENS, E., MASSCHAELE, B., VAN HOOREBEKE, L., CORNELISSEN, M., UNGER, R., KIRKPATRICK, C. J. & SCHACHT, E. (2008b) Toward modulating the architecture of hydrogel scaffolds: Curtains versus channels. *Journal of Materials Science: Materials in Medicine.* **19**, pp. 1459-1466.

VAN VLIERBERGHE, S., VANDERLEYDEN, E., BOTERBERG, V. & DUBRUEL, P. (2011) Gelatin functionalization of biomaterial surfaces: Strategies for immobilization and visualization. *Polymers.* **3**, pp. 114-130.

VASITA, R. & KATTI, D. S. (2006) Nanofibers and their applications in tissue engineering. *International Journal of Nanomedicine.* **1**(1), pp. 15-30.

VERT, M., LI, S. M., SPENLEHAUER, G. & GUÉRIN, P. (1992) Bioresorbability and biocompatibility of aliphatic polyesters. *Journal of Materials Science: Materials in Medicine.* **3**, pp. 432-446.

VUNJAK-NOVAKOVIC, G., ALTMAN, G., HORAN, R. & KAPLAN, D. L. (2004) Tissue engineering of ligaments. *Annu Rev Biomed Eng.* **6**, pp. 131-156.

WALBOOMERS, X. F. & JANSEN, J. A. (2001) Cell and tissue behavior on micro-grooved surfaces. *Odontology.* **89**, pp. 2-11.

WALSH, D., FURUZONO, T. & TANAKA, J. (2001) Preparation of porous composite implant materials by in situ polymerization of porous apatite containing ε-caprolactone or methyl methacrylate. *Biomaterials.* **22**, pp. 1205-1212.

WANG, H. B., MULLINS, M. E., CREGG, J. M., HURTADO, A., OUDEGA, M., TROMBLEY, M. T. & GILBERT, R. J. (2009) Creation of highly aligned electrospun poly-L-lactic acid fibers for nerve regeneration applications. *Journal of Neural Engineering.* **6**, p. 016001.

WANG, L., LI, C., RYAN, A. J. & ARMES, S. P. (2006) Synthesis and peptide-induced degradation of biocompatible fibers based on highly branched poly(2-hydroxyethyl methacrylate). *Advanced Materials.* **18**, pp. 1566-1570.

WANG, L. & RYAN, A. J. (2011). Introduction to Electrospinning. In: BOSWORTH, L. & DOWNES, S. (eds.) *Electrospinning for Tissue Regeneration.* Cambridge, U.K.: Woodhead Publishing Limited.

WANG, S., WANG, B., PAN, N., FU, L., WANG, C., SONG, G., AN, J., LIU, Z., ZHU, W., GUAN, Y., XU, Z.-Q. D., CHAN, P., CHEN, Z. & ZHANG, Y. A. (2015) Differentiation of human induced pluripotent stem cells to mature functional Purkinje neurons. *Scientific Reports.* **5**(9232), pp. 1-9.

WANG, T.-Y., FORSYTHE, J. S., NISBET, D. R. & PARISH, C. L. (2012) Promoting engraftment of transplanted neural stem cells/progenitors using biofunctionalised electrospun scaffolds. *Biomaterials.* **33**, pp. 9188-9197.

WEST, M. J. (1999) Stereological methods for estimating the total number of neurons and synapses: Issues of precision and bias. *Trends in Neurosciences.* **22**, pp. 51-61.

WEST, M. J. (2002) Design-based stereological methods for counting neurons. *Progress in Brain Research.* **135**, pp. 43-51.

WHITCHER, J. P. & SRINIVASAN, M. (1997) Corneal ulceration in the developing world—a silent epidemic. *British Journal of Ophthalmology.* **81**(8), pp. 622-623.

WHITCHER, J. P., SRINIVASAN, M. & UPADHYAY, M. P. (2001) Corneal blindness: A global perspective. *Bulletin of the World Health Organization.* **79**(3), pp. 214-221.

WILLIAMS, R. M., ZIPFEL, W. R. & WEBB, W. W. (2005) Interpreting second-harmonic generation images of collagen I fibrils. *Biophysical Journal.* **88**(2), pp. 1377-1386.

WILSON, A. (2011). Regulatory Issues Relating to Electrospinning. In: BOSWORTH, L. & DOWNES, S. (eds.) *Electrospinning for Tissue Regeneration.* Cambridge, U.K.: Woodhead Publishing Limited.

WINN, B., WHITAKER, D., ELLIOTT, D. B. & PHILLIPS, N. J. (1994) Factors affecting light-adapted pupil size in normal human subjects. *Investigative Ophthalmology and Visual Science.* **35**, pp. 1132-1137.

WOO, S. L.-Y., ABRAMOWITCH, S. D., KILGER, R. & LIANG, R. (2006) Biomechanics of knee ligaments: injury, healing, and repair. *Journal of Biomechanics.* **39**, pp. 1-20.

WOODFIELD, T. B. F., MALDA, J., DE WIJN, J., PETERS, F., RIESLE, J. & VAN BLITTERSWIJK, C. A. (2004) Design of porous scaffolds for cartilage tissue engineering using a three-dimensional fiber-deposition technique. *Biomaterials.* **25**, pp. 4149-4161.

WOODRUFF, M. A. & HUTMACHER, D. W. (2010) The return of a forgotten polymer: Polycaprolactone in the 21st century. *Progress in Polymer Science (Oxford).* **35**(10), pp. 1217-1256.

WÖRZ, A., BERCHTOLD, B., MOOSMANN, K., PRUCKER, O. & RÜHE, J. (2012) Protein-resistant polymer surfaces. *Journal of Materials Chemistry.* **22**, pp. 19547-19561.

XAVIER, J. B., SCHNELL, A., WUERTZ, S., PALMER, R., WHITE, D. C. & ALMEIDA, J. S. (2001) Objective threshold selection procedure (OTS) for segmentation of scanning laser confocal microscope images. *Journal of Microbiological Methods.* **47**, pp. 169-180.

XI, P., ANDEGEKO, Y., WEISEL, L. R., LOZOVOY, V. V. & DANTUS, M. (2008) Greater signal, increased depth, and less photobleaching in two-photon microscopy with 10 fs pulses. *Optics Communications.* **281**, pp. 1841-1849.

XIE, H.-R., HU, L.-S. & LI, G.-Y. (2010a) SH-SY5Y human neuroblastoma cell line: *In vitro* cell model of dopaminergic neurons in Parkinson's disease. *Chinese Medical Journal.* **123**(8), pp. 1086-1092.

XIE, J., MACEWAN, M. R., SCHWARTZ, A. G. & XIA, Y. (2010b) Electrospun nanofibers for neural tissue engineering. *Nanoscale.* **2**, pp. 35-44.

XIYI, C. & CAMPAGNOLA, P. J. (2013). SHG Microscopy and Its Comparison with THG, CARS, and Multiphoton Excited Fluorescence Imaging. In: PAVONE, F. S. & CAMPAGNOLA, P. J. (eds.) *Second Harmonic Generation Imaging.* Boca Raton, Florida: CRC Press.

XU, C. Y., INAI, R., KOTAKI, M. & RAMAKRISHNA, S. (2004) Aligned biodegradable nanofibrous structure: A potential scaffold for blood vessel engineering. *Biomaterials.* **25**, pp. 877-886.

XU, Y.-G., XU, Y.-S., HUANG, C., FENG, Y., LI, Y. & WANG, W. (2008) Development of a rabbit corneal equivalent using an acellular corneal matrix of a porcine substrate. *Molecular Vision.* **14**, pp. 2180-2189.

YAN, H., LIU, L. & ZHANG, Z. (2009) Alignment of electrospun nanofibers using dielectric materials. *Applied Physics Letters.* **95**, pp. 143114-143114.

YANG, F., MURUGAN, R., WANG, S. & RAMAKRISHNA, S. (2005) Electrospinning of nano/micro scale poly(L-lactic acid) aligned fibers and their potential in neural tissue engineering. *Biomaterials.* **26**, pp. 2603-2610.

YANG, S., LEONG, K.-F., DU, Z. & CHUA, C.-K. (2001a) The design of scaffolds for use in tissue engineering. Part I. Traditional factors. *Tissue Engineering.* **7**(6), pp. 679-689.

YANG, X., BEYENAL, H., HARKIN, G. & LEWANDOWSKI, Z. (2000) Quantifying biofilm structure using image analysis. *Journal of Microbiological Methods.* **39**, pp. 109-119.

YANG, X., BEYENAL, H., HARKIN, G. & LEWANDOWSKI, Z. (2001b) Evaluation of biofilm image thresholding methods. *Water Research.* **35**(5), pp. 1149-1158.

YANG, Y., LI, X., CUI, W., ZHOU, S., TAN, R. & WANG, C. (2008) Structural stability and release profiles of proteins from core-shell poly(DL-lactide) ultrafine fibers prepared by emulsion electrospinning. *Journal of Biomedical Materials Research Part A.* **86**(2), pp. 374-385.

YARIN, A. L., ZUSSMAN, E., WENDORFF, J. H. & GREINER, A. (2007) Material encapsulation and transport in core-shell micro/nanofibers, polymer and carbon nanotubes and micro/nanochannels. *Journal of Materials Chemistry.* **17**, pp. 2585-2599.

YASUI, T., TAKAHASHI, Y., ITO, M., FUKUSHIMA, S. & ARAKI, T. (2009) *Ex vivo* and *in vivo* second-harmonic-generation imaging of dermal collagen fiber in skin: Comparison of imaging characteristics between mode-locked Cr:forsterite and Ti:sapphire lasers. *Applied Optics.* **48**(10), pp. D88-D95.

YERLY, J., HU, Y., JONES, S. M. & MARTINUZZI, R. J. (2007) A two-step procedure for automatic and accurate segmentation of volumetric CLSM biofilm images. *Journal of Microbiological Methods.* **70**, pp. 424-433.

YU, D.-G., YU, J.-H., CHEN, L., WILLIAMS, G. R. & WANG, X. (2012) Modified coaxial electrospinning for the preparation of high-quality ketoprofen-loaded cellulose acetate nanofibers. *Carbohydrate Polymers.* **90**, pp. 1016-1023.

ZEIN, I., HUTMACHER, D. W., TAN, K. C. & TEOH, S. H. (2002) Fused deposition modeling of novel scaffold architectures for tissue engineering applications. *Biomaterials.* **23**, pp. 1169-1185.

ZELENY, J. (1914) The electrical discharge from liquid points, and a hydrostatic method of measuring the electric intensity at their surfaces. *Physical Review.* **3**(2), pp. 69-91.

ZENG, J., XU, X., CHEN, X., LIANG, Q., BIAN, X., YANG, L. & JING, X. (2003) Biodegradable electrospun fibers for drug delivery. *Journal of Controlled Release.* **92**, pp. 227-231.

ZENG, Y., YANG, J., HUANG, K., LEE, Z. & LEE, X. (2001) A comparison of biomechanical properties between human and porcine cornea. *Journal of Biomechanics.* **34**, pp. 533-537.

ZEUGOLIS, D. I., KHEW, S. T., YEW, E. S. Y., EKAPUTRA, A. K., TONG, Y. W., YUNG, L. Y. L., HUTMACHER, D. W., SHEPPARD, C. & RAGHUNATH, M. (2008) Electro-spinning of pure collagen nano-fibres—Just an expensive way to make gelatin? *Biomaterials.* **29**, pp. 2293-2305.

ZHANG, R. & MA, P. X. (1999) Poly(α-hydroxyl acids)/hydroxyapatite porous composites for bone-tissue engineering. I. Preparation and morphology. *Journal of Biomedical Materials Research.* **44**(4), pp. 446-455.

ZHANG, Y., HUANG, Z. M., XU, X., LIM, C. T. & RAMAKRISHNA, S. (2004) Preparation of core-shell structured PCL-r-gelatin bi-component nanofibers by coaxial electrospinning. *Chemistry of Materials.* **16**, pp. 3406-3409.

ZHANG, Y. Z., WANG, X., FENG, Y., LI, J., LIM, C. T. & RAMAKRISHNA, S. (2006) Coaxial electrospinning of (fluorescein isothiocyanate-conjugated bovine serum albumin)-encapsulated poly(ε-caprolactone) nanofibers for sustained release. *Biomacromolecules.* **7**(4), pp. 1049-1057.

ZHONG, S., TEO, W. E., ZHU, X., BEUERMAN, R. W., RAMAKRISHNA, S. & YUNG, L. Y. L. (2006) An aligned nanofibrous collagen scaffold by electrospinning and its effects on *in vitro* fibroblast culture. *Journal of Biomedical Materials Research Part A.* **79A**, pp. 456-463.

ZHOU, Y., CHAN, K. K. H., LAI, T. & TANG, S. (2013) Characterizing refractive index and thickness of biological tissues using combined multiphoton microscopy and optical coherence tomography. *Biomedical Optics Express.* **4**(1), pp. 38-50.

ZIPFEL, W. R., WILLIAMS, R. M. & WEBB, W. W. (2003) Nonlinear magic: Multiphoton microscopy in the biosciences. *Nature Biotechnology*. **21**(11), pp. 1369-1377.

ZOUMI, A., YEH, A. & TROMBERG, B. J. (2002) Imaging cells and extracellular matrix *in vivo* by using second-harmonic generation and two-photon excited fluorescence. *Proceedings of the National Academy of Sciences.* **99**(17), pp. 11014-11019.